

Title	Mathematical and computational approaches to contagion dynamics on networks
Authors	Humphries, Rory
Publication date	2022-09-27
Original Citation	Humphries, R. 2022. Mathematical and computational approaches to contagion dynamics on networks. PhD Thesis, University College Cork.
Type of publication	Doctoral thesis
Rights	© 2022, Rory Humphries. - https://creativecommons.org/licenses/by-nc-nd/4.0/
Download date	2025-05-09 11:34:14
Item downloaded from	https://hdl.handle.net/10468/14049

Mathematical and Computational Approaches to Contagion Dynamics on Networks



Thesis presented by
Rory Humphries

for the degree of
Doctor of Philosophy

University College Cork
School of Mathematical Sciences

Head of School: Dr. Kevin Hayes
Head of Discipline: Prof. Sebastian Wiecek

Supervisors: Dr. Philipp Hövel, Dr. Kieran Mulchrone

Internal Examiner: Dr. Andreas Amann
External Examiner: Prof. James Gleeson

2022

“Every new discovery is just a reminder... We’re all small and stupid.”

—*Everything Everywhere All at Once*

Contents

1	Introduction	1
2	Theoretical Background	9
2.1	Network Theory	9
2.1.1	Graphs	10
2.1.2	Matrix Representations of Graphs	14
2.1.3	Network Properties and Measures	17
2.2	Compartmental Epidemiological Models	28
2.2.1	Ordinary Differential Equation Models	28
2.2.2	Stability Analysis	33
2.3	Network Epidemiological Models	35
2.3.1	Individual-Based Model	37
2.3.2	Meta-Population Models	40
2.4	Network Mobility Models	46
2.4.1	Gravity Model	47

CONTENTS

2.4.2	Radiation Model	50
2.5	Summary	52
3	A Systematic Framework For the Modelling of Epidemics on Temporal Networks	55
3.1	Overview	56
3.2	Reduced Master Equations	59
3.3	SIR Network Model	61
3.3.1	Temporal Individual-based Model	62
3.3.2	Temporal Pair-based Model	65
3.4	Epidemic Threshold	71
3.5	Results	75
3.5.1	Synthetic Networks	76
3.5.2	Empirical Networks	84
3.6	Summary	92
4	A Meta-Population Model for the Spread of SARS-CoV-2	93
4.1	Overview	94
4.2	Local Dynamics	96
4.3	Network Contagion Model	101
4.4	Reproduction Number	103
4.5	Network Data	106

4.6	Mobility Model	107
4.7	Case study: Ireland	113
4.7.1	First Wave of COVID-19	113
4.7.2	Dynamic Interventions	124
4.8	Summary	130
5	Models for Cattle Trade	133
5.1	Analysis of Trade Networks	135
5.1.1	Cattle Trade Data	136
5.1.2	Cattle Trade Network Representation	137
5.1.3	Static Network Analysis	138
5.1.4	Temporal Network Analysis	143
5.2	Models for Cattle Trade	146
5.2.1	Gravity Model	147
5.2.2	Radiation Model	149
5.3	Results	151
5.4	Application to the Spread of Disease	155
5.5	Summary	156
6	Conclusion and Outlook	157
A	Vertex Pair Transition Rates for the PB Model	163

CONTENTS

Acknowledgements	165
-------------------------	------------

List of Publications	167
-----------------------------	------------

Acronyms

basic DFE Basic Disease-Free Equilibrium. 33, 34, 39, 44, 53, 69–71, 97, 98, 118

BTB Bovine Tuberculosis. 130, 149, 158

BVD Bovine Viral Diarrhoea. 149

CSO Central Statistics Office. 103, 104, 114

DFE Disease-Free Equilibrium. 69, 71, 96, 97

ED Electoral Division. 91, 104, 105, 107, 120, 125

GRM Generalised Radiation Model. 108, 109

IB Individual-Based. 35, 37–40, 53–56, 60, 61, 75, 79, 82, 85, 87, 154

MC Monte-Carlo. 55, 56, 73–77, 79–89, 155

NBT Non-Backtracking. 62, 63, 73, 77–80, 83–86, 88, 89, 139, 155

NISRA Northern Ireland Statistics and Research Agency. 103

NUTS Nomenclature of Territorial Units for Statistics. 103

ODE Ordinary Differential Equation. 30, 33, 34, 36, 37, 39, 54, 95, 99

PB Pair-Based. 53, 55, 56, 67, 68, 75, 89, 90, 155

RM Radiation Model. 109

RME Reduced Master Equation. 57–60, 63–65

SEIR Susceptible-Exposed-Infected-Recovered. 32

SIQRD Susceptible-Infected-Quarantined-Recovered-Dead. 156

SIR Susceptible-Infected-Recovered. 2, 4, 28, 31–33, 35, 36, 38–41, 43–45, 53, 55–57, 59, 60, 66, 67, 69, 70, 73–77, 80, 82, 83, 85, 87–90, 154–156

SIRS Susceptible-Infected-Recovered-Susceptible. 32

SIS Susceptible-Infected-Susceptible. 32, 69–71

SOA Super Output Area. 91, 104, 120, 125

TIB Temporal Individual-Based. 60–62, 65–67, 70, 73–77, 82–85, 87, 88, 155, 157

TPB Temporal Pair-Based. 56, 66, 67, 73–80, 82–85, 87, 88, 155–157

WHO World Health Organisation. 1

This is to certify that the work I am submitting is my own and has not been submitted for another degree, either at University College Cork or elsewhere. All external references and sources are clearly acknowledged and identified within the contents. I have read and understood the regulations of University College Cork concerning plagiarism and intellectual property.

Chapter 1

Introduction

For societies throughout history, epidemics have often been a leading cause of loss of life. It is even believed that the Antonine plague of 165AD saw the beginning of the decline of the Roman Empire [56, 165] with a large portion of its population decimated by the disease. This due to the soldiers of the empire bringing back diseases from people and lands they had previously had no contact with. Thus, from the earliest empires, humankind has struggled with the ever evolving landscape of communicable diseases.

In 1977, it appeared as though humanity had turned a corner in its bid to control and prevent infectious diseases. During that year, the last recorded case of naturally occurring smallpox was recorded [91], a disease that had killed countless of people over the course of millennia. For example, it is generally believed that the Antonine plague was an outbreak of smallpox.

Since its eradication, progress has been made towards the eradication of other diseases such as polio, malaria, measles and rubella to name a few [201]. This is very much an ongoing campaign, with the first malaria vaccine seeing recommendation by the World Health Organisation (WHO) for broad use in October 2021 [198].

It is not only human diseases which affect our society, zoonotic diseases have

historically also played a large role in human history as entire food sources have been wiped out. A recent example is that of the foot and mouth outbreak of 2001 in the UK [64, 88] in which approximately 6.5 million animals were culled in a successful campaign to bring the disease under control. The massive number of animals that were killed resulted in a reported loss of around £8 billion [183] in the combined public and private sectors of the UK.

Despite the large strides made in recent decades, 25% of yearly deaths are still caused by communicable diseases [163]. As a result, current pharmaceutical interventions are not enough to completely curtail such preventable losses. Coupled with the fact that there are still a number of diseases which have no available cure, such as AIDS, the disease caused by the virus HIV, as well as the fact that antibiotic resistant diseases are of growing concern, we must turn our attention in equal measure to understanding how these diseases spread from the context of mathematical models.

Following the outbreak of the severe acute respiratory syndrome coronavirus 2 (SARS-CoV-2) in 2019, the virus which causes the disease known commonly as COVID-19 [202], we are starkly reminded that epidemics of such a scale are not problems of the past. However, thanks to global cooperation of the scientific community at a level not seen before, the virus was brought under control by means of preventative non-pharmaceutical public health measures such as restriction of movements, quarantining, face masks and hand washing and also, by the eventual roll-out of a global vaccination programme. In the early stages of the disease, when the development of vaccines for the disease had just begun [182], mathematical modelling played a key role in the decision making of governments in relation to the public health measures they adopted. This is because non-pharmaceutical interventions were all that were available while the race to provide an effective vaccine was underway.

The foundation for much of modern epidemiological modelling can be traced back to 1927 in a paper by Kermack and McKendrick [111] that outlines what we refer today as the Susceptible-Infected-Recovered (SIR) model. This models the evolution of the disease in well mixed population, i.e., all individuals in the

population interact with an equal rate. Individuals start as susceptible and become infected with some probability after coming into contact with an infected individual, then once infected the individual recovers after some time. This type of model is referred to as a compartmental model and has seen many extensions since, taking into account factors such as incubation periods [90], vaccination [167], age [53] etc.

While these models can be useful, they often lack the nuance that comes with heterogeneous contact patterns within populations. As a result, research of epidemiological models has turned to network science in recent years, largely due to abundance of mobility data from sources such as mobile phones [82, 192], air traffic networks [31, 41, 100] etc.

Thanks to the internet and the vast amount of data being recorded in regards to interactions, be they physical or online, network science has benefited greatly. Network science is an area of mathematics that analysis complex networks such as the brain [125], internet [4], commuting patterns [71] etc., in other words, anything that can be reduced to interactions between objects, be they physical things or individuals. Often by reducing complicated systems to such a simple description, one can gain a deeper insight into how the interaction patterns affect the system as a whole. The mathematical structure of a network, that is referred to as a graph, consists of a number of vertices/nodes/hubs that are connected by edges/links. However, the term network and graph are often used interchangeably. There is often differences in the terminology depending on the author or field.

Much of the early analysis of complex networks was pioneered by the likes of Erdős and Rényi around 1960 who discovered many results related to random networks [60–62]. This allowed for the study networks/graphs at arbitrary scales as graphs could now be described via more concise means via the probability of a vertex having k edges attached to it. This means very large graphs could be considered without the need to formulate very large matrices. At the same time, there were a number of individuals such as Bevelas, Katz and Freeman, some of whom were sociologists, who were attempting to quantify the importance of vertices in a graph according to different metrics [21, 69, 70, 107]. This led to the

concept of centrality measures in graphs, a concept even more important today than it was then. This due to the enormous amounts of highly linked data that is produced today, extensions of these original centrality algorithms allow us to sort what data is more likely to be considered important.

By the 1990s the availability of cheap computers started to become more widespread. As a result, many of these concepts of centrality were extended to more complicated descriptions which could be solved by numerical means. At this time individuals such as Wasserman, White, and Page began to look at network science with the idea of analysing far larger networks than before [151, 195, 197]. In particular the work by Page was the basis for the web page ranking algorithm used by Google.

As interest in network science grew, so did its applicability in other areas, particularly in mathematical epidemiology where the likes of Newman formulated the SIR model for networks [140, 144] and moved the theory forward. However, many of the results used network epidemiology date back earlier (1970s) to the study of percolation on networks by the likes of Mollison and Grassberger [81, 139]. Much of this work was done on configuration graphs, that is, graphs with a set degree distribution. As a result, many of the results are specific to the type of configuration graph, like the random graph of Erdős and Rényi discussed previously. This was due to the lack of availability of much real network data. Thus, in recent years, there has been a large increase in work done on data driven network models. These are models which use real world networks to inform the model, such as using the adjacency matrix to determine the coupling in some set of ordinary differential equations which describe the evolution of a disease.

These data-driven models appear in various forms, the most basic being the individual-based model as given in Ref. [10] by Anderson and May, named as such because it ignores past interactions, and thus the state of each individual/vertex is considered independent. This model has seen extensive use due to its relatively simple description and has produced many interesting results such as the epidemic threshold. This threshold is the combination of parameters in a model at which the qualitative dynamics change from a disease being unable to sustain

itself to causing an epidemic [194]. It is an incredibly important quantity when using mathematical models to inform public health policy. There is an often used extension to the individual-based model, and that is the pair-based model (see for instance, Sharkey and Gleeson [78, 170]), which helps recover some of the inaccuracy lost in the individual-based model. The pair-based model is still an approximation, simply a better one. This does come at the cost of slightly increased complexity.

While network epidemiological models help account for the heterogeneity in contact patterns that the well mixed models of Kermack and McKendrick do not account for, there is still a temporal aspect that is not accounted for. For such static graphs (graphs that do not change with time), the contact patterns are usually aggregated over some time span. This leads to contacts patterns that are averaged over the time span. An extension which has seen an increase in interest in the last decade is that of temporal graphs, i.e., graphs that change with time [25, 180]. This is useful for contact patterns that are not well approximated by an averaged static graph. For example, cattle trade networks [187] exhibit very distinct seasonal trading patterns, as a result, the ability for a disease to spread can be dependent on the time the disease is introduced, it can also depend on the length of time between contacts, if the timescale on which edges appear is far slower than the rate at which individuals recover from the disease then it is likely the disease will die out [123].

An important result is that from Valdano [189], which extends the concept of epidemic threshold to temporal networks by taking into account the time scale on which the contacts happen compared to the timescale of the disease. Recently, much work has been done in order to try and generalise many of the results in network science to the temporal setting [93, 153, 184, 189]. We will see in Chp. 3, that we will extend both the individual-based and an improved pair-based model to the temporal setting.

Both the discussed individual-based and pair-based models assume that each vertex is a single entity/individual which interacts with others. While this assumption can be useful, often this level of granularity is not needed. An alter-

native approach is to use a meta-population model, a concept that comes from ecology [86]. This assumes that each vertex in a graph/network is a smaller community part of the larger community the graph represents [22]. The assumption is that this smaller community is well mixed and thus, the compartmental models of Kermack and McKendrick can be used. This implies that the disease is able to maintain itself in vertices, even in the absence of interactions. In the case of the meta-population model the edges are weighted, meaning that there is a real value associated with them. In this context the weight represents the rate of travel from one vertex to another. In Ref. [22], Belik extends the concept of meta-population models to commuting patterns of humans.

Similar to extending the individual-based and pair-based models to the temporal setting, it is also possible to extend the meta-population models to the temporal setting. This is done in a rather natural way by allowing the weights of the graph edges to depend on time as in Ref. [121], meaning, the rate of travel between vertices is dependent on the time. This allows for complex periodic commuting patterns that see individuals leave their home vertex during the day, mix with others, then return to their home vertex and mix with others there. We will use this concept of temporal meta-population models in Chp. 4 in order to model the spread of COVID-19.

While in this day and age we have more data than we know what to do with, it can be the case that when attempting to construct a graph to model some system there is no data available at the right granularity or even at all. This is particularly the case in developing countries which do not have the means to collect such detailed data. As a result, it is often easier to use mobility models to construct the edges of a graph representing mobility of humans or even cattle trades. Simini et al. in their seminal paper Ref. [174], develops a model (called the radiation model) based on process of radiation which can accurately model the movement of humans at large scales. This offers improvements over the long used gravity model [33] that lacks a derivation like the radiation model, and is based on assumptions and heuristics instead. We will see the radiation model used in both Chps. 4 and 5 in order to construct networks modelling commuting

and cattle trade.

Outline of Thesis. In Chapter 2, we introduce the basic terminology and concepts needed for the rest of the chapters. In particular we introduce the basics of graph/network theory, epidemiological models (both well mixed and on networks), and mobility models (the gravity and radiation models). In Chapter 3, we introduce a general framework for epidemiological network models from which the known individual-based and pair-based models can be derived. We then introduce a more exact pair-based model by showing previous iterations are a linearised version of it, and then we extend it further to the temporal setting. In Chapter 4, we present a meta-population model for the spread of COVID-19 in Ireland which makes use of temporal commuting patterns generated from the radiation model. Finally in Chapter 5, we analyse a year worth of Irish cattle trade data. We then fit a number of mobility models and show that an altered version of the radiation model, which we call the generalised radiation model, is able to accurately reproduce the distance distribution of cattle trades in the country.

Chapter 2

Theoretical Background

2.1 Network Theory

Network theory is a branch of mathematics that concerns itself with analysing the interactions within complex systems. As such, network science has seen much use in biology [77], sociology [51], applied mathematics and physics [57] etc. Examples include, predator-prey food webs [102], the brain [96], social networks both in person and online [156], and air travel [41].

In recent decades, network theory has experienced a huge increase in interest, along with many other fields, thanks to the availability of cheap, powerful computers [166] and importantly, increased availability of data. Much of this data is made freely available [75], which aids with the testing and development of theories.

Network theory has a very rich and interesting history, much of which lies in the closely related field of graph theory that can trace its roots back to 1741. This is when Euler’s work on solving the “seven bridges of Königsberg” [63] was first published. In that work, Euler shows that is impossible, for the street layout of Königsberg at the time, to traverse each of the seven bridges only once, by

converting the problem from bridges and islands, to vertices and edges. Thus, paving the way with some of the first graph theoretic results used.

There is often confusion as to the relationship between network theory and graph theory. In reality they are much the same thing with different interests and goals. Graph theory concerns itself with the mathematical object the *graph* and results on this object. However, network theory concerns itself with problems, often modelling some sort of interaction in another area of science [14, 117, 123, 125], which may be represented as a graph, and what can be learned about the problem by using graph theoretic results. Thus, when we discuss networks and graphs, we use the term network to refer to a real system of interactions, and we use the term graph to refer to the mathematical object that they represent. However, the difference between these two is not always clear, and so they may be used synonymously at times.

The largest source of confusion is that fact that there can be slight differences in terminology depending on the author/field/result. Throughout this thesis care is made to be consistent in the use of terminology, but the alternatives will also be presented to ensure the reader can follow sources if need be. The rest of this section will deal with presenting the basics of graph/network theory required for the later chapters.

2.1.1 Graphs

In this section we introduce the basic graph structures which provide the foundation for all of graph theory. In essence, a graph is an object which maps a set of vertices or nodes to each other via edges or links.

Definition 2.1 (Undirected Graph). An undirected graph [28] or sometimes just called a graph is an ordered triple (V, E, ψ) , where V is the set of vertices, E is the set of edges, which is disjoint from V , and ψ is the incidence function, that maps each edge in E to an **unordered** pair of vertices in V . The incidence function

for an undirected graph is defined as,

$$\psi : E \longrightarrow \{\{u, v\} | u, v \in V\}. \quad (2.1)$$

As defined above, the set V contains what are referred to as vertices or nodes, with the former more popular in graph theory and the latter more popular in network theory. Similarly, the E contains what are referred to as edges or links. Take for example, Fig. 2.1 which shows an example of an undirected graph. The set of vertices are $V = \{a, b, c, d, e\}$ and the set of edges are $E = \{u, v, w, x, y, z\}$. The incidence function of this graph would then be $\psi(u) = \{a, e\} = \{e, a\}$, $\psi(v) = \{a, c\} = \{c, a\}$, $\psi(w) = \{e, b\} = \{b, e\}$ etc. Also, loops/self-loops are allowed in the definition of a graph, that is, edges which connected a vertex to itself. For example, in Fig.2.2, the edge x is a self-loop with $\psi(x) = \{b\}$.

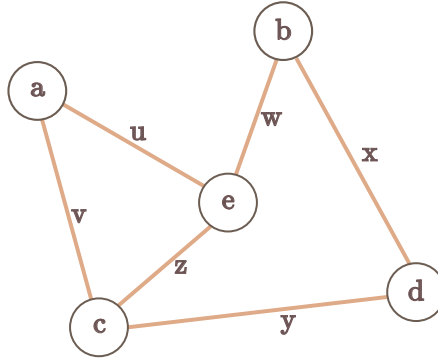


Figure 2.1: An example of a simple undirected graph.

The use of the incidence function may seem extraneous in the context of this example as each edge is unambiguously identified by its incident vertices, this type of graph is referred to as simple. However, graphs permit the existence of multiple parallel edges between the same vertices as in Fig. 2.2. In such a case, the adjacent vertices do not unambiguously identify the edge as we have $\psi(u) = \psi(w) = \{e, b\}$.

A slight alteration to the definition above gives rise to another type of graph, referred to as directed graph. These types of graphs are useful when dealing with directed or one way interactions which are not reciprocal, e.g. hyper-links on web

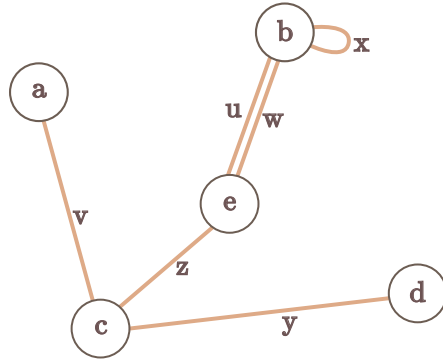


Figure 2.2: An example of a undirected graph with a loop, x , and multi-edge between e and b .

pages, linking to another page does not imply that it links back.

Definition 2.2 (Directed Graph). A directed graph [28] is an ordered triple (V, E, ψ) , where V is the set of vertices, E is the set of edges, which is disjoint from V , and ψ is the incidence function that maps each edge in E to an **ordered** pair of vertices in V . The incidence function for a directed graph is defined as,

$$\psi : E \longrightarrow \{(u, v) | u, v \in V\}. \quad (2.2)$$

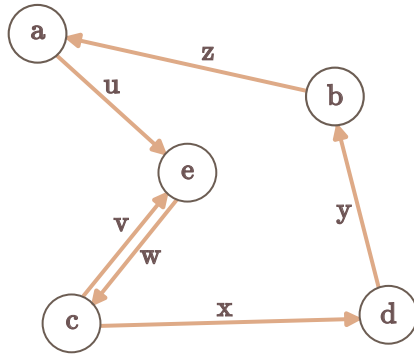


Figure 2.3: An example of a simple directed graph.

In the example of the directed graph given in Fig. 2.3, the vertex set is given by $V = \{a, b, c, d, e\}$ and the edge set is given by $E = \{u, v, w, x, y, z\}$. The incidence function maps the edges to the following ordered pairs of vertices, $\psi(u) = (a, e)$, $\psi(v) = (c, e)$, $\psi(w) = (e, c)$ etc.

We have now introduced the two basic graph structures, an undirected and

directed graph. We provided the most general definition for these structures which uses the concept of the incidence function. There are many types of restrictions which may be made to these graphs which give rise to particular structures or named graphs. Some of the most common are the following,

Definition 2.3 (Simple (Un)directed Graph). A simple (un)directed graph [28], $G = (V, E)$, is one in which self-loops and parallel edges are not allowed. This implies the following incidence functions. For an undirected graph:

$$\psi : E \longrightarrow \{\{u, v\} | u, v \in V, u \neq v\}, \quad (2.3)$$

where ψ is bijective. For a directed graph:

$$\psi : E \longrightarrow \{(u, v) | u, v \in V, u \neq v\}, \quad (2.4)$$

where ψ is bijective.

Much of graph theory concerns itself with simple graphs, or at least graphs that do not contain parallel edges, as result they often get special treatment. Since the edges in graphs with no parallel edges can be unambiguously associated with the vertices they are incident with, the incidence function is dropped and the graph is specified as the ordered pair $G = (V, E)$ where V is specified as before and E is now a set of ordered or unordered pairs of vertices. For an undirected graph $E \subseteq \{\{u, v\} | u, v \in V\}$ and for a directed graph $E \subseteq \{(u, v) | u, v \in V\}$.

Definition 2.4 (Weighted Graph). A weighted graph [145], $G = (V, E, \psi, \omega)$, is a graph which also has a weight function, ω , associated with it. This maps each edge to some real value, i.e.,

$$\omega : E \longrightarrow \mathbb{R}. \quad (2.5)$$

Much of the time in network science, one has some sort of values associated with the edges in a graph structure, as a result, weighted graphs often play a very important role. For example, in road transport networks, the weights often represent factors such as average traffic congestion, road quality or number of traffic lights etc. This information is vital in determining shortest paths from one

vertex to another [160].

Definition 2.5 (Discrete-Time Temporal Graph). A discrete-time temporal graph [25], $\mathcal{G} = (G_{t_1}, G_{t_2}, \dots, G_{t_{n_t}})$, is a sequence of n_t graphs (and thus n_t time-stamps). Each of these graphs, $G_{t_i} = (V, E_{t_i})$, which represent a snapshot of the network at some time t_i , share the same vertex set V , but differ in their edge sets E_{t_i} . The graph snapshots are all assumed of the same type, meaning that they are all either directed/undirected, weighted/unweighted etc.

Note that continuous-time representations of temporal graphs are also possible [146], however, as networks often deal with empirical data, which are just time-stamped measurements, a discrete description is required. As a result, we will not be dealing with continuous-time temporal graphs.

2.1.2 Matrix Representations of Graphs

While graphs are very useful structures, from the definitions given in the previous section they can be difficult to deal with in many areas of mathematics. For this reason matrix representations of graphs are used which allow for very powerful tools, such as linear algebra, to be used when analysing graphs. They are also far more natural descriptions for use on computers.

An adjacency matrix is a matrix that describes the number of parallel edges connecting two vertices, or in the case of a weighted graph, the weight of edge connecting two vertices. In order to associate with each (un)directed graph an adjacency matrix, we first need to be able quantify this number. The number of edges connecting two vertices u and v in an undirected graph is given by $|\psi^{-1}(\{u, v\})|$, and the number of edges connecting u to v in a directed graph is given by $|\psi^{-1}((u, v))|$. These quantities are the cardinality of the pre-image of the incidence functions. For example, take graph given in Fig. 2.2, we would have $|\psi^{-1}(\{e, b\})| = 2$, $|\psi^{-1}(\{c, d\})| = 1$, etc. When dealing with adjacency matrices it is often easier to represent each vertex as a unique integer in $\{1, 2, \dots, |V|\}$. This way each vertex maps directly to row/column of the matrix.

Definition 2.6 (Adjacency Matrix of an Undirected Graph). The adjacency matrix \mathbf{A} , of an undirected graph $G = (V, E, \psi)$ is defined as,

$$A_{ij} = \begin{cases} |\psi^{-1}(\{i, j\})| & \text{if } i \neq j \\ 2|\psi^{-1}(\{i, j\})| & \text{if } i = j. \end{cases} \quad (2.6)$$

In words, the entry in row i and column j is the number of edges connecting vertex i and j or two times the number of edges connecting i and j when $i = j$, i.e., when its a loop. The reason for multiplying the diagonal by 2 can be thought of as accounting for the fact that self-loops touch the vertex twice. The practical reason is that many results become nicer when including this multiplication on the diagonal, thus it has become standard practice. Because the number of edges from i to j is equal to the number of edges from j to i in an undirected graph i.e., $\psi^{-1}(\{i, j\}) = \psi^{-1}(\{j, i\})$, the adjacency matrix for an undirected graph is symmetric.

Definition 2.7 (Adjacency Matrix of a Directed Graph). For a directed graph, the adjacency matrix is,

$$A_{ij} = |\psi^{-1}((i, j))|. \quad (2.7)$$

That is, the entry in row i and column j is the number of edges connecting vertex i to j .

Take the examples of the graphs given in Figs. 2.1, 2.2, and 2.3. The adjacency matrices for each of these graphs respectively are,

$$\mathbf{A} = \begin{bmatrix} 0 & 0 & 1 & 0 & 1 \\ 0 & 0 & 0 & 1 & 1 \\ 1 & 0 & 0 & 1 & 1 \\ 0 & 1 & 1 & 0 & 0 \\ 1 & 1 & 1 & 0 & 0 \end{bmatrix}, \mathbf{A} = \begin{bmatrix} 0 & 0 & 1 & 0 & 0 \\ 0 & 2 & 0 & 0 & 2 \\ 1 & 0 & 0 & 1 & 1 \\ 0 & 0 & 1 & 0 & 0 \\ 0 & 2 & 1 & 0 & 0 \end{bmatrix}, \mathbf{A} = \begin{bmatrix} 0 & 0 & 0 & 0 & 1 \\ 1 & 0 & 0 & 0 & 0 \\ 0 & 0 & 0 & 1 & 1 \\ 0 & 1 & 0 & 0 & 0 \\ 0 & 0 & 1 & 0 & 0 \end{bmatrix}, \quad (2.8)$$

where the vertices, $\{a, b, c, d, e\}$, are replaced by the matrix indices $\{1, 2, 3, 4, 5\}$, respectively.

Definition 2.8 (Adjacency Matrix of a Weighted (un)directed Graph with no parallel edges). The adjacency matrix, \mathbf{W} , of a weighted graph $G = (V, E, \omega)$, with no parallel edges is given by,

$$W_{ij} = \begin{cases} \omega(\{i, j\}) & \text{if } \{i, j\} \in E \\ 0 & \text{otherwise,} \end{cases} \quad (2.9)$$

in the case of an undirected graph, and

$$W_{ij} = \begin{cases} \omega((i, j)) & \text{if } (i, j) \in E \\ 0 & \text{otherwise,} \end{cases} \quad (2.10)$$

in the case of directed graph. Hence, the adjacency matrix is simply the weights, ω , on edges and zero if the edge does not exist.

It is important to note that it is not possible represent a general weighted graph with parallel edges as an adjacency matrix as it is not fully determined by the matrix. A decision must be made on how to represent parallel edges in the matrix, for example, summing the weights for all edges connecting the same vertices. However, in this case, the state of the original graph cannot be recovered as it is unknown how many parallel edges there are, or what their weights are based on such an adjacency matrix.

Definition 2.9 (Adjacency matrices of a Discrete-Time Temporal Graph). The adjacency matrix, $\mathcal{A}^{[t_k]}$, of a discrete-time temporal graph, $\mathcal{G} = (G_{t_1}, G_{t_2}, \dots, G_{t_{n_t}})$, at time t_k , is simply given as the adjacency matrix of the graph, G_{t_k} .

In other words, a discrete-time temporal graph is represented by a sequence of adjacency matrices, where the particular definition of the adjacency matrix is dependent on what kind of graph is used to represent each of the snapshots in the temporal graph.

These matrix representations are used to develop methods and algorithms that a deeper insight into structure of particular networks and help answer questions such as, “which vertices are most important?” or “which vertices appear in the

most number of shortest paths?”.

2.1.3 Network Properties and Measures

In this section we present a number of fundamental concepts in network science which relate to the overall structure of a graph, both at a microscopic (i.e., vertices) and macroscopic (i.e., graph) level. An important question often asked of graphs, is which vertices are most important, according to some metric. A measure that attempts to answer such a question is called a measure of centrality. However, many attempts to classify this idea of importance depends on things such the vertex’s neighbours, or how many shortest paths it appears in etc.

Walks on Graphs

When analysing networks, there is often a need to discuss the ways in which it is possible to traverse the graph and the effects these walks have. However, before we discuss these topics, we introduce some terminology used when discussing possible “walks” on graphs. For example, a walk may represent the flights taken to from one location to another in an air transport network [41], or represent the order of contacts in a social network in which a disease has spread [117].

Definition 2.10 (Walk). A walk [28] on a graph, $G = (V, E, \psi)$, is an alternating sequence of not necessarily unique vertices and edges, $(v_1, e_1, v_2, e_2, v_3, e_3, \dots)$, which starts and ends with a vertex. Each edge, e_i , is incident with the vertices that precede and proceed it, i.e., $\psi(e_i) = (v_i, v_{i+1})$ and similarly for an undirected graph. In a simple graph, the walk may be fully determined by its sequence of vertices (v_1, v_2, \dots) as there are no parallel edges.

Definition 2.11 (Path). A path [28] is a finite walk in which all edges in the sequence are unique. This induces a simple graph which is sometimes used as the definition of a path.

Definition 2.12 (time-Respecting Path). Suppose we have a discrete-time temporal graph $\mathcal{G} = (G_{t_1}, G_{t_2}, \dots, G_{t_{n_t}})$, where $G_{t_i} = (V, E_{t_i})$. The set E_{t_i} , refers

to the edge set at time t_i . Then a time-respecting path, is a path given by $(v_1, e_1, v_2, e_2, \dots, v_k, e_k, v_{k+1})$, such that $e_i \in E_{t_{j_i}}$, implies that $t_{j_1} < t_{j_2} < \dots < t_{j_k}$.

Definition 2.13 (Non-Backtracking Path). A non-backtracking path, is a path $(v_1, e_1, v_2, e_2, \dots, v_k, e_k, v_{k+1})$, such that for its sequence of vertices, (v_1, v_2, \dots, v_k) , for each double that appears (v_i, v_{i+1}) , it may only appear once, and its reverse, (v_{i+1}, v_i) may not appear at all.

Definition 2.14 (Non-Backtracking Path). Suppose we have a discrete-time temporal graph $\mathcal{G} = (G_1, G_2, \dots, G_{n_t})$, where $G_i = (V, E_i)$. The set E_i , refers to the edge set at time t_i , and of course, $t_1 < t_2 < \dots, t_{n_t}$. Then a time-respecting non-backtracking cycle, is a cycle $(v_1, e_1, v_2, e_2, \dots, v_k, e_k, v_1)$ (as defined in Sec. 2.1.1), where $e_1 \in E_{i_1}, e_2 \in E_{i_2}, \dots, e_k \in E_{i_k}$ and $i_1 < i_2 < \dots < i_k$. Also, for the subsequence of vertices, (v_1, v_2, \dots, v_k) , for each double that appears (v_i, v_{i+1}) , it may only appear once, and its reverse, (v_{i+1}, v_i) may not appear at all.

Definition 2.15 (Cycle). A cycle [28] is a finite walk in which all edges and vertices in the sequence are unique except for the first and last vertex which are the same.

Definition 2.16 (Distance). The distance between two vertices is the number of edges traversed in the shortest possible path (as defined above) between two vertices. For weighted graphs, this is generalised to the path with smallest possible sum of edge weights in the path.

Connectedness

With the above definitions related to walks in mind, we consider the idea of *contentedness* of a graph. This tells us whether or not every vertex in a graph is reachable (i.e. there exists a path) from every other vertex. However, this idea of connectedness depends on whether the graph is directed or undirected. Components of graph are used to describe the number of sub-graphs in which every vertex is reachable by every other.

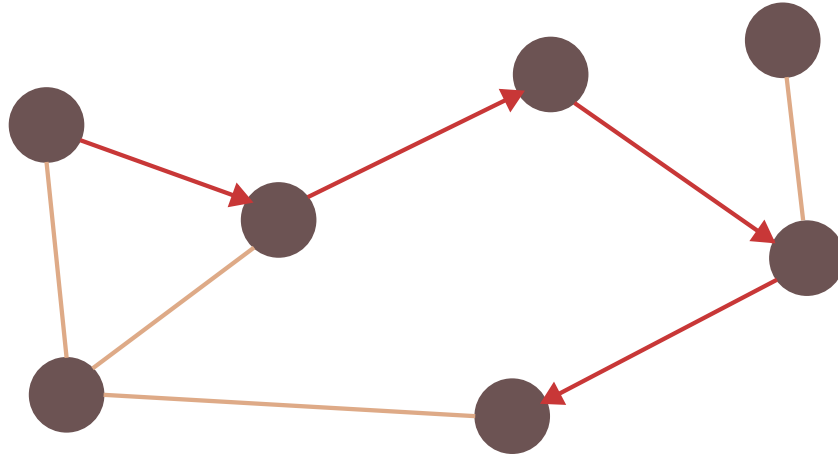


Figure 2.4: An example of a walk on a simple graph. The walk starts from the vertex in the top left and follows the edges denoted as red arrows (in the direction of the arrows), until it reaches its final vertex in the bottom right.

Definition 2.17 (Connected). An undirected graph is connected if there exists a path between every vertex. A connected sub-graph of a graph is called a *connected component* if it is connected and there does not exist another larger connected sub-graph containing it.

Definition 2.18 (Strongly Connected). A directed graph is strongly connected if there exists a path between every vertex. A strongly connected sub-graph of a graph is called a *strongly connected component* if it is strongly connected and there does not exist another larger strongly connected sub-graph containing it.

Definition 2.19 (Weakly Connected). A directed graph is weakly connected if there exists a path between every vertex in an equivalent graph where the reciprocal of each edge is added. A weakly connected sub-graph of a graph is called a *weakly connected component* if it is weakly connected and there does not exist another larger weakly connected sub-graph containing it.

It is often the case that algorithms assume that a graph is fully connected (cf. centrality measures later in this section) for ease of description. However, this usually does not pose a problem as the algorithms can simply be applied to the connected components of a graph should it be disconnected. See Fig. 2.5 for an example of a disconnected graph with 3 connected components.

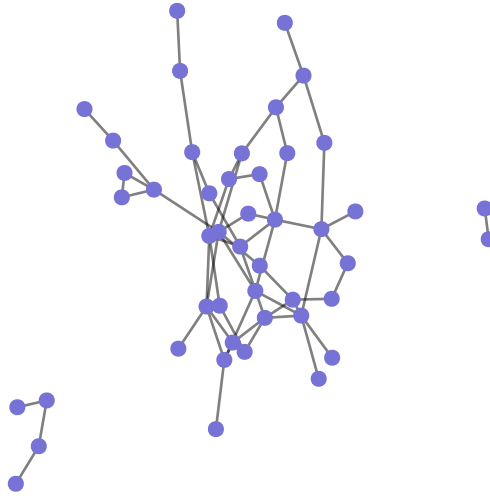


Figure 2.5: An example of an undirected graph with 3 components.

Degree

We now attempt to quantify how important a given vertex is in a graph in relation to other vertices. One of the most simple such measures for quantifying this idea of importance is that of the *degree* [145]. The degree of vertex in an unweighted graph is a count of the number of vertices it is adjacent with. In terms of the adjacency matrix, \mathbf{A} , of a graph, $G = (V, E, \psi)$, the degree of an undirected graph is given by,

$$\deg(i) = \sum_{k \in V} A_{ik} = \sum_{k \in V} A_{ki}. \quad (2.11)$$

For directed graphs, degree is split into in-degree and out-degree as edges are not reciprocal, and thus the adjacency matrix is not symmetric. The in-degree is given by,

$$\deg^{\text{in}}(i) = \sum_{k \in V} A_{ki}, \quad (2.12)$$

and the out-degree is given by,

$$\deg^{\text{out}}(i) = \sum_{k \in V} A_{ik}. \quad (2.13)$$

For weighted graphs, the definition remains the same, and so degree in a weighted graph can be thought of the sum of the weights in/out of vertex. The left panel in Fig. 2.6 shows an example of a random graph with 30 vertices where the probability of connection was 0.1. The color of the vertices represent their degree with a darker colour meaning higher degree.

The distribution of the degree of each vertex in a graph is referred to as the *degree distribution* and turns out to be an incredibly useful tool for categorising types of graphs. For example, take a random graph [60], also known as an Erdős-Rényi graph. That is, a graph with n_v vertices with the probability of an edge existing between any 2 vertices as being p . Then it can be shown that the distribution of the degrees within such a network follow a binomial distribution [18],

$$P(k) = \binom{n_v - 1}{k} p^k (1 - p)^{n_v - k - 1}, \quad (2.14)$$

where $P(k)$ is the probability of a vertex having degree k .

In a similar fashion, the Albert-Barabási model [16] is another type of random graph with a slightly different construction. It starts with a number of vertices, and then progressively adds new vertices with n edges out at each step. The edges are connected to the existing vertices in the graph with a probability proportional to their current degree, or out degree for a directed graph ($p = \deg(i) / \sum_{k \in V} \deg(k)$), this is referred to as preferential attachment. As shown in the original paper [16], the degree distribution of such a graph follows,

$$P(k) \sim k^{-\gamma} \quad (2.15)$$

where γ is some positive value. This type of degree distribution is seen in numerous examples in nature [17] and is characterised by its scale-free nature, hence, graphs with this property are often called *scale-free networks*. The middle panel

in Fig. 2.6 shows an example of an Albert-Barabási network. The initial number of vertices was 2 with a degree of 0, at each step, a vertex was added with 2 outgoing edges until 30 vertices was reached. Similar to the other plots, color of the vertices represent their degree with a darker colour meaning higher degree.

The last type of random graph we will look at is the Watts-Strogatz graph [196] or *small-world graph*. This is another type of important random graph which emerges from a specific construction. We start with a k -regular ring lattice graph with n_v vertices, that is, a graph where every vertex is placed on a ring and then connected to the $k/2$ closest vertices on their left and right (every vertex has degree k). Then, each edge is re-wired with some probability p . That means one of the vertices the edge is incident with is randomly reassigned. This leads to a network with a very small deviation in the degree distribution and has an average degree very close to k (for small p). The important feature of this graph, is that it makes the average distance between vertices very small (hence small-world) and produces a clustering coefficient which is relatively high for small p . This helped provide a greater understanding of the *6 degrees of separation* phenomenon [1], in which it is often seen that given any two people in the world, the average number *connections* (acquaintances of acquaintances) it takes for them to reach each other is 6. The right panel in Fig. 2.6 shows an example of a Watts-Strogatz network. The graph contains 30 vertices, where each vertex started with 4 edges. With probability $p = 0.1$, each edge was rewired.

Eigenvector Centrality

While degree centrality is useful in its own right, it is a rather basic description of importance. Often, the importance of vertex in a network is dependent also on the importance of the vertices that interact with it. This is where eigenvector centrality [145] can be of use, its measure of importance depends not only on neighbours, but also on the importance of those neighbours. Eigenvector centrality is, as the name suggest, a measure of a vertex's importance based of the eigenvector associated with the largest eigenvalue of the adjacency matrix. Suppose the vertex

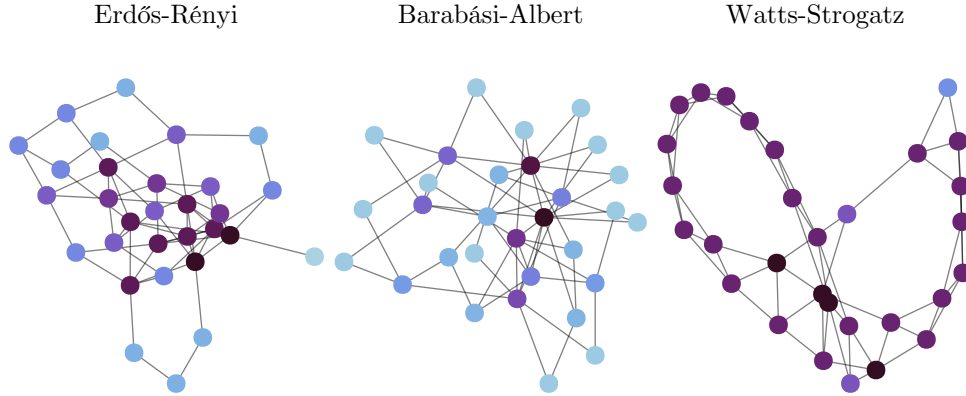


Figure 2.6: An example of 3 graphs characterised by their degree distribution. The colour of each vertex is determined of the degree of the vertex. A light colour (blue) indicates low degree whereas dark colour (purple/black) indicates a high degree. Each graph has 30 vertices. In the left plot the probability of an edge between vertices was $p = 0.1$. In the middle plot, the Albert-Barabási model started with 2 unconnected vertices, at each step a vertex was added with 2 edges until 30 vertices was reached. The probability that one of the edges was assigned to an already existing vertex i was given by $p = \deg(i) / \sum_{k \in V} \deg(k)$. In the plot on the right, the Watts-Strogatz model started as 4-regular graph where each edge was rewired with a probability of $p = 0.1$.

set of the (un)directed graph is simply a list of integers, $V = \{1, 2, \dots, n_v\}$, then the eigenvector centrality of the i th vertex is given as the solution to,

$$c_i = \frac{1}{\lambda} \sum_{k \in V} A_{ik} c_k, \quad (2.16)$$

where c_i (a positive value) is the eigenvector centrality of vertex i . This is simply the definition of an eigenvector re-written in a component-wise fashion. By the Perron-Frobenius theorem [145], there is only one eigenvector of \mathbf{A} that is all positive, and its associated with its largest eigenvalue. This is only true if the graph is strongly connected, and so, the centrality measure is only defined on strongly connected graphs (an unconnected graph can always be split into its strongly connected components). In matrix notation this is written as,

$$\mathbf{A}\mathbf{c} = \lambda\mathbf{c}, \quad (2.17)$$

where \mathbf{c} is the vector of centrality components (also an eigenvector) $\mathbf{c} = [c_1, \dots, c_{n_v}]^T$.

From eigenvector centrality, there are number of related extensions. Most notably, these are Katz [107] and Page Rank [151] centrality, the latter of which was developed by Larry Page for the Google search algorithm. These both attempt to fix flaws in the original eigenvector centrality that appear under certain conditions. Suppose that a directed graph has no outgoing edges from a vertex i , then c_i as defined above would be 0, even if every other vertex had an out-edge into i . In many cases this vertex i should have some level of importance greater than 0.

Katz centrality is defined by the solution to,

$$\mathbf{c} = \lambda^{-1} \mathbf{A} \mathbf{c} + \beta \mathbf{1}. \quad (2.18)$$

This is related to the original eigenvector centrality as in Eq. (2.17) by adding some non-zero parameter, β to every component. This allows vertices with no out-edges to attain a non-zero level of importance, depending on the importance of the vertices that have edges into the vertex. The parameter β is often set to 1 as it has no effect on the relative difference between the Katz centrality of each vertex. The parameter λ is usually chosen to be smaller than the largest eigenvalue of \mathbf{A} , as the solution to the above equation is not defined when λ is set equal to the largest eigenvalue, and iterative methods will diverge if it is larger (by properties of the spectral radius [120]).

The potential problem that Page rank centrality attempts to fix in both eigenvector and Katz centrality is that a vertex that has an in-edge from important vertices will also be ranked highly important. This is not always necessarily a problem. However, considering Page rank was designed with ranking web pages in mind, this would clearly be a problem as there are websites with potentially millions of hyper-links out. This would lead to scenarios where my personal blog would be ranked as highly as Amazon.com if it were to link to my site. This problem is averted by weighting the adjacency matrix by the inverse of the out-degree of the incoming vertex. The Page rank centrality is given as the solution to,

$$\mathbf{c} = \lambda^{-1} \mathbf{A} \mathbf{D}^{-1} \mathbf{c} + \beta \mathbf{1}, \quad (2.19)$$

where $\mathbf{D} = \text{diag}([\text{deg}^{\text{out}}(1), \dots, \text{deg}^{\text{out}}(n_v)]^T)$. This has the effect of diluting the amount of importance a vertex has to divvy out proportionally to the inverse of its out degree. Values for β and λ are chosen by the same reasoning as in Katz centrality.

In Fig. 2.7 we compare the centrality measures on the same random Erdős-Rényi graph with 30 vertices and a probability of connection of $p = 0.1$. The centralities were scaled such that their max value is 1 and the colour indicates the level of centrality of vertex, with darker indicating higher centrality. Some of the problems with eigenvector centrality as discussed earlier can be seen. Take the vertex in top right for example. In eigenvector centrality it has a measure of 0 due to having no out links, even though it's pointed to by a vertex with a high number of edges. This problem does not appear in the other types of centrality indicated by the colour of the vertex. It is also apparent that the most important vertex in each case is different. A certain measure of centrality is not necessarily better than any other as it is quite dependent on what important means in the context.

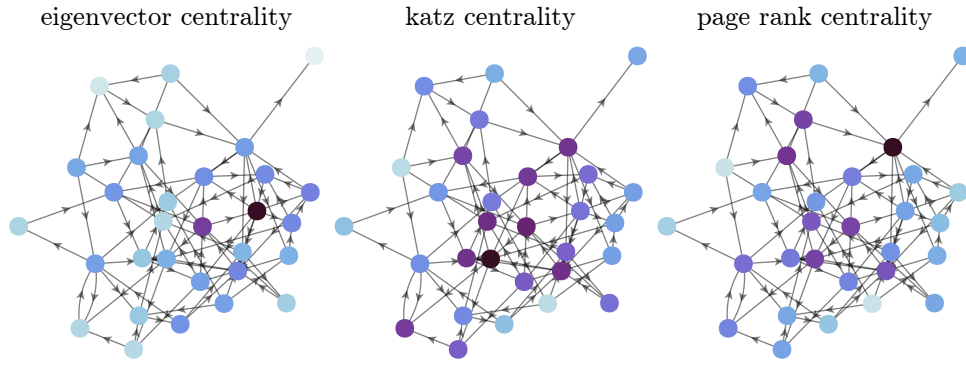


Figure 2.7: The eigenvector, Katz, and Page rank centrality on the same Erdős-Rényi graph with 30 vertices and a probability of connection of $p = 0.1$. The left panel shows eigenvector centrality, the middle panel shows Katz centrality and the right panel shows Page rank centrality. In all cases the centrality values were rescaled by dividing by their max value such that the maximum centrality is given as 1. The colour of each vertex indicates its measure of centrality with darker indicating higher centrality.

Closeness and Betweenness Centrality

Instead of using eigenvector based methods for measuring centrality, it is possible to instead define it using shortest paths. While related to the previously described eigenvector methods, they quantify importance in a slightly different way. Two such popular measures of centrality are closeness [21] and betweenness [197]. Closeness centrality determines the importance of vertex based on its average distance to every vertex. The closeness of vertex i is defined as,

$$c_i = \frac{1}{\sum_{k \in V} d(i, k)}, \quad (2.20)$$

where $d(i, k)$ is the distance between i and k . In other words, it's the inverse of the sum of all distances out of a vertex. This is useful for determining how easy it is to travel from one vertex to another. As in the case of the Watts-Strogatz model, it is identified by a very low average closeness.

Betweenness is a similar concept built on top of the idea of shortest paths. However, betweenness centrality determines whether or not a vertex is important depending on the number of shortest paths it is part of. The betweenness of a vertex i is defined as,

$$c_i = \sum_{\substack{k, l \in V \\ k \neq l \neq i}} \frac{\sigma_{kl}(i)}{\sigma_{kl}}, \quad (2.21)$$

where σ_{kl} is the number of shortest paths from vertex k to l and $\sigma_{kl}(i)$ is the number of shortest paths from k to l which go through vertex i . Thus, the higher the number of shortest paths a vertex is part of, the more central a role it plays in the graph. This is particularly important in areas such as power grid management [92], in which vertices represent power stations and edges represent power lines. Vertices with high betweenness would reduce robustness of the network as a whole and make it more susceptible to total failure in the case of an important power station going down.

In Fig. 2.8 we present an example of both closeness and betweenness centrality on the same random network with 30 vertices where each edge has a probability

of occurring of 0.1. The darker colours indicate a higher measure of centrality. We see that both of the examples give the same vertex the highest centrality score, this is expected as a vertex that is in many shortest paths will also be close to many other vertices. However, we see that closeness centrality tends to give a much higher score, particularly to vertices without any in-edges.

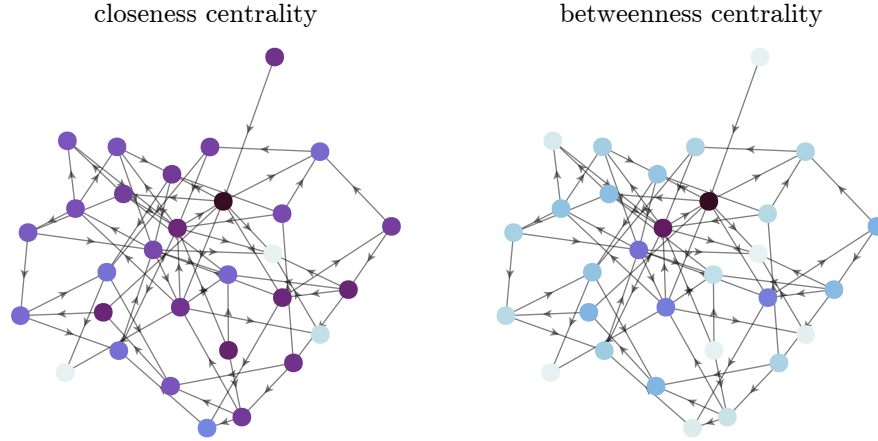


Figure 2.8: The closeness and betweenness centrality on the same Erdős-Rényi graph with 30 vertices and a probability of connection of $p = 0.1$. The left panel shows closeness centrality and the right panel shows betweenness centrality. In all cases the centrality values were rescaled by dividing by their max value such that the maximum centrality is given as 1. The colour of each vertex indicates its measure of centrality with darker indicating higher centrality.

Following our discussion of centrality and measure of importance of vertices in a graph, we note that this plays an important role in network epidemiology [85]. It allows us to infer what vertices in a graph could potentially act as super spreaders, and thus, which vertices should be monitored for outbreak of disease. This can be incredibly useful for diseases such as Bovine Tuberculosis [142], where herds act as vertices and trades between them act as directed edges. However, before we attempt to model the spread of disease on networks, we first discuss epidemiological models which describe the evolution of a disease in well mixed populations. This will give us a grounding in mathematical epidemiology from which we can extend ideas to networks.

2.2 Compartmental Epidemiological Models

Infectious diseases typically display a wide range of clinical symptoms as well as a broad spectrum of transmission dynamics which vary over both temporal and spatial scales when looking at the level of populations. These dynamics are often difficult to concisely and fully capture in a closed model. However, many such diseases display similar characteristics and thus, it is possible to abstract away many of dynamics of specific diseases and class them as belonging to different phenological models which places the population into different classes or compartments based on the characteristics of the disease they are associated with. The most common such groups being those who are susceptible to catching the disease, those who have the disease and are infectious and those who have recovered and are immune or dead. This particular model is discussed in greater detail below.

2.2.1 Ordinary Differential Equation Models

One of the first and most well known mathematical epidemiological models is what is now referred to as the Susceptible-Infected-Recovered (SIR) model, first introduced by Kermack and McKendrick in 1927 [111]. The model defines 3 quantities, the number of susceptible $S(t)$, infected $I(t)$ and recovered $R(t)$ at time t . The evolution of the disease is described by the following set of integro-differential equations,

$$\frac{dS}{dt} = -S(t) \left(- \int_0^t \beta(\theta) e^{-\int_0^\theta \mu(a) da} \frac{dS}{dt}(t-\theta) d\theta + \beta(t) I(0) e^{-\int_0^t \mu(a) da} \right), \quad (2.22a)$$

$$\frac{dI}{dt} = \frac{d}{dt} \left(- \int_0^t e^{-\int_0^\theta \mu(a) da} \frac{dS}{dt}(t-\theta) d\theta + I(0) e^{-\int_0^t \mu(a) da} \right), \quad (2.22b)$$

$$\frac{dR}{dt} = - \int_0^t \mu(\theta) e^{-\int_0^\theta \mu(a) da} \frac{dS}{dt}(t-\theta) d\theta + \mu(t) I(0) e^{-\int_0^t \mu(a) da}, \quad (2.22c)$$

where the following condition must also be satisfied and is a direct result of the above system of equations.

$$N = S(t) + I(t) + R(t). \quad (2.22d)$$

n refers to number of initial individuals in the system and is assumed to remain constant for all time. Mixing within the population is assumed to be uniform and homogeneous. This is an important assumption which will later justify the use of networks to model epidemics later.

The parameters in the above equations are defined as the following. The probability of moving from S to I after being in group S for time t is $\beta(t)$ and the probability of moving from I to R after being in group I for time t is $\mu(t)$. A common assumption used in the context of this model, especially in network science, is to take $\mu(t) \equiv \mu$ and $\beta(t) \equiv \beta$ as constants, which is not the most realistic assumption one can make, but provides a good approximation of the true dynamics none the less. This is because the assumption of constant recovery rate implies that the process is exponentially distributed with rate μ [26] (as shown later in this section). Thus, the average time it takes to recover according to the model is given by $1/\mu$. As a result, one can choose μ to be the inverse of the true average time to recover, and so, the model will match the true average recovery time of the disease.

With the previous assumption we find the following simplifications of the model are attained. By substituting the constant values for β and μ into Eqs. (2.22), we get the following for $\frac{dI}{dt}$,

$$\frac{dI}{dt} = \frac{d}{dt} \left(- \int_0^t e^{-\theta\mu} \frac{dS}{dt} (t - \theta) d\theta + I(0) e^{-t\mu} \right). \quad (2.23)$$

Thus, giving us

$$I(t) = - \int_0^t e^{-\theta\mu} \frac{dS}{dt} (t - \theta) d\theta + I(0) e^{-t\mu}. \quad (2.24)$$

We do the same thing for $\frac{dS}{dt}$ and substitute in the constant values for β and μ

and obtain,

$$\begin{aligned}
 \frac{dS}{dt} &= -S(t) \left(- \int_0^t \beta e^{-\theta\mu} \frac{dS}{dt}(t-\theta) d\theta + \beta I(0) e^{-t\mu} \right), \\
 &= -\beta S(t) \left(- \int_0^t e^{-\theta\mu} \frac{dS}{dt}(t-\theta) d\theta + I(0) e^{-t\mu} \right), \\
 &= -\beta S(t) I(t),
 \end{aligned} \tag{2.25}$$

where the last step is obtained directly from Eq.(2.24). Similarly, we may rewrite $\frac{dR}{dt}$ as the following,

$$\begin{aligned}
 \frac{dR}{dt} &= - \int_0^t \mu e^{-\theta\mu} \frac{dS}{dt}(t-\theta) d\theta + \mu I(0) e^{-t\mu}, \\
 &= \mu I(t).
 \end{aligned} \tag{2.26}$$

Using the simplified formulations for both $\frac{dS}{dt}$ and $\frac{dR}{dt}$, as well as Eq. (2.22d) we may write,

$$\begin{aligned}
 \frac{dI}{dt} &= -\frac{dS}{dt}(t) - \frac{dR}{dt}(t), \\
 &= \beta S(t) I(t) - \mu I(t).
 \end{aligned} \tag{2.27}$$

Combing all the above we arrive at the following system of equations that make quite frequent appearance in literature due to their simple and intuitive nature compared to the original general model of Eqs. (2.22):

$$\frac{dS}{dt} = -\beta S(t) I(t), \tag{2.28a}$$

$$\frac{dI}{dt} = \beta S(t) I(t) - \mu I(t), \tag{2.28b}$$

$$\frac{dR}{dt} = \mu I(t). \tag{2.28c}$$

Now assuming for a moment that we hold the number of susceptibles steady and that no more can be infected, we obtain,

$$\frac{dI}{dt} = -\mu I(t). \tag{2.29}$$

The solution to which may be obtained by rudimentary Ordinary Differential Equation (ODE) techniques [181],

$$I(t) = I(0)e^{-\mu t}. \quad (2.30)$$

From the above equation $I(t)$ gives the number of individuals left infected after time t , meaning that the proportion who have recovered after time t is given by,

$$I(t) = 1 - e^{-\mu t}. \quad (2.31)$$

This is the cumulative distribution function of the exponential distribution with parameter μ , thus implying that the time to recovery according to SIR model is exponentially distributed.

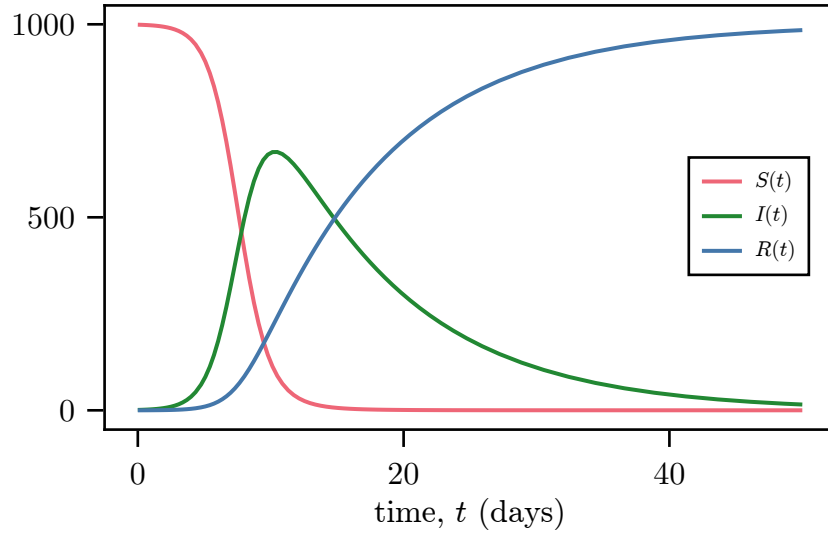


Figure 2.9: An example solution to the SIR model, given by Eqs. (2.22). The parameters used were a population size of $N = 1000$, $\beta = 1/1000$ and $\mu = 1/10$. The initial conditions were set to $I(0) = 1$ and $S(0) = 999$ and the system was integrated from $t = 0$ to $t = 50$.

We show an example solution of the SIR model for a population of $N = 1000$ in Fig. 2.9. $S(t)$ is given by the red line, $I(t)$ is given by the green line and $R(t)$ is given by the blue line. The parameters used were $\beta = 1/10000$ and $\mu = 1/10$, with initial conditions of $S(0) = 999$, $I(0) = 1$, and $R(0) = 0$.

This formulation, which is a direct consequence of the original SIR model, is sometimes referred to as *density dependent*. This is due to the fact that the force of infection $\beta I(t)$ is directly proportional to the number of infected. An alternative formulation is often used and is what is referred to as *frequency dependent* and is given as,

$$\frac{dS}{dt} = -\beta \frac{S(t)I(t)}{N}, \quad (2.32a)$$

$$\frac{dI}{dt} = \beta \frac{S(t)I(t)}{N} - \mu I(t), \quad (2.32b)$$

$$\frac{dR}{dt} = \mu I(t). \quad (2.32c)$$

The term frequency dependent is used because the force of infection in this case, $\frac{\beta I(t)}{N}$, is no longer dependent on the population size but the fraction of individuals who are infected. For the rest of the chapter we shall use the density dependent formulation unless specified otherwise.

While the SIR model remains popular, likely due to a mixture of simplicity, history and range of qualitative behaviour, there are numerous such compartment models in literature. There are the Susceptible-Infected-Recovered-Susceptible (SIRS) [179], Susceptible-Infected-Susceptible (SIS) [189] and Susceptible-Exposed-Infected-Recovered (SEIR) [124] just to name a few. Each of these compartments adds a new set of dynamics (or even just a sub-population) to an epidemiological model. For example, in the previous examples, the SEIR model adds an *exposed* compartment to the SIR model. This allows for the latent effects of a disease to be modelled [90], helping to improve realism in the model as often it takes a number of days for an infected person to become infectious, depending on the disease. Other compartments sometimes seen are vaccinated [52] or quarantining [5] individuals.

2.2.2 Stability Analysis

When dealing with such epidemiological models often the goal is not to model or predict exactly the number of infected individuals at a given period of time, but rather, investigate what scenarios could give rise to epidemics or vice versa. This leads naturally to the area of stability analysis of fixed points. The fixed points of the SIR model are all such points, $[S^*, I^*, R^*]^T$, (superscript T is used to denote the transpose) for which the ODEs defining the model as in Eqs. (2.28) attain the value zero. This corresponds to the solutions of the following set of equations

$$-\beta S^* I^* = 0, \tag{2.33a}$$

$$\beta S^* I^* - \mu I^* = 0, \tag{2.33b}$$

$$\mu I^* = 0. \tag{2.33c}$$

This implies that if the system were to start with initial conditions $[S^*, I^*, R^*]^T$, the system would stay at this state for all of time. From Eqs. 2.33, it is clear that the fixed points of the system are any points which satisfy $[S^*, 0, R^*]^T$ and $S^* + R^* = N$. This makes intuitive sense as if there are no infected in the system, no more can be produced and the susceptible and recovered remain at the same levels for all time, assuming the total population, N , remains constant. It is worth noting that no endemic fixed points are possible with the standard SIR model, i.e., a fixed point with non-zero infected individuals. In order for such a fixed point to be possible variable populations must be introduced, which is often done by adding birth and death dynamics.

It is unsurprising that a system with no infected individuals will not produce any. As such, a better question may be for what parameters β and μ would an epidemic occur should the system be perturbed slightly from its fixed point of $[S^*, 0, R^*]^T$. To give the disease the best chance at producing an epidemic we start with the fixed point $[N, 0, 0]^T$, which we shall refer to as the Basic Disease-Free Equilibrium (basic DFE). We define an epidemic in the SIR model as instability of the basic DFE.

Assume that $0 < \delta \ll 1$ and perturb the basic DFE such that the state of the system at time 0 is $[N - \delta, \delta, 0]^T$ which is approximately $[N, \delta, 0]^T$ due to N being much larger than δ . Thus, at time 0 we have,

$$\frac{dI}{dt}(0) > 0 \iff \frac{N\beta}{\mu} > 1. \quad (2.34)$$

This gives the condition that in order for an epidemic to occur in the SIR model, at the basic DFE, the parameters must satisfy the condition that $\frac{N\beta}{\mu} > 1$. In the frequency dependent formulation this condition is also independent of the population size and is given by $\frac{\beta}{\mu} > 1$. This quantity is what is often referred to in literature as the basic reproduction number, \mathcal{R}_0 [190]. That is, the number of expected secondary cases produced by a single infected individual. This quantity can be more formally derived by computation of the next-generation matrix [54, 190], a method we will use in Sec. 2.3.2. When this value is greater than one, the number of infected in the system will increase over time.

In order to demonstrate the long-term effects of the basic reproduction number \mathcal{R}_0 , we define R_∞ , called the *outbreak size* as the limit of the number of recovered as time goes to infinity, i.e.,

$$R_\infty = \lim_{t \rightarrow \infty} R(t). \quad (2.35)$$

This quantity tells us how many individuals in the system became infected over the course of an outbreak due to the fact that $\lim_{t \rightarrow \infty} I(t) = 0$. From Ref. [37], this can be shown to be the solution to the equation

$$1 - R_\infty - e^{-\mathcal{R}_0 R_\infty} = 0, \quad (2.36)$$

which is a function of the basic reproduction number \mathcal{R}_0 . We show the outbreak sizes for a population of $N = 1000$ in Fig. 2.10. We assume a value of $\mu = 1/10$ and then vary the values of β such that \mathcal{R}_0 varies from 0 to 4. As is clearly evident from the plot, for $\mathcal{R}_0 > 1$ the outbreak size, R_∞ , begins to quickly increase giving rise to an epidemic.

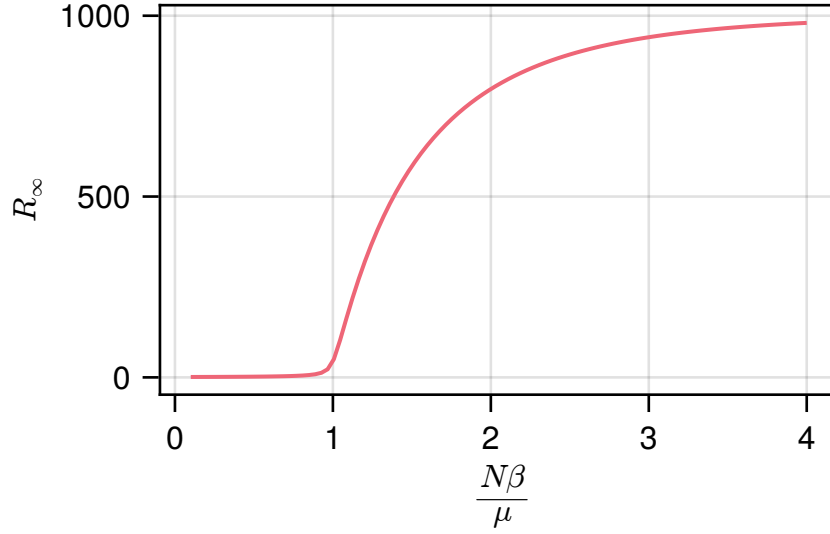


Figure 2.10: The final outbreak sizes for the SIR model against the reproduction number $\mathcal{R}_0 = N\beta/\mu$. The parameters used were $\mu = 1/10$ and β ranging from $1/10000$ to $1/2500$.

2.3 Network Epidemiological Models

One of the main assumptions in the previously discussed ODE models for modelling epidemics is the assumption that the population is well mixed. This assumption may be a good approximation for small areas with little to no interaction with individuals outside the given area. However, such areas in today's world are few and far between. When modelling on the scale of countries it is not feasible to assume that individuals who are thousands of kilometers away are just as likely to interact as with their neighbours. The goal of this section is to introduce techniques for modelling epidemics on networks, thus taking into account heterogeneous contact and interaction patterns. Due to combinatorial explosion in combinations of contact chains when dealing with networks, some trade-offs must be made by ignoring causal relationships when formulating probabilities of infection occurring, this will be first seen in the Individual-Based (IB) model.

First we describe a static contact network. Let $G = (V, E)$ be a simple undirected graph (note we drop the incidence function ψ for a simple graph)

which represents the usual contact patterns in a population. $V = \{1, 2, \dots, n_v\}$ is the set of vertices which represent individuals. $E \subseteq \{\{i, j\} | i, j \in V\}$ is the set of edges which represents a contact between individuals. n_v is the number of vertices and n_e is the number of edges.

Rather than describing the expected number infected as in the case of the well mixed ODE epidemiological models, when dealing with networks we shall instead describe the probability of a particular vertex/individual belonging to a given compartment in the epidemiological model. We let Ω be the set of compartments or states which the vertices may attain. For example, in the SI or SIS model, $\Omega = \{S, I\}$, in the case of the SEIR or SEIRS model $\Omega = \{S, E, I, R\}$ etc. However, we will continue with the example of the SIR model for consistency. In this case we have $\Omega = \{S, I, R\}$.

With each vertex, we associate a state, u_i , which describes the compartment vertex i belongs to. For example, we may have $u_i = S$, $u_i = I$ or $u_i = R$ etc. in the SIR model. We will use the more compact notation s_i to imply $u_i = S$ and similarly for I and R . Clearly, we have $u_i \in \Omega$. The state vector of the entire network is then given by $\mathbf{u} = (u_1, u_2, \dots, u_{n_v})^T$, which has $|\Omega|^{n_v} = 3^{n_v}$ state combinations. Clearly, this is a huge number even for relatively small graphs.

By assuming that the infection process is a Markovian process, we may use the master equation to move the system forward in time. We let $P(\mathbf{u}, t)$ denote the probability of the network being in state \mathbf{u} at time t and $W(\mathbf{u}|\mathbf{v}, t)$ denote the transition rate of moving to state \mathbf{u} given the network is in state \mathbf{v} at time t . The rate of change of the probability of the vertices being in the combination of states \mathbf{u} at time t is given by the relation,

$$\frac{\partial P}{\partial t} = \sum_{\mathbf{v} \neq \mathbf{u} \in \Omega^{n_v}} [W(\mathbf{v}|\mathbf{u}, t)P(\mathbf{u}, t) - W(\mathbf{u}|\mathbf{v}, t)P(\mathbf{v}, t)]. \quad (2.37)$$

This would be a huge computational task to compute the probability of all combinations of states at each time step for graphs with many vertices.

2.3.1 Individual-Based Model

A compromise must be made between correctness and computability of the problem. The first port of call, as with many probabilistic problems, is to assume statistical independence in the state of vertices, essentially forgetting all their past interactions. In this case, the probability of a vertex changing state is only dependent on the current state of its neighbours. This assumption of independence is what is referred to as an IB model. With the assumption of independence, we write the IB model by describing the marginal probabilities of the network via a system of ODEs. We let $P_{S_i}(t)$, $P_{I_i}(t)$ and $P_{R_i}(t)$ denote the marginal probabilities of vertex i being in state S , I and R respectively at time t . This produces a far smaller system of $3n_v - 1$ equations compared to the $3^{n_v} - 1$ needed for the full master equation description as in Eq. (2.37). This is due to the fact that the master equation sums over the probability of every single combination of possible states, which for the SIR model is number of compartments to the power of the number of vertices. The minus 1 is due to the fact that an equation may be left out as total probability must always be conserved. This reduced system can be rigorously derived from the master equation, as we will see in Chp. 3.

We assume that \mathbf{A} is the adjacency matrix for the graph G which represents contacts in the network. Assuming β is the transition rate of becoming infected on contact with an infectious individual, the transition rate of a vertex, i , moving from susceptible to infected is given by the quantity $\beta \sum_{j \in V} A_{ij} P_{I_j}(t)$. With this quantity in mind, we may write the ODEs for the IB model as,

$$\frac{dP_{S_i}}{dt} = -\beta \sum_{j \in V} A_{ij} P_{I_j}(t) P_{S_i}(t), \quad (2.38a)$$

$$\frac{dP_{I_i}}{dt} = \beta \sum_{j \in V} A_{ij} P_{I_j}(t) P_{S_i}(t) - \mu P_{I_i}(t), \quad (2.38b)$$

$$\frac{dP_{R_i}}{dt} = \mu P_{I_i}(t). \quad (2.38c)$$

such that

$$P_{S_i} + P_{I_i} + P_{R_i} = 1, \quad (2.38d)$$

and where μ is the transition rate of moving from the I to the R compartment, i.e., the rate of removal or recovery.

The above set of equations are the time continuous version of the IB model. It is often the case that a time discrete version is preferred due to the fact that temporal networks are often considered as discrete snapshots. The discrete time version is given as,

$$\frac{dP_{S_i}}{dt} = - \left[\prod_{j \in V} (1 - \beta A_{ij} P_{I_j}(t)) - 1 \right] P_{S_i}(t), \quad (2.39a)$$

$$\frac{dP_{I_i}}{dt} = \left[\prod_{j \in V} (1 - \beta A_{ij} P_{I_j}(t)) - 1 \right] P_{S_i}(t) - \mu P_{I_i}(t), \quad (2.39b)$$

$$\frac{dP_{R_i}}{dt} = \mu P_{I_i}(t). \quad (2.39c)$$

Although they are similar in description, the β parameters in both the continuous and discrete time models of the network IB model represent different quantities with the former being a transition rate and the latter being a probability.

As in the case of the well mixed SIR model, stability analysis may also be performed on epidemiological network models. For this analysis, it is easier to use the linearised version of the model given by Eqs. (2.38). Due to the nature of the system, it may be written in a more concise matrix description. Let $\mathbf{P}_S(t) = [P_{S_1}(t), P_{S_2}(t), \dots, P_{S_{n_v}}(t)]^T$ be the vector of marginal probabilities of the system being entirely in the susceptible compartment. Similarly for \mathbf{P}_I and \mathbf{P}_R . We may then rewrite the system as,

$$\frac{d\mathbf{P}_S}{dt} = -\beta \mathbf{P}_S^T(t) \mathbf{A} \mathbf{P}_I(t), \quad (2.40a)$$

$$\frac{d\mathbf{P}_I}{dt} = \beta \mathbf{P}_S^T(t) \mathbf{A} \mathbf{P}_I(t) - \mu \mathbf{P}_I(t), \quad (2.40b)$$

$$\frac{d\mathbf{P}_R}{dt} = \mu \mathbf{P}_I(t). \quad (2.40c)$$

The fixed points of the system, $[\mathbf{P}_S^{*T}, \mathbf{P}_I^{*T}, \mathbf{P}_R^{*T}]^T$, are the values for which the derivatives in Eqs. (2.40), attain the value zero. It is straight forward to show

that the only fixed points in the system are of the form $[\mathbf{P}_S^{*T}, 0, \mathbf{P}_R^{*T}]^T$, where $\mathbf{P}_S^* + \mathbf{P}_R^* = \mathbf{1}$. This is the same as we saw in the well mixed case (cf. Sec. 2.2.2), where no infected individuals implies that no more can be introduced to the population, as such, the number of susceptible and recovered remains constant for all time.

In the network case, we define an epidemic in terms of instability of the basic DFE, that is, instability of the fixed point $[\mathbf{1}^T, \mathbf{0}^T, \mathbf{0}^T]^T$. Thus, we start from a perturbed basic DFE, $[(\mathbf{1} - \boldsymbol{\delta})^T, \boldsymbol{\delta}^T, \mathbf{0}^T]^T$, which is approximately equal to $[\mathbf{1}^T, \boldsymbol{\delta}^T, \mathbf{0}^T]^T$ where $\boldsymbol{\delta} = [\delta_1, \dots, \delta_{n_v}]^T$ and for all $i \in V$, $0 < \delta_i \ll 1$. Substituting this value into Eq. (2.40b) gives,

$$\frac{d\mathbf{P}_I}{dt} = (\beta\mathbf{A} - \mu\mathbf{Id})\boldsymbol{\delta}, \quad (2.41)$$

where \mathbf{Id} is the identity matrix. Standard analysis of linear systems tells us that this system is unstable if the largest eigenvalue, λ_{\max} , of $\beta\mathbf{A} - \mu\mathbf{Id}$ is greater than zero. λ_{\max} is given by the largest solution of λ to the characteristic equation,

$$\det(\beta\mathbf{A} - \mu\mathbf{Id} - \lambda\mathbf{Id}) = \det\left(\mathbf{A} - \frac{(\mu + \lambda)}{\beta}\mathbf{Id}\right) = 0. \quad (2.42)$$

Thus, the largest eigenvalue of the matrix \mathbf{A} , which we will call σ_{\max} , is related to λ_{\max} by,

$$\sigma_{\max} = \frac{\mu + \lambda_{\max}}{\beta}, \quad (2.43)$$

which implies that $\lambda_{\max} > 0$ when $\sigma_{\max} > \frac{\mu}{\beta}$. This is the necessary condition for an epidemic to occur on average in the IB SIR model. This is sometimes referred to as the *epidemic threshold* (cf. Sec. 2.2.2). Unsurprisingly, this is the same quantity produced in the well mixed case, although the parameters carry different meanings.

In Chp. 3 we will see this model extended to the Pair-Based (PB) model which no longer assumes independence between the states of vertices, but instead assumes conditional independence between triples of vertices, thus increasing accuracy by reducing the likelihood of echo chambers forming (see Fig. 3.2).

2.3.2 Meta-Population Models

In this section, we introduce the concept of epidemiological *meta-population models* [22, 42, 43, 87]. This class of models may be thought of as compromise between the well mixed ODE models (see Sec. 2.2.1) and the network models described in the previous section. As mentioned previously, there is merit in models which assume homogeneous mixing, as long as that assumption is true, or at least approximately true. With meta-population models, the population is split up into a number of groups which will correspond to the vertices in a graph. These groups are chosen based on individuals' geographical proximity. It is assumed that within these groups, the individuals are close enough together that it is justified to assume they mix in a uniform manner. It is even possible to use these models at the level of household [95], however this sort of granularity requires a lot of data and strong assumptions of individuals contact patterns. Thus, the well mixed models may be used to model the spread of disease within each group. However, movement of individuals between groups is allowed via travel/commuting [193] etc. These travelling individuals correspond to edges in the graph. This allows infected individuals to spread disease outside their home group/vertex, thus, allowing the disease to spread throughout the overall population. Parameters can be chosen specific to each geographical location [3, 109] which may represent things like number of hospitals present or education level etc. This can produce more realistic behaviour by making it more difficult for a disease to take hold in certain locations. The use of commuting/travel networks gives rise to more realistic infection patterns in the sense that areas with a large influx of individuals will see the disease break out first, which is often seen in real life examples, with diseases hitting dense cities much harder [161].

These meta-population models can be more useful in practice than the pure network models, as each vertex in the network models represent an individual. When trying to model the spread of disease across large scales, the number of vertices required in the contact network would be in the millions or hundreds of millions making computation of models, such as the IB model, difficult. The meta-population models allow for a huge reduction in the number of vertices re-

quired by allowing a single vertex to represent a large number of people. Another use of the meta-population models comes from the use of empirical data. When commuting/travelling data is available, it will be aggregated to some level, often down to some sort of administrative or geographical areas. Thus, it is relatively straightforward to apply this data to meta-population models by defining vertices as the same such areas.

We now formally define the SIR meta-population model on a network. We have a population in some geographical location we wish to model the spread of disease in. The location is split up into n_v sub-locations labeled from 1 to n_v . Each sub-location i , has a population $N_i(t)$ associated with it. Unlike in the previous case of the SIR model for a single population where we assumed a constant population, the populations associated with each vertex depends on time due the ability of individuals to travel between vertices. We do however, have the sum of the sub-populations conserved by $N = \sum_{i \in V} N_i(t)$, where N is the sum of all sub-populations. The rate at which individuals travel from location i to j is constant and denoted by ω_{ij} . This quantity may be informed by empirical data or generated from mobility models such as the gravity model or radiation model, which will be discussed in the next section (Sec. 2.4). As we will see in Chp. 4, the travel rates may depend on time with the use of a temporal graph. We represent this network of populations and travels between them as a directed weighted graph, $G = (V, E, \omega)$, where the vertices, $V = \{1, \dots, n_v\}$, represent the sub-locations of the same label and the edges, E , represent the rate of travel between the sub-locations. The weights of the edges are the travel rates such that $\omega((i, j)) = \omega_{ij}$. Thus, the weighted adjacency matrix, \mathbf{W} , of G , is given by $\mathbf{W}_{ij} = \omega_{ij}$. For example, in Fig. 2.11, the adjacency matrix is given by,

$$\mathbf{W} = \begin{bmatrix} 0 & \omega_{ab} & \omega_{ac} \\ \omega_{ba} & 0 & \omega_{bc} \\ \omega_{ca} & \omega_{cb} & 0 \end{bmatrix}. \quad (2.44)$$

Ignoring the effects of travel for the moment, the evolution of the disease in each vertex is governed by the same system of equations as in Eqs. (2.28). For

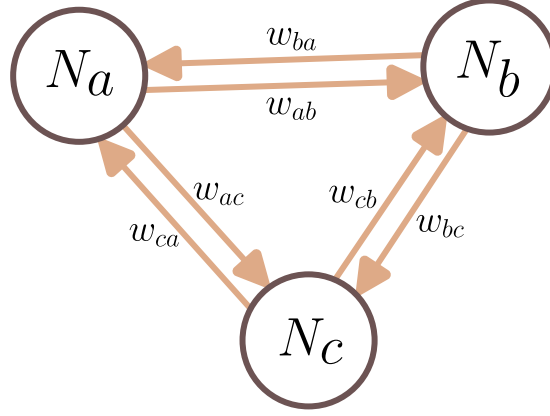


Figure 2.11: A simple example of the quantities associated with a graph representing a travel network. There are 3 vertices a, b and c . The populations associated with these nodes are denoted by n_a, n_b and n_c respectively. The rate of travel of individuals between vertices are denoted by w_{ab} for the number travelling, on average, from a to b etc.

each vertex i , the number of individuals on average belonging to each of the three S , I and R compartments at time t are denoted by $S_i(t)$, $I_i(t)$ and $R_i(t)$ respectively and are given as follows,

$$\frac{dS_i}{dt} = -\beta S_i I_i, \quad (2.45a)$$

$$\frac{dI_i}{dt} = \beta S_i I_i - \mu I_i, \quad (2.45b)$$

$$\frac{dR_i}{dt} = \mu I_i, \quad (2.45c)$$

where the population at any given time is determined by,

$$N_i = S_i + I_i + R_i. \quad (2.45d)$$

Here, β is interpreted as the rate of contact between susceptible and infectious individuals multiplied by the probability of infection on contact and μ is the rate of recovery. For travelling individuals, it is assumed that it does not matter what compartment they belong to, the rate of movement, ω_{ij} , is the same for all compartments. This assumption in general is not necessary. For example, a quarantining compartment could be added which would have little to no movement between vertices. Thus, the rate of change of the number of susceptible individuals in a vertex at time t , is given by the quantity $\sum_{j \in V} (\omega_{ji} S_j(t) - \omega_{ij} S_i(t))$,

similarly for the other compartments. With this quantity, we write the evolution of a vertex i , in the meta-population SIR model as,

$$\frac{dS_i}{dt} = -\beta S_i I_i + \sum_{j \in V} (\omega_{ji} S_j - \omega_{ij} S_i), \quad (2.46a)$$

$$\frac{dI_i}{dt} = \beta S_i I_i - \mu I_i + \sum_{j \in V} (\omega_{ji} I_j - \omega_{ij} I_i), \quad (2.46b)$$

$$\frac{dR_i}{dt} = \mu I_i + \sum_{j \in V} (\omega_{ji} R_j - \omega_{ij} R_i), \quad (2.46c)$$

An interesting result of these set of equations are their relationship to the reaction diffusion equations, specifically the Fisher-Kolmogorov–Petrovsky–Piskunov (FKPP) equation [29, 42] which is defined as,

$$\frac{\partial u}{\partial t} = D \frac{\partial^2 u}{\partial x^2} + mqu, \quad (2.47)$$

where $u(x, t)$ is some function in x and t , and D , m , and q are constant parameters. The formulation of the above equation is of the same form used in the original paper by Fisher in Ref. [65]. Given the vertices are arranged in a line such that vertex i is in position i , and the travel rates are given by $\omega_{ij} = \omega \delta_{i-1,j} + \omega \delta_{i+1,j}$ where δ_{ij} is the Kronecker delta, i.e., travel is only allowed between neighbours. Then, the set of equations given by Eqs. (2.46), relate directly to the FKPP equation. It can be shown in this case that with sufficiently localised initial conditions, the system exhibits a travelling wave speed in the proportion of infected individuals of approximately $\sqrt{\omega}$ as shown in Ref. [42]. As such, the meta-population models may be thought of a generalised (in the sense that the wave front travels along a graph rather than spatially) and discretised reaction diffusion equation.

Often populations of large geographical areas are already in a diffusive equilibrium and populations remain constant, at least compared to the timescales of the model. Thus, it is sometimes required that the population of vertices in the meta-population model remain constant over time. Given the travel rates of the model, the population of each vertex in diffusive equilibrium is determined by

the balance $N_i(\infty)/N_j(\infty) = \omega_{ji}/\omega_{ij}$. Thus, with constant travel rates, the only way to ensure a constant population within each vertex is to choose the travel rates such that $\omega_{ij} = \omega_{ji}$, making the graph undirected, and thus, the adjacency matrix \mathbf{W} , symmetric. When allowing for temporal travel rates, there are more realistic options available for necessitating a constant population. For example, in the case of commuting, these travel rates may be periodic functions. More will be discussed on this in Chp. 4.

Epidemic threshold

As with the previous epidemiological models, the concept of epidemic threshold is just as important, i.e., what combination of parameters gives rise to an epidemic. The fact individuals can move between vertices complicates things slightly. The overall level of infectious individuals may be rising, however, in particular vertices the level may be lowering due to a high rate of travel out. As a result, we must be careful with how we define an epidemic in the meta-population SIR model. This is most easily done by establishing the basic reproduction number, \mathcal{R}_0 , at the basic DFE. Thus, we define an epidemic in the meta-population SIR model as any condition that produces $\mathcal{R}_0 > 1$ at the basic DFE. This set of parameters which produce $\mathcal{R}_0 = 1$ we call the epidemic threshold.

In order to compute the reproduction number, and thus epidemic threshold, we follow [54] and compute the next generation matrix of the system. Firstly, only the *infection subsystem* is considered, which is all equations that describe the production of new infected individuals as well as changes in the state of already infected individuals. Linearising the infection subsystem of equations near the basic DFE, which is defined as $[\mathbf{S}^T, \mathbf{I}^T, \mathbf{R}^T]^T = [\mathbf{M}^T, \mathbf{0}^T, \mathbf{0}^T]^T$, gives,

$$\frac{dI_i}{dt} = \beta N_i I_i + \sum_{j \in V} (\omega_{ji} I_j - \omega_{ij} I_i), \quad (2.48)$$

where $\mathbf{N} = [N_1, \dots, N_{n_v}]^T$, $\mathbf{S} = [S_1, \dots, S_{n_v}]^T$ and similarly for \mathbf{I} and \mathbf{R} . We shall refer to the infected compartment in vertex i as *infected state i* . Now the goal is

to write the system above as,

$$\frac{d\mathbf{I}}{dt} = (\mathbf{T} + \mathbf{\Sigma})\mathbf{I}, \quad (2.49)$$

where \mathbf{T} and $\mathbf{\Sigma}$ are both matrices. T_{ij} describes the rate at which infected individuals in infected state i give rise to infected individuals in infected state j and Σ_{ij} describes the rate at which individuals move from infected state i to infected state j except on the diagonal, which describes the rate at which infected individuals leave/enter the infected state i not via another infected state. This produces the matrices,

$$T_{ij} = \beta N_i \delta_{ij}, \quad (2.50)$$

$$\Sigma_{ij} = -\mu \delta_{ij} + \omega_{ji} - \delta_{ij} \sum_{k \in V} \omega_{ik}, \quad (2.51)$$

Writing these equations using their full matrix specification gives,

$$\mathbf{T} = \text{diag}(\beta \mathbf{N}) \quad (2.52)$$

$$\mathbf{\Sigma} = \mathbf{W}^T - \text{diag}((\mu \mathbf{Id} + \mathbf{W}) \mathbf{1}). \quad (2.53)$$

As shown in Ref. [54], the basic reproduction number of the system is determined by,

$$\mathcal{R}_0 = \rho(\mathbf{T}\mathbf{\Sigma}^{-1}) = \rho\left(\text{diag}(\beta \mathbf{N}) (\mathbf{W}^T - \text{diag}((\mu \mathbf{Id} + \mathbf{W}) \mathbf{1}))^{-1}\right) \quad (2.54)$$

where ρ denotes the spectral radius operator, that is, the largest magnitude of all eigenvalues of the matrix. If the travel rates are assumed to be zero, we get the basic reproduction number to be,

$$\mathcal{R}_0 = \rho(\text{diag}(\beta \mathbf{N}) (\mu \mathbf{Id})^{-1}) = \frac{\beta \max_i(N_i)}{\mu}, \quad (2.55)$$

which is exactly the condition found in the well mixed SIR model (see Eqs. (2.34)). However, in this case, the maximum of all populations $\max_i N_i$ is used in the reproduction number.

The network models for the spread of disease which we have looked at are what are referred to as data-driven models [199], in that they require an adjacency matrix, usually informed by empirical data, in order to run them. While these models are very useful, it is often the case there is no network data available on the system we wish to model, especially in less developed countries where data collection is not a priority. In such cases we may turn to mobility models, which are able to generate likely movements of individuals and thus, let us build contact networks.

2.4 Network Mobility Models

An important aspect of developing good network models for contagion dynamics on large scales, is one's ability to accurately model the movement of individuals [19] between vertices in the context of meta-population models or model interactions between individuals in the context of contact network models. Much of the time empirical movement data is used [41, 168]. This has both its uses and drawbacks. While it offers a good representation of the mobility or contacts within/between groups, there are often biases which depend on how and when the data was collected. Take the 2016 census in Ireland [36] for example. The census asked where individuals had travelled on the day. This provides snapshot into the behaviour of individuals movement patterns at a particular moment in time. However, the static nature of such data presents challenges, as there is no clear way in how to use the data in other contexts. For example, if the data was collected on a Sunday, is it a good approximation for Monday, or in the case of restricted movement as seen during the COVID-19 pandemic, how does one use the data to inform movements when usual patterns would change. These kind of questions have no clear answers. As a result, many researchers turn to either the gravity [152, 175] or radiation [129, 134, 174] models which may easily adapt and respond to changes in movement behaviours as well as external factors.

Mobility in complex systems is a very difficult thing to model as it involves many complicated interactions and quantities within the system that are often

too numerous and difficult to measure. The goal of the mobility models we will look at is to attempt to take advantage of universal properties of mobility that appear in empirical data [134], leading to very simple descriptions. As a result, likelihood of mobility between locations in some system may be described using just population size and distance. In the case of the radiation model, it does not even need parameters fit in the most simple case.

2.4.1 Gravity Model

The gravity model is based on the simple assumption that the likelihood of an individual travelling from one location to another is directly proportional to the product of the locations' populations, divided by some function of the distance between them. This model has seen wide use in literature with its first appearance dating back to 1859 [35]. While often used for human mobility, it also sees extensive use in regression analysis for predicting international trade [155].

Given a number of locations in a geographical area labeled $1, \dots, n_v$, where location i has population N_i and the distance between two locations i and j is denoted by d_{ij} , then expected number of travellers per unit time, T_{ij} , from location i to j is given by,

$$T_{ij} = N_i^\alpha N_j^\beta f(d_{ij}). \quad (2.56)$$

The name *gravity model* becomes apparent due to the formulation being related to Newton's law of gravity. In the above equation, the parameters α and β are adjustable exponents which take into account specific properties of the area being modelled. These parameters are usually fit using a linear regression, and thus, the gravity model requires empirical data to fit against. As we will see in the next section this is not a necessity in the radiation model. A case against the gravity model as often used in research is its lack of a rigorous derivation from first principles. It does however result from entropy maximisation techniques as proven in [200]. Although, this derivation shows the values of α and β to be 1 and gives no hint as to what the cost function as denoted by f in Eq. (2.56) is to be.

The deterrence function, f , is a sort of cost function that penalises locations for being further away. The most common forms of the function are the exponential function $f(d) = e^{-\gamma d}$ [33] and the power-law function $f(d) = d^{-\kappa}$ [134], both single parameter functions which must also be fit from empirical data. More complicated functions are possible such as a combination of power-law and exponential [128] or even the log-normal distribution [74].

In the case of very low or zero counts in the number of travellers between locations in the empirical data, the estimations provided by the above model when fit using linear regression can perform very poorly. It can significantly under or over predict the total number of travellers when compared to the actual data. There are a number of attempts to alleviate this problem [33] such as fitting using a poisson or modified poisson regression models. However, it is possible to obtain better results using what are referred to as *constrained* gravity models. These models ensure that certain quantities are matched in the prediction such as overall flow of individuals, total flow out of locations, total flow into locations or a combination. There are 4 constrained models in common use, the *total flow constrained* gravity model, the *production constrained* gravity model, the *attraction constrained* gravity model and the *doubly constrained* gravity model [89].

In the total flow constrained gravity model, the total number of travellers between locations is matched to some quantity. Thus, if there are m travellers overall, the model produces $\sum_{i,j} T_{ij} = m$, where T_{ij} are the expected travellers from i to j . Thus, the flow constrained gravity model is formulated as,

$$T_{ij} = \frac{m N_i^\alpha N_j^\beta f(d_{ij})}{\sum_{k,l} N_k^\alpha N_l^\beta f(d_{kl})}. \quad (2.57)$$

In the production constrained gravity model, the predicted total number of travellers out of a location matches a required amount. Thus, the model produces $\sum_j T_{ij} = u_i$, where u_i denotes the required total number of individuals travelling

out of location i . The production constrained gravity model is given by,

$$T_{ij} = \frac{u_i N_j^\beta f(d_{ij})}{\sum_k N_k^\beta f(d_{ik})}. \quad (2.58)$$

The attraction constrained gravity model's description is similar to the production constrained model in that they are both singly constrained. The attraction constrained model has the predicted total number of travellers into a location match a required amount. Thus, the model produces $\sum_i T_{ij} = v_j$ where v_i is the required total number of individuals travelling into location i . The attraction constrained gravity model is given as,

$$T_{ij} = \frac{v_j N_i^\alpha f(d_{ij})}{\sum_k N_k^\alpha f(d_{kj})}. \quad (2.59)$$

Finally, in the doubly constrained or production-attraction constrained gravity model, both the predicted total number of travellers out of location and the total number of travellers into a location match required amounts. Thus, the model produces $\sum_j T_{ij} = u_i$ and $\sum_i T_{ij} = v_j$ where u_i is the required total number of individuals travelling from location i and v_j is the required total number of individuals travelling into location j . The doubly constrained gravity model is given as,

$$T_{ij} = a_i b_j u_i v_j f(d_{ij}), \quad (2.60a)$$

$$a_i = \left(\sum_k b_k v_k f(d_{ik}) \right)^{-1}, \quad (2.60b)$$

$$b_i = \left(\sum_k a_k u_k f(d_{ki}) \right)^{-1}, \quad (2.60c)$$

where the equations a_i and b_i are normally solved by iterative means.

2.4.2 Radiation Model

The goal of the radiation model is much the same as the gravity model. It attempts to model the flow of individuals between various locations by attempting to take advantage of universal patterns that are often seen in mobility data. This allows for a short and concise description of the probability of an individual travelling from one location to another by approximating the likelihood using only a few explanatory variables. In the case of the *basic* gravity model [174], there are no parameters which require fitting. This provides a huge advantage in comparison to the gravity model which requires a substantial amount of data in order to be able to fit its numerous parameters. It also means that the radiation model may be used when there is no empirical data available to fit against.

The radiation model is still relatively young, with it first being introduced in 2012 [174], this is in stark contrast to the gravity model which has been discussed in some form or another for well over a century [35]. This may be due to the formulation of the radiation model not being as obvious as the gravity model, however, they can be shown to be equivalent with certain distributions of populations [94].

A key difference between the two mentioned models is that the gravity model only depends on the properties, usually just population, of the home and destination locations. This not the most realistic assumption as for locations that are far apart, the probability of travelling from one to another is likely affected by the number of locations in between as well as their own attractiveness. Simply put, an individual is less likely to travel to a destination location when there are numerous locations with a very high attractiveness between the source location and the destination location. Fortunately, the radiation model makes this exact assumption.

In order to derive the radiation model, the probability of a travel between two locations is modelled as an emission/absorption process of particles, hence the name *radiation model*. Suppose there are n_v locations labeled $1, \dots, n_v$ such that location i has a population of N_i . The distance between two locations i and j

is denoted by d_{ij} . Given some probability distribution $p(z)$ which represents the distribution of the attractiveness of a benefit in a location. We define a benefit as anything which would attract an individual to a location, for example, number of jobs. Then, each location has n_i random variables z_i (which represent benefits and their attractiveness) drawn from $p(z)$ associated with it. Given that an individual is travelling from location i , it is assumed they will choose the closest location which has a benefit higher than in their own location. Mathematically, this can be written,

$$\begin{aligned} q_{ij} &= \int_0^\infty p_{n_i}(z) p_{s_{ij}}(< z) p_{m_j}(> z) dz, \\ &= \frac{N_i N_j}{(N_i + s_{ij})(N_i + N_j + s_{ij})}. \end{aligned} \quad (2.61)$$

That is, q_{ij} is the probability of a single traveller leaving from location i choosing location j . The quantity denoted by $p_x(z)$, is the probability that the maximum value attained after x extractions from the random distribution $p(z)$ is z . Similarly, $p_x(< z)$ and $p_x(> z)$ are the probabilities that the maximum value attained after x extractions from the random distribution $p(z)$ is less than or greater than z respectively. The variable denoted s_{ij} , is the sum of all populations within a circle centered at i with a radius of d_{ij} not including the populations of i and j themselves.

$$s_{ij} = \sum_{\substack{k; d_{ik} < d_{ij} \\ k \neq i \neq j}} N_k. \quad (2.62)$$

Let u_i denote the total number of individuals leaving location i , as in gravity model. Then, the probability that exactly x travellers leaving from i arrive at j is given by the binomial distribution,

$$P_{ij}(x) = \frac{u_i!}{x!(u_i - x)!} q_{ij}^x (1 - q_{ij})^{u_i - x}, \quad (2.63)$$

and thus, the expected number of travellers, T_{ij} , from i to j is given as,

$$\begin{aligned} T_{ij} &= u_i q_{ij} \\ &= u_i \frac{N_i N_j}{(N_i + s_{ij})(N_j + s_{ij})}. \end{aligned} \tag{2.64}$$

This can be directly compared to the production constrained gravity model which predicts the exact same quantity with the same constraint.

2.5 Summary

In this chapter we have introduced the basics required for the rest of the chapters. We start with defining networks and their graph representations along with definitions and measures pertaining to them. We then introduce the SIR model for well mixed populations which is the starting point for much epidemiological modelling. In this model we derive the condition necessary for an epidemic to occur and how it relates to the basic reproduction number, \mathcal{R}_0 .

After developing the theory for the SIR model in the well mixed case, we show how the model can be extended to the network case by two means, the IB model, which we develop further in Chp. 3, and the meta-population model, which is used in Chp. 4. The IB model assumes that each vertex in the graph represents a single individual, whereas the meta-population model assumes each vertex is a small community on which the original well mixed epidemiological models can be used. For both of these cases we also compute the basic reproduction number and thus, the condition required for an epidemic to occur.

Following the discussion of epidemics on networks, we introduce two models for mobility which can be used to build networks in the absence of empirical data. These are the gravity and radiation models. Both work by assuming that the attractiveness between two vertices is proportional to some function of their populations and distance between them. We will use the radiation model in Chp. 4 in order to build commuting patterns under various movement restriction

scenarios. In Chp. 5 will extend and generalise the radiation model in order to describe the distribution of cattle trades in Ireland and compare its performance to the gravity model.

Chapter 3

A Systematic Framework For the Modelling of Epidemics on Temporal Networks

In this chapter we present a modelling framework for the spreading of epidemics on temporal networks from which both the Individual-Based (IB) and Pair-Based (PB) models can be recovered. We have previously discussed the formulation of the IB model in Sec. 2.3, which approximates the spread of disease on a network by assuming statistical independence in the state of the vertices. The proposed temporal PB model that is systematically derived from this framework offers an improvement over existing PB models and moves away from edge-centric descriptions as in the contact-based model [117] while keeping the description concise and relatively simple. For the contagion process, we consider a Susceptible-Infected-Recovered (SIR) model, which is realized on a network with time-varying edges (specifically a discrete-time temporal graph which we define in Sec. 2.1.1). We show that the shift in perspective from IB to PB quantities enables exact modelling of Markovian epidemic processes on temporal networks which have no more than one non-backtracking path between any two vertices. On arbitrary networks, the proposed PB model provides a substantial increase in accuracy at a low com-

putational and conceptual cost compared to the IB model. From the PB model, we analytically find the condition necessary for an epidemic to occur, otherwise known as the epidemic threshold. We identify an epidemic by looking at the stability the Basic Disease-Free Equilibrium (basic DFE), that is, the state of the system before any infected individuals are present.

3.1 Overview

In recent years epidemiological modelling, along with many other fields, has seen renewed activity thanks to the emergence of network science [18, 135, 145, 203]. Approaching these models from the view of complex coupled systems has shed new light onto spreading processes where the early black-box Ordinary Differential Equation (ODE) models, such as those developed by Kermack and McKendrick, had their limitations [99, 110]. These ODE models assume homogeneous mixing of the entire population, which may be an appropriate approximation for small communities. However, when attempting to model the spread of disease at a national or international level, they fail to capture how heterogeneities in both travel patterns and population distributions contribute to and affect the spread of disease. Epidemiological models on complex networks aim to solve this problem by moving away from averaged dynamics of populations and mean-field descriptions. Instead, the focus is on interactions between individuals or meta-populations, where the spreading process is driven by contacts in the network [42, 169, 194].

There have been many improvements made in regards to network models, e.g., generalised multi-layer network structures or more specifically temporal networks that allow for the network structure to change with time [100, 116, 123, 135]. Temporal networks are a natural way of representing contacts and lead to an insightful interplay between the disease dynamics and the evolving network topology [106, 122, 173]. With the ever growing availability of mobility and contact data it has become easier to provide accurate and high-resolution data to inform network models. The results can be extremely useful tools for

public-health bodies and other stakeholders [75, 76, 187].

In previous works, a widely used epidemiological concept is the IB model [145, 171, 189], (see Sec. 2.3). It assumes statistical independence in the state of each vertex. A major problem associated with such a model is that it suffers quite badly from an echo chamber effect due to the fact that there is no memory of past interactions due to statistical independence.

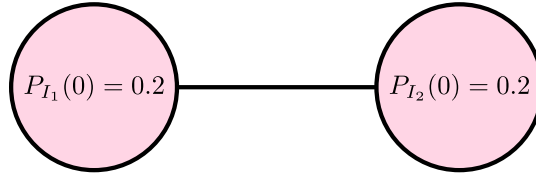


Figure 3.1: A 2-vertex graph with both vertices connected by an edge for all time. The quantities $P_{I_1}(0) = 0.2$ and $P_{I_2}(0) = 0.2$ refer to the initial conditions of the SIR model shown in Fig. 3.2.

In order to demonstrate this phenomenon of echo chambers, we consider a graph as in Fig. 3.1, made up of 2 vertices which are connected for all time, i.e., a temporal realisation of a static graph. We give the two vertices initial conditions such that their initial probability of being infected is 0.2, i.e. $P_{I_1}(0) = P_{I_2}(0) = 0.2$ using the notation introduced in Sec. 2.3 for the IB model. Then, by running the IB model and comparing the results to the average of many Monte-Carlo (MC) realisations of the stochastic SIR infection process that the IB model attempts to describe, we can judge the accuracy of the IB model by how close to the average of the MC realisation it is.

In Fig. 3.2, we show the results of running the IB model (red curve) as well as the average of 10^4 MC realisations (green curve) for 40 time steps. The parameters used were $\beta = 0.4$ and $\mu = 0.2$. The y-axis shows the average proportion of the number of recovered which $P_{R_{\text{avg}}} = \frac{1}{2}(P_{R_1}(t) + P_{R_2}(t))$. From this very simple example, it is clear how the IB model fails in describing the true process by vastly overestimating the probability of contracting the disease at some point during the evolution of the model.

There have been efforts to ameliorate this problem by introducing memory at the level of each vertex's direct neighbours. These models referred to as Contact-

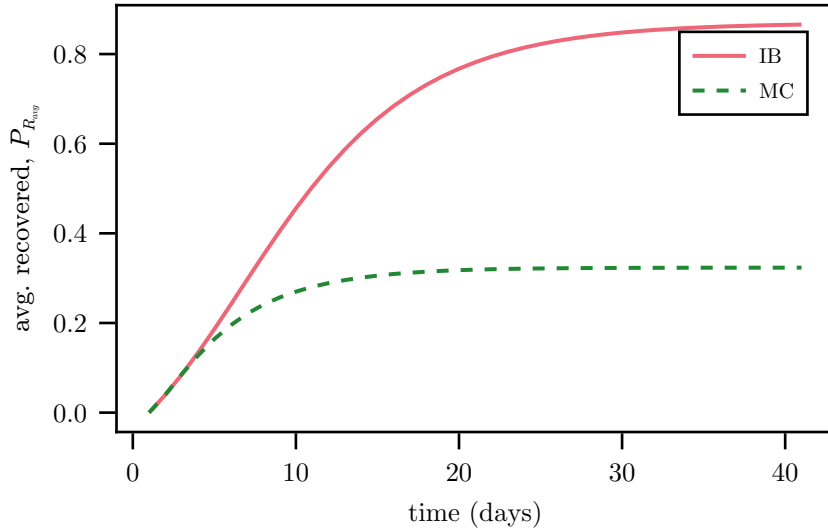


Figure 3.2: The average number of recovered individuals in the SIR model according to the IB model (red curve) and the average of 10^4 MC realisations (green dashed curve). The parameters used were $P_{I_1}(0) = P_{I_2}(0) = 0.2$, $\beta = 0.4$ and $\mu = 0.2$.

Based [117] or PB [68] and have been shown to significantly reduce the echo chamber effect, depending on the underlying network structure. These two models differ in their initial approach. The contact-based model takes an edge-based perspective, which extends the message-passing approach [106, 114], and all dynamic equations are formulated in terms of edges. By contrast, the PB model keeps the vertex-based approach of the IB model and dynamic equations are in terms of vertices.

This chapter is largely based on our work in Ref. [98], in which we extend the PB model to a temporal setting giving a Temporal Pair-Based (TPB) Model. We show how it can be drastically reduced and simplified under a certain dynamical assumption [172]. We deal specifically with SIR models. Once the TPB model is written in concise form, it is then possible to show that the contact-based model is equivalent to a linearised version of the TPB model. We then establish the conditions for an epidemic to occur according to the TPB model, also known as the epidemic threshold. We investigate how the TPB model performs on a number of synthetic and empirical networks and investigate what kind of network

topologies work best with the TPB model.

3.2 Reduced Master Equations

Let us start by considering a discrete time temporal network, $\mathcal{G} = (G_1, \dots, G_{n_t})$ (as in Sec. 2.1.1), to be a series of n_t networks where $G_t = (V, E_t)$ denotes the network at time step t . The networks all share the same vertex set, V , but differ in their temporal edge sets, E_t . Let $n_v = |V|$ be the number of vertices and $n_{e,t} = |E_t|$ be the number of edges at time t . The adjacency matrix for the network at time t will be denoted by $\mathcal{A}^{[t]}$, and $\mathcal{A}_{ij}^{[t]} = 1$ implies a directed edge between vertices i and j at time t . If the network is undirected then we have $\mathcal{A}_{ij}^{[t]} = \mathcal{A}_{ji}^{[t]}$.

Let Ω be the set of compartments in an epidemiological compartment model, that is, in the SIR model: $\Omega = \{S, I, R\}$. Let $\mathbf{x}_t = [x_1, x_2, \dots, x_{n_v}]^T \in \Omega^{n_v}$ be the vector whose i -th element refers to the state of the i -th vertex, i.e., $x_i = S$ means vertex i $\mathcal{A}_{ij}^{[t]} = \mathcal{A}_{ji}^{[t]}$ belongs to compartment S , similarly for other compartments. The evolution of the disease is then described by the discrete-time and space master equation [73],

$$\Delta P(\mathbf{x}, t) = \sum_{\mathbf{y} \in \Omega^{n_v}} [W(\mathbf{x}|\mathbf{y}, t)P(\mathbf{y}, t) - W(\mathbf{y}|\mathbf{x}, t)P(\mathbf{x}, t)], \quad (3.1)$$

and thus, we assume that the infection process is Markovian. $P(\mathbf{x}, t)$ is the probability of the network being in the particular configuration of states given by \mathbf{x} at time t and $W(\mathbf{x}|\mathbf{y}, t)$ is the transition rate of the network moving from the configuration of states \mathbf{y} to \mathbf{x} at time t . These equations describe the entire process on the network. However, in order to progress the system forward one step in time, the probabilities of all combinations of state vectors must be found. This usually is not feasible for network processes with potentially billions of vertices as for the SIR process the total combination of states is given by 3^{n_v} .

As an alternate approach, it is possible to describe the evolution of the disease

using a system of Reduced Master Equations (RMEs) [171], that describes the evolution of subsystems within the network, such as individual vertices, removing the need to obtain every possible combination of states. An important note is that these RMEs are in fact not themselves true master equations as they are not necessarily linear due to the fact that the transition rates of the subsystems are nonlinear combinations of the transitions rates of the original system. However, we shall continue to use the term RME introduced by the author of Ref. [171]. We use the following notation for the joint marginal probabilities,

$$P_{x_{i_1}, x_{i_2}, \dots, x_{i_k}}(t), \quad (3.2)$$

which is the probability of realising the states $x_{i_1}, x_{i_2}, \dots, x_{i_k}$ for the vertices i_1, i_2, \dots, i_k at time t respectively. For denoting the condition marginal probabilities we use the similar notation,

$$P_{x_{i_1}, x_{i_2}, \dots, x_{i_k} | x_{j_1}, x_{j_2}, \dots, x_{j_l}}(t), \quad (3.3)$$

for the probability of the vertices i_1, i_2, \dots, i_k being in the states $x_{i_1}, x_{i_2}, \dots, x_{i_k}$, respectively, at time t , given that the vertices j_1, j_2, \dots, j_l are in the states $x_{j_1}, x_{j_2}, \dots, x_{j_l}$ respectively, at time t also. We use the following notation for the marginal transition rates,

$$W_{x_{i_1}, x_{i_2}, \dots, x_{i_k} | y_{i_1}, y_{i_2}, \dots, y_{i_k}}(t), \quad (3.4)$$

which is the transition rate of vertices i_1, i_2, \dots, i_k respectively moving to the states $x_{i_1}, x_{i_2}, \dots, x_{i_k}$ at time t , given they are in the states $y_{i_1}, y_{i_2}, \dots, y_{i_k}$.

When we wish to specify a particular realisation of x_i , we denote it by S_i , I_i or R_i to imply $x_i = S$, $x_i = I$ or $x_i = R$ respectively. Employing this new notation we start with the RME, which describes the evolution of individual vertices,

$$\Delta P_{x_i}(t) = \sum_{y_i \in \Omega} [W_{x_i | y_i}(t) P_{y_i}(t) - W_{y_i | x_i}(t) P_{x_i}(t)], \quad (3.5)$$

The next section deals with how to approximate the quantities given above in

the RME.

3.3 SIR Network Model

For SIR dynamics, the evolution of each vertex in each compartment is given as the following,

$$P_{S_i}(t_{n+1}) = P_{S_i}(t_n) + \Delta P_{S_i}(t_n), \quad (3.6a)$$

$$P_{I_i}(t_{n+1}) = P_{I_i}(t_n) + \Delta P_{I_i}(t_n), \quad (3.6b)$$

$$P_{R_i}(t_{n+1}) = P_{R_i}(t_n) + \Delta P_{R_i}(t_n), \quad (3.6c)$$

where $\Delta P_{S_i}(t_n)$ is defined by the RME in the previous section as Eq. (3.5). Filling in the transition rates we find,

$$P_{S_i}(t_{n+1}) = P_{S_i}(t_n) - W_{I_i|S_i}(t_n)P_{S_i}(t_n), \quad (3.7a)$$

$$P_{I_i}(t_{n+1}) = P_{I_i}(t_n) - W_{R_i|I_i}(t_n)P_{I_i}(t_n) + W_{I_i|S_i}(t_n)P_{S_i}(t_n), \quad (3.7b)$$

$$P_{R_i}(t_{n+1}) = P_{R_i}(t_n) + W_{R_i|I_i}(t_n)P_{I_i}(t_n). \quad (3.7c)$$

Note that transition rates such as $W_{R_i|S_i}$ are not present, as they are impossible and thus attain a value of 0. P_{R_i} can be recovered using the conservation of the probabilities $P_{S_i} + P_{I_i} + P_{R_i} = 1$. In order to compute the transition rates we define the following quantities: the probability of infection on contact, β , and the rate of recovery, μ . The quantity $\mathcal{A}^{[t_n]}$, is the temporal adjacency matrix of the network on which the process is occurring. Following directly from Ref. [68], the transition rates of moving from S to I , and I to R are given by,

$$\begin{aligned} W_{I_i|S_i}(t_n) = & \beta \sum_{j_1 \in V} \mathcal{A}_{ij_1}^{[t_n]} P_{I_{j_1}|S_i}(t_n) - \beta^2 \sum_{j_1 < j_2 \in V} \mathcal{A}_{ij_1}^{[t_n]} \mathcal{A}_{ij_2}^{[t_n]} P_{I_{j_1}, I_{j_2}|S_i}(t_n) \\ & + \dots - (-\beta)^{n_v-1} \sum_{j_1 < \dots < j_{n_v-1} \in V} \mathcal{A}_{ij_1}^{[t_n]} \dots \mathcal{A}_{ij_{n_v-1}}^{[t_n]} P_{I_{j_1}, \dots, I_{j_{n_v-1}}|S_i}(t_n), \end{aligned} \quad (3.8a)$$

$$W_{R_i|I_i}(t_n) = \mu. \quad (3.8b)$$

Equation (3.8a) can be thought of as analogous to the binomial distribution, where the probability of at least 1 success out of $n_v - 1$ trials is given as,

$$\begin{aligned} P(k > 0) &= 1 - \binom{n_v - 1}{0} \beta^0 (1 - \beta)^{n_v - 1} \\ &= \binom{n_v - 1}{0} \beta - \binom{n_v - 1}{1} \beta^2 + \binom{n_v - 1}{2} \beta^3 - \dots + \binom{n_v - 1}{n_v - 1} (-\beta)^{n_v - 1}, \end{aligned} \quad (3.9)$$

where β is the probability of success and k is the number of successes. The difference to Eq. (3.8a) however, is that the probability of success is different for each “infection attempt” as it depends on the current state of the system, as well as the state of the adjacency matrix. These equations describe the probabilistic SIR process on temporal networks. Note that the system of equations is not closed as they lack a description for their joint conditional probabilities $P_{I_{j_1}, S_i}$ as well as all higher order quantities. There are a number of ways in which this problem can be tackled, usually by making a number of numerical or dynamical approximations [79, 117, 189, 194].

In the next sections we attempt to improve on and unify many existing approaches showing how they are derived from the system of RMEs given by Eqs.(3.7) and (3.8).

3.3.1 Temporal Individual-based Model

One of the most commonly used epidemiological models on networks is the IB model, which has been extended to the temporal setting in Ref. [189]. We refer to this extension as the Temporal Individual-Based (TIB) model. The key idea is the assumption of statistical independence of vertices or the mean field approximation, i.e., the factorisation

$$P_{x_{i_1}, x_{i_2}, \dots, x_{i_k}}(t_n) = P_{x_{i_1}}(t_n) P_{x_{i_2}}(t_n) \dots P_{x_{i_k}}(t_n). \quad (3.10)$$

By assuming this independence of vertices, we solve the problem of Eq. (3.8a) not being closed with it simplifying to,

$$\begin{aligned}
W_{I_i|S_i}(t_n) = & \beta \sum_{j_1 \in V} \mathcal{A}_{ij_1}^{[t_n]} P_{I_{j_1}}(t_n) - \beta^2 \sum_{j_1, j_2 \in V} \mathcal{A}_{ij_1}^{[t_n]} \mathcal{A}_{ij_2}^{[t_n]} P_{I_{j_1}}(t_n) P_{I_{j_2}}(t_n) \\
& + \dots - (-\beta)^{n_v-1} \sum_{j_1 < \dots < j_{n_v-1} \in V} \mathcal{A}_{ij_1}^{[t_n]} \dots \mathcal{A}_{ij_{n_v-1}}^{[t_n]} P_{I_{j_1}}(t_n) \dots P_{I_{j_{n_v-1}}}(t_n).
\end{aligned} \tag{3.11}$$

Under the assumption of independence, the conditional probability is cancelled by the definition of conditional probability, i.e.,

$$P_{I_{j_1}|S_i} = \frac{P_{I_{j_1}, S_i}}{P_{S_i}} = \frac{P_{I_{j_1}} P_{S_i}}{P_{S_i}} = P_{I_{j_1}} \tag{3.12}$$

Upon factorising Eq. (3.11), it may be written more concisely as,

$$W_{I_i|S_i}(t_n) = 1 - \prod_{k \in V} \left(1 - \beta \mathcal{A}_{ik}^{[t_n]} P_{I_k}(t_n) \right). \tag{3.13}$$

Upon substituting the transition rates $W_{I_i|S_i}$ and $W_{R_i|I_i}$ under the assumption of statistical independence, the full TIB model is written as,

$$P_{S_i}(t_{n+1}) = P_{S_i}(t_n) \prod_{k \in V} \left(1 - \beta \mathcal{A}_{ik}^{[t_n]} P_{I_k}(t_n) \right) \tag{3.14a}$$

$$P_{I_i}(t_{n+1}) = P_{I_i}(t_n)(1 - \mu) + P_{S_i}(t_n) \left(1 - \prod_{k \in V} \left(1 - \beta \mathcal{A}_{ik}^{[t_n]} P_{I_k}(t_n) \right) \right), \tag{3.14b}$$

which is the same as the IB model given in Sec. 2.3, only discretised and extended to temporal graphs. The quantity which is multiplied by $P_{S_i}(t_n)$ is the probability of a vertex not becoming infected under the IB model. This model closes Eq. (3.8a) at the level of vertices, thus ignoring all correlations with other vertices at previous times. However, ignoring all past correlations causes the model to suffer quite badly from an echo chamber effect [173] (see Sec. 3.1). This echo chamber has the effect of vertices artificially amplifying each others probability of being infected, P_{I_i} , at each new time step, as the marginal probability of each vertex is highly correlated with the rest of the network and the factorisation of

Eq. (3.8a) means each vertex forgets its past interactions. As demonstrated in Ref. [173], in the absence of a recovered compartment, a static network of two linked vertices for non-zero initial conditions has probabilities of being infected which converge according to $\lim_{n \rightarrow \infty} P_{I_0}(t_n) = \lim_{n \rightarrow \infty} P_{I_1}(t_n) = 1$ for the TIB model.

Further simplifications of the TIB model are often seen [145, 171] by taking numerical approximations of the product in Eqs. (3.14). Given a sequence of numbers $(r_i)_{i=1}^N$ such that $|r_i| < 1$ for all i , one obtains,

$$\begin{aligned} \prod_{i=1}^N (1 - r_i) &= 1 - \sum_{i=1}^N r_i + \sum_{i=1}^N \sum_{j=1}^N r_i r_j - \sum_{i=1}^N \sum_{j=1}^N \sum_{k=1}^N r_i r_j r_k + \dots \\ &\approx 1 - \sum_{i=1}^N r_i. \end{aligned} \quad (3.15)$$

Using this numerical approximation, Eqs. (3.14) become

$$P_{S_i}(t_{n+1}) = P_{S_i}(t_n) \left(1 - \sum_{k \in V} \beta \mathcal{A}_{ik}^{[t_n]} P_{I_k}(t_n) \right) \quad (3.16)$$

$$P_{I_i}(t_{n+1}) = P_{I_i}(t_n)(1 - \mu) + P_{S_i}(t_n) \sum_{k \in V} \beta \mathcal{A}_{ik}^{[t_n]} P_{I_k}(t_n). \quad (3.17)$$

The TIB model which we have just derived is one of the simplest network models for the spread of disease one can use. The form of the model comes down to the choice of the level of statistical independence which is assumed for the vertices in order to close Eq. (3.8a). Hence, in the next section we see how an alternative assumption in the independence of vertices leads to a more accurate model.

3.3.2 Temporal Pair-based Model

In contrast to the TIB model, instead of assuming independence of vertices we can approximate the marginal probabilities in terms of combinations of lower order marginals using some form of moment closure [68, 172]. Here, we make an equivalent assumption to that of the message passing approaches [106, 173]. The assumption we make is that the graph contains no more than a single time-respecting Non-Backtracking (NBT) path (see Sec. 2.1.3) from one vertex to another (the path may be taken multiple ways through time, but the vertex sequence must be the same). If the graph is undirected, then this implies the graph contains no time-respecting NBT cycles. In other words, starting at some initial vertex i that leaves via vertex j , there is no way to find a time-respecting path returning to this vertex that does not return via j . This must mean that under the assumption of this model, an undirected graph must be a tree-graph in the static case, or in the case of a temporal graph, tree-like when it is viewed in its static embedding of the supra-adjacency representation [25].

These assumptions allow us to write all higher order moments in Eq. (3.8a) as a combination of pairs P_{S_i, I_k} . To show why this is possible, consider the three vertices i, j, k connected by two edges through i . If conditional independence of these vertices is assumed given we have the state of i , then one can make the following assumption,

$$P_{x_i, x_j, x_k} = P_{x_j, x_k | x_i} P_{x_i} = \frac{P_{x_i, x_j}}{P_{x_i}} \frac{P_{x_i, x_k}}{P_{x_i}} P_{x_i} = \frac{P_{x_i, x_j} P_{x_i, x_k}}{P_{x_i}}. \quad (3.18)$$

This has the effect of assuming that there exists only a single time-respecting NBT path from one vertex to another, as it implies that the flow of probability from j to k must occur through vertex i and does not occur through any other intermediary vertex. In the Sec. 3.5, we will investigate how this assumption holds up on graphs which do not satisfy the previously mentioned condition. The result obtained in Eq. (3.18) is often referred to as the Kirkwood closure [114]. Under the above assumption of conditional independence, the following simplification is

obtained for Eq. (3.8a),

$$W_{I_i|S_i}(t_{n+1}) = 1 - \prod_{k \in V} \left(1 - \beta \mathcal{A}_{ik}^{[t_n]} \frac{P_{S_i, I_k}(t_n)}{P_{S_i}(t_n)} \right). \quad (3.19)$$

However, we run into the problem that we have no description for pairs of vertices. Thus, we derive expressions for their evolution from the RMEs for pairs of vertices which is given by,

$$\Delta P_{x_i, x_j}(t) = \sum_{y_i, y_j \in \Omega} [W_{x_i, x_j | y_i, y_j}(t) P_{y_i, y_j}(t) - W_{y_i, y_j | x_i, x_j}(t) P_{x_i, x_j}(t)], \quad (3.20)$$

For P_{S_i, I_j} , we obtain

$$\begin{aligned} P_{S_i, I_j}(t_{n+1}) &= P_{S_i, I_j}(t_n) + \Delta P_{S_i, I_j}(t_n) \\ &= P_{S_i, I_j}(t_n) + W_{S_i, I_j | S_i, S_j}(t_n) P_{S_i, S_j}(t_n) - W_{I_i, I_j | S_i, I_j}(t_n) P_{S_i, I_j}(t_n) \\ &\quad - W_{S_i, R_j | S_i, I_j}(t_n) P_{S_i, I_j}(t_n) - W_{I_i, R_j | S_i, I_j}(t_n) P_{S_i, I_j}(t_n). \end{aligned} \quad (3.21)$$

Note that the above equation requires a description for P_{S_i, S_j} also, which we find to be the following,

$$\begin{aligned} P_{S_i, S_j}(t_{n+1}) &= P_{S_i, S_j}(t_n) + \Delta P_{S_i, S_j}(t_n) \\ &= P_{S_i, S_j}(t_n) - W_{S_i, I_j | S_i, S_j}(t_n) P_{S_i, S_j}(t_n) \\ &\quad - W_{I_i, S_j | S_i, S_j}(t_n) P_{S_i, S_j}(t_n) - W_{I_i, I_j | S_i, S_j}(t_n) P_{S_i, S_j}(t_n). \end{aligned} \quad (3.22)$$

Since only the probabilities P_{S_i, I_j} and P_{S_i, S_j} are needed in order to describe the RMEs in Eq. (3.19), we consider those two combinations of states. From Ref. [68], we obtain the exact transition rates for pairs of vertices and find that we can factorise the pair-wise transition rates similar to Eq. (3.8a). Here, we give the expression for $P_{S_i, I_j | S_i, S_j}$ only, while the rest of the pair-wise transition rates

are given in Appendix A:

$$\begin{aligned}
W_{S_i, I_j | S_i, S_j}(t_n) = & \left[1 - \beta \sum_{k_1 \in V} \mathcal{A}_{ik_1}^{[t_n]} P_{I_{k_1} | S_i, S_j}(t_n) + \beta^2 \sum_{k_1 < k_2 \in V} \mathcal{A}_{ik_1}^{[t_n]} \mathcal{A}_{ik_2}^{[t_n]} P_{I_{k_1}, I_{k_2} | S_i, S_j}(t_n) \right. \\
& \left. - \dots + (-\beta)^{n_v-2} \sum_{k_1 < \dots < k_{n_v-2} \in V} \mathcal{A}_{ik_1}^{[t_n]} \dots \mathcal{A}_{ik_{n_v-2}}^{[t_n]} P_{I_{k_1}, \dots, I_{k_{n_v-2}} | S_i, S_j}(t_n) \right] \\
& \times \left[\beta \sum_{k_1 \in V} \mathcal{A}_{jk_1}^{[t_n]} P_{I_{k_1} | S_i, S_j}(t_n) - \beta^2 \sum_{k_1 < k_2 \in V} \mathcal{A}_{jk_1}^{[t_n]} \mathcal{A}_{jk_2}^{[t_n]} P_{I_{k_1}, I_{k_2} | S_i, S_j}(t_n) \right. \\
& \left. + \dots - (-\beta)^{n_v-2} \sum_{k_1 < \dots < k_{n_v-2} \in V} \mathcal{A}_{jk_1}^{[t_n]} \dots \mathcal{A}_{jk_{n_v-2}}^{[t_n]} P_{I_{k_1}, \dots, I_{k_{n_v-2}} | S_i, S_j}(t_n) \right]. \quad (3.23)
\end{aligned}$$

In the above equation, the term in the first pair of square brackets corresponds to the probability that vertex i does not become infected and the term in the second pair of square brackets corresponds to the probability that vertex j becomes infected. Upon applying our moment closure technique, Eq. (3.23) may be written as,

$$\begin{aligned}
W_{S_i, I_j | S_i, S_j}(t_n) = & \prod_{\substack{k \in V \\ k \neq j}} \left(1 - \beta \mathcal{A}_{ik}^{[t_n]} \frac{P_{S_i, I_k}(t_n)}{P_{S_i}(t_n)} \right) \left[1 - \prod_{\substack{k \in V \\ k \neq i}} \left(1 - \beta \mathcal{A}_{jk}^{[t_n]} \frac{P_{S_j, I_k}(t_n)}{P_{S_j}(t_n)} \right) \right]. \quad (3.24)
\end{aligned}$$

By introducing the following functions, the RMEs for pairs as well as the individual vertices can be written more concisely. The probability that vertex i does not become infected at time step t_{n+1} , given that i is not infected at time step t_n is denoted by

$$\Psi_i(t_n) = \prod_{k \in V} \left(1 - \beta \mathcal{A}_{ik}^{[t_n]} \frac{P_{S_i, I_k}(t_n)}{P_{S_i}(t_n)} \right). \quad (3.25)$$

Similarly, the probability that vertex i does not become infected at time step

t_{n+1} , given that i is not infected at time step t_n while excluding any interaction with j , is given by

$$\Phi_{ij}(t_n) = \prod_{\substack{k \in V \\ k \neq j}} \left(1 - \beta \mathcal{A}_{ik}^{[t_n]} \frac{P_{S_i, I_k}(t_n)}{P_{S_i}(t_n)} \right). \quad (3.26)$$

Then, the evolution of the state of every vertex in the network is determined by the following closed set of equations,

$$P_{S_i}(t_{n+1}) = \Psi_i(t_n) P_{S_i}(t_n) \quad (3.27a)$$

$$P_{I_i}(t_{n+1}) = (1 - \mu) P_{I_i}(t_n) + (1 - \Psi_i(t_n)) P_{S_i}(t_n) \quad (3.27b)$$

$$\begin{aligned} P_{S_i, I_j}(t_{n+1}) &= (1 - \mu) \left(1 - \beta \mathcal{A}_{ij}^{[t_n]} \right) \Phi_{ij}(t_n) P_{S_i, I_j}(t_n) \\ &\quad + \Phi_{ij}(t_n) (1 - \Phi_{ji}(t_n)) P_{S_i, S_j}(t_n) \end{aligned} \quad (3.27c)$$

$$P_{S_i, S_j}(t_{n+1}) = \Phi_{ij}(t_n) \Phi_{ji}(t_n) P_{S_i, S_j}(t_n). \quad (3.27d)$$

This approximation allows a large increase in accuracy compared to TIB model while only adding two equations to the final model. All past dynamic correlations are now tracked by the model and so the echo chamber effect is eliminated, but only with direct neighbours, that is, vertices which share an edge. A major benefit of this particular TPB model over other existing iterations [79, 117] is that this model can be implemented as an element-wise sparse matrix multiplication rather than having to iterate through all edges for every time step making it extremely computationally efficient and fast on even large networks. It also benefits from a low conceptual cost by not deviating from a vertex-based perspective, like the contact-based models, which move to the perspective of edges and thus define the model in terms of the line-graphs and non-backtracking matrices [117].

Similar to Ref. [173], we can compare TPB models to the TIB model using the two vertex example. In that illustrative configuration, we consider two vertices connected by an undirected static edge and give the two vertices some initial non-zero probability $P_{I_1}(0) = P_{I_2}(0) = z$ of being infected. We then run the

TIB and TPB models for some given parameters β and μ and compare it to the ground truth, which is the average of a number of MC realisations.

In Fig. 3.3, we show the two vertex example from Fig. 3.1 again, however, this time we also plot the TPB model. It is apparent how the TIB model fails to capture the true SIR process on the network due to the previously discussed echo chamber induced by assuming statistical independence of vertices. It becomes clear that the TPB model accurately describes the underlying SIR process for this simple example as each vertex is able to recover the dynamic correlations of past interactions with direct neighbours.

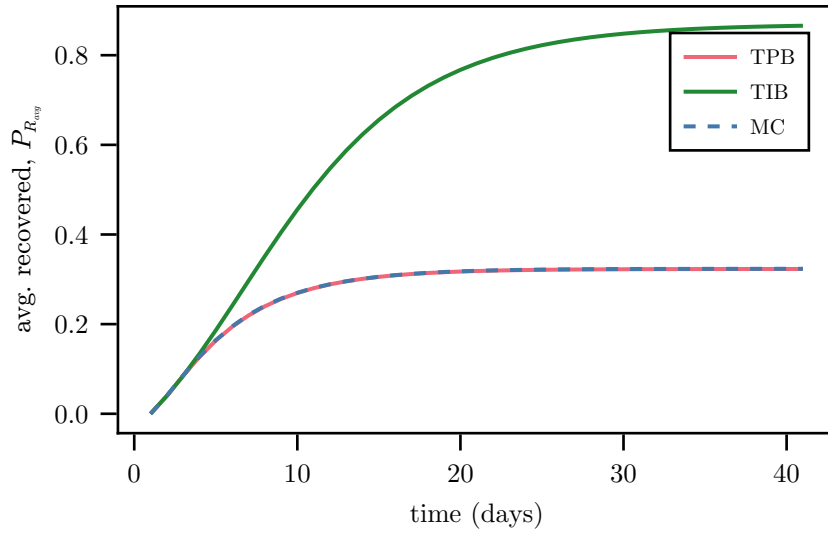


Figure 3.3: Running 40 time steps of the TIB (green curve) and TPB (red curve) SIR model as well as the average over 10^5 MC simulations (blue dashed curve) for the two vertex example given in Fig. 3.1. Parameters: $\beta = 0.4$, $\mu = 0.2$, and initial conditions $P_{I_1}(0) = P_{I_2}(0) = 0.2$.

Equivalence Between The Contact-based and Pair-based Models

The contact-based model as defined in Ref. [117], is an extension of the message passing approach to the spreading of epidemics. It moves from considering individual vertices to edges in the network, thus tracking pairs of vertices similar to our pair based model. The central component is $\theta_{ij}(t_n)$, which is the probability

that node j has not passed infection to node i up to time step n . From $\theta_{ij}(t_n)$, the quantity $P_{S_i}(t_n)$ may be computed as,

$$P_{S_i}(t_{n+1}) = P_{S_i}(t_0) \prod_{j \in V} \theta_{ij}(t_{n+1}). \quad (3.28)$$

This equation is the basis for the contact-based model and allows us to easily compare with the PB model as it describes the same quantity as our Eq. (3.27a). The authors also assume that the evolution of $\theta_{ij}(t_n)$ satisfies the following relation,

$$\begin{aligned} \theta_{ij}(t_{n+1}) &= \theta_{ij}(t_n) - \beta \mathcal{A}_{ij}^{[t_n]} \frac{P_{S_i, I_j}(t_n)}{P_{S_i}(t_n)} \\ \theta_{ij}(t_0) &= 1. \end{aligned} \quad (3.29)$$

In the PB model, the evolution of the susceptible probability, given by Eq. (3.27a), can similarly be rewritten in terms of its initial conditions,

$$P_{S_i}(t_{n+1}) = \Psi_i(t_n) P_{S_i}(t_n) \quad (3.30a)$$

$$= P_{S_i}(t_0) \prod_{m=0}^n \Psi_i(t_m) \quad (3.30b)$$

$$= P_{S_i}(t_0) \prod_{j \in V} \prod_{m=0}^n \left(1 - \beta \mathcal{A}_{ij}^{[t_m]} \frac{P_{S_i, I_j}(t_m)}{P_{S_i}(t_m)} \right). \quad (3.30c)$$

From equating (3.28) and (3.30) it is clear that if the models are exactly equivalent then θ_{ij} is defined by

$$\theta_{ij}(t_{n+1}) = \prod_{m=0}^n \left(1 - \beta \mathcal{A}_{ij}^{[t_m]} \frac{P_{S_i, I_j}(t_m)}{P_{S_i}(t_m)} \right). \quad (3.31)$$

However, this contradicts the assumption made by Eq. (3.29). Thus the PB and contact-based models are only equivalent if the following linearisation is as-

sumed:

$$\prod_{m=0}^n \left(1 - \beta \mathcal{A}_{ij}^{[t_m]} \frac{P_{S_i, I_j}(t_m)}{P_{S_i}(t_m)} \right) \approx 1 - \sum_{m=0}^n \beta \mathcal{A}_{ij}^{[t_m]} \frac{P_{S_i, I_j}(t_m)}{P_{S_i}(t_m)}, \quad (3.32)$$

which then implies Eq. (3.31) can be written as

$$\theta_{ij}(t_{n+1}) = 1 - \sum_{m=0}^{n-1} \beta \mathcal{A}_{ij}^{[t_m]} \frac{P_{S_i, I_j}(t_m)}{P_{S_i}(t_m)} - \beta \mathcal{A}_{ij}^{[t_n]} \frac{P_{S_i, I_j}(t_n)}{P_{S_i}(t_n)} \quad (3.33a)$$

$$= \theta_{ij}(t_n) - \beta \mathcal{A}_{ij}^{[t_n]} \frac{P_{S_i, I_j}(t_n)}{P_{S_i}(t_n)}. \quad (3.33b)$$

This shows that the contact-based model is a linearised version of the PB model.

We have shown that from our framework we are able to derive a number of existing models such as the TIB and contact-based models, and we derive a new concise form of the PB model in a temporal setting which also does not rely on any numerical linearisation. In the next section we compute the conditions necessary for an epidemic to occur in our TPB model.

3.4 Epidemic Threshold

One of the most important metrics used in epidemiological modelling is the epidemic threshold, which has been discussed in previous sections (cf. Sec. 2.3). It allows us to determine the critical values of the model parameters at which a transition in qualitative behaviour occurs and an epidemic occurs. In order to determine these parameters, we first need the fixed points of the system, as their stability can aid us in the definition of an epidemic. The fixed points are given as,

$$P_{S_i}(t_n) = S_i^*, \quad P_{I_i}(t_n) = 0, \quad P_{R_i}(t_n) = R_i^* \quad \forall i, \quad (3.34)$$

where $S_i^* + R_i^* = 1$. From this definition it is clear that there exists a whole class of Disease-Free Equilibriums (DFEs), which must be considered. At the critical point, defined by some function of the model parameters, the DFE becomes unstable and on average an epidemic occurs. Defining an epidemic in the SIR

model is a bit more difficult compared to the Susceptible-Infected-Susceptible (SIS) model due to the fact that the flow of probability is in only one direction between compartments $S \rightarrow I \rightarrow R$. Therefore, the class of DFE solutions are always asymptotically stable. Thus, we will look at classifying the initial stability of the SIR model as we perturb it from the state,

$$P_{S_i}(t_n) = S_i^*, \quad P_{I_i}(t_n) = 0, \quad P_{R_i}(t_n) = 0 \quad \forall i, \quad (3.35)$$

which we shall define as the basic DFE. If it is unstable that means the disease has a chance to take hold and will spread through the network causing an epidemic before dying out. We now look at small perturbations from the basic DFE, if they vanish then the disease will die out and will not have a chance to propagate through the network. We shall define an epidemic in the SIR model as instability of the basic DFE under such perturbations. First, we look to linearise the difference equation for $P_{I_i}(t_{n+1})$ near the basic DFE, this translates to linearising the non-linear function $\Psi_i(t_n)$. Under the assumption $P_{I_i}(t_n) = \epsilon_i$ for every vertex i such that $0 < \epsilon_i \ll 1$, we find,

$$0 \leq \frac{P_{S_i, I_j}(t_n)}{P_{S_i}(t_n)} \leq \epsilon_j \quad (3.36)$$

by the fact that for the joint probability $P_{S_i, I_j}(t_n) \leq \min\{P_{S_i}(t_n), P_{I_j}(t_n)\}$. Thus for $\epsilon_i \ll 1$ we may assume $\frac{P_{S_i, I_j}(t_n)}{P_{S_i}(t_n)} \approx \epsilon_j$. Upon substituting this into $\Psi_i(t_n)$ we find that

$$\begin{aligned} \Psi_i(n) &\approx \prod_{k \in V} \left(1 - \beta \mathcal{A}_{ik}^{[t_n]} \epsilon_k\right) \\ &\approx 1 - \sum_{k \in V} \beta \mathcal{A}_{ik}^{[t_n]} \epsilon_k, \end{aligned} \quad (3.37)$$

We can then use this to linearise $P_{I_j}(t_{n+1})$ from Eq. (3.27). While $\epsilon_i \ll 1$ holds, so does the approximation,

$$P_{I_i}(t_{n+1}) \approx P_{I_i}(t_n)(1 - \mu) + \sum_{k \in V} \beta \mathcal{A}_{ik}^{[t_n]} P_{I_k}(t_n). \quad (3.38)$$

This linearisation eliminates $P_{S_i}(t_n)$ from the equation. Interestingly, this is exactly the form of the SIS model in the TIB framework for which the epidemic threshold is easily found [189]. Therefore, we find that the SIS and SIR models share the same epidemic threshold condition. We introduce the matrix $\mathbf{M}^{[t_n]}$, called the infection propagator, which is a linear map that describes the evolution of the SIR model close to the basic DFE:

$$M_{ij}^{[t_n]} = \beta \mathcal{A}_{ij}^{[t_n]} + \delta_{ij}(1 - \mu). \quad (3.39)$$

Following Ref. [189], we find that the condition required for an epidemic to occur is given by

$$\rho(\mathcal{M}) = \rho\left(\mathbf{M}^{[t_{n_t}]} \prod_{k=1}^{n_t-1} \mathbf{M}^{[t_k]}\right) > 1, \quad (3.40)$$

where \mathcal{M} is the infection propagator written in terms of the supra adjacency matrix [25] and ρ is the spectral radius operator, i.e., it gives the largest eigenvalue by magnitude. The matrix \mathcal{M} is given by,

$$\mathcal{M} = \begin{pmatrix} \mathbf{0} & \mathbf{M}^{[t_1]} & \mathbf{0} & \dots & \dots & \mathbf{0} \\ \mathbf{0} & \mathbf{0} & \mathbf{M}^{[t_2]} & \dots & \dots & \mathbf{0} \\ \mathbf{0} & \mathbf{0} & \mathbf{0} & \dots & \dots & \mathbf{0} \\ \vdots & \vdots & \vdots & \ddots & & \vdots \\ \mathbf{0} & \mathbf{0} & \mathbf{0} & & \ddots & \mathbf{M}^{[t_{n_t-1}]} \\ \mathbf{M}^{[t_{n_t}]} & \mathbf{0} & \mathbf{0} & \dots & \dots & \mathbf{0} \end{pmatrix}. \quad (3.41)$$

For the values of β and μ which the above Eq. (3.40) is satisfied, implies that when a disease is introduced into the network the basic DFE is unstable for a period of time. What this means is that in the equivalent SIS model with the same parameters, the proportion of infected vertices never settles on a DFE. We wish to show that the equivalence in Eq. (3.40) is true. First, we partition $\lambda \mathbf{Id} - \mathcal{M}$

into

$$\left(\begin{array}{c|cccc} \lambda \mathbf{Id} & -\mathbf{M}^{[t_1]} & \mathbf{0} & \dots & \dots & \mathbf{0} \\ \hline \mathbf{0} & \lambda \mathbf{Id} & -\mathbf{M}^{[t_2]} & \dots & \dots & \mathbf{0} \\ \mathbf{0} & \mathbf{0} & \lambda \mathbf{Id} & \dots & \dots & \mathbf{0} \\ \vdots & \vdots & \vdots & \ddots & & \vdots \\ \mathbf{0} & \mathbf{0} & \mathbf{0} & & \ddots & -\mathbf{M}^{[t_{n_t}-1]} \\ -\mathbf{M}^{[t_{n_t}]} & \mathbf{0} & \mathbf{0} & \dots & \dots & \lambda \mathbf{Id} \end{array} \right), \quad (3.42)$$

then, by use of the following formula for the determinant of 2×2 block matrices, which is derived by applying the determinant to Schur's complement, we may say that,

$$\det \begin{pmatrix} \mathbf{A} & \mathbf{B} \\ \mathbf{C} & \mathbf{D} \end{pmatrix} = \det(\mathbf{A}) \times \det(\mathbf{D} - \mathbf{C}\mathbf{A}^{-1}\mathbf{B}), \quad (3.43)$$

where $\mathbf{A}, \mathbf{B}, \mathbf{C}$ and \mathbf{D} are matrices of sizes $p \times p$, $p \times q$, $q \times p$ and $q \times q$ respectively. Then from the above partitioning we get,

$$\det(\lambda \mathbf{Id} - \mathcal{M}) = \det(\lambda \mathbf{Id}) \det \left(\lambda \mathbf{Id} - \mathcal{M}_1 + \frac{1}{\lambda} \mathbf{E}_1 \right), \quad (3.44)$$

where the two new matrices introduced are given as,

$$\mathcal{M}_k = \begin{pmatrix} \mathbf{0} & \mathbf{M}^{[t_{k+1}]} & \mathbf{0} & \dots & \dots & \mathbf{0} \\ \mathbf{0} & \mathbf{0} & \mathbf{M}^{[t_{k+2}]} & \dots & \dots & \mathbf{0} \\ \mathbf{0} & \mathbf{0} & \mathbf{0} & \dots & \dots & \mathbf{0} \\ \vdots & \vdots & \vdots & \ddots & & \vdots \\ \mathbf{0} & \mathbf{0} & \mathbf{0} & & \ddots & \mathbf{M}^{[t_{n_t}-1]} \\ \mathbf{0} & \mathbf{0} & \mathbf{0} & \dots & \dots & \mathbf{0} \end{pmatrix}, \quad (3.45)$$

and

$$\mathbf{E}_k = \begin{pmatrix} \mathbf{0} & \mathbf{0} & \dots & \dots & \mathbf{0} \\ \vdots & \vdots & \ddots & & \\ \mathbf{0} & \mathbf{0} & & \ddots & \mathbf{0} \\ \mathbf{M}^{[t_{n_t}]} \prod_i^k \mathbf{M}^{[t_i]} & \mathbf{0} & \dots & \dots & \mathbf{0} \end{pmatrix}. \quad (3.46)$$

By continuing the partitioning of the matrices in this way, we are able to reduce

the determinant to,

$$\begin{aligned}
\det(\lambda \mathbf{Id} - \mathbf{M}) &= \det(\lambda \mathbf{Id}) \det \left(\lambda \mathbf{Id} - \mathbf{M}_1 + \frac{1}{\lambda} \mathbf{E}_1 \right) \\
&= \det(\lambda \mathbf{Id})^2 \det \left(\lambda \mathbf{Id} - \mathbf{M}_2 - \frac{1}{\lambda^2} \mathbf{E}_2 \right) \\
&\vdots \\
&= \det(\lambda \mathbf{Id})^{n_t-2} \det \left(\lambda \mathbf{Id} - \mathbf{M}_{n_t-2} + \frac{(-1)^{n_t}}{\lambda^{n_t-1}} \mathbf{E}_{n_t-2} \right) \\
&= \det(\lambda \mathbf{Id})^{n_t-1} \det \left(\lambda \mathbf{Id} + \frac{(-1)^{n_t}}{\lambda^{n_t-1}} \mathbf{E}_{n_t-1} \right).
\end{aligned} \tag{3.47}$$

Now, by computing the determinant for the identity matrix and substituting in the expression for \mathbf{E}_{n_t-1} , we find that the above expression is given as,

$$\begin{aligned}
\det(\lambda \mathbf{Id} - \mathbf{M}) &= \lambda^{n_t(n_t-1)} \det \left(\lambda \mathbf{Id} + \frac{(-1)^{n_t}}{\lambda^{n_t-1}} \mathbf{E}_{n_t-1} \right) \\
&= \det \left(\lambda^{n_t} \mathbf{Id} + (-1)^{n_t} \mathbf{M}^{[t_{n_t}]} \prod_k^{n_t-1} \mathbf{M}^{[t_k]} \right),
\end{aligned} \tag{3.48}$$

thus proving that the largest eigenvalue, λ_{\max} , of the matrix \mathbf{M} is equivalent to $\sigma_{\max}^{n_t}$, where σ_{\max} is the maximum eigenvalue of $\mathbf{M}^{[t_{n_t}]} \prod_k^{n_t-1} \mathbf{M}^{[t_k]}$.

We now aim to test the accuracy of our TPB model compared to the TIB model and investigate under what graph structures it performs well. We also test our findings for the epidemic threshold.

3.5 Results

In this section, we compare the accuracy of the TIB model and the TPB model against the ground truth MC average, that is, direct stochastic simulations. In short, we show how the TPB model can offer a massive increase in accuracy and also discuss when it fails to accurately capture the true dynamics of the stochastic SIR process. Furthermore, we validate the analytical epidemic threshold.

3.5.1 Synthetic Networks

Now we test our results on a number of randomly generated static graphs, including that of a tree-graph in order to test our hypothesis that our TPB model is exact on tree-graphs. In total, we consider 4 different randomly generated graphs, all consisting of 100 vertices. They are Erdős-Rényi, Barabási-Albert, Watts-Strogatz and random tree-graphs respectively. For the first 3 mentioned random graphs, see Sec. 2.1.1 for details of their construction. Details on the parameters used in the graphs generation follow.

The assumption in the TPB model is conditional independence between vertices with a neighbour in common, given the common neighbours state, is equivalent to assuming the graph contains only a single time-respecting NBT path between any two vertices. In the case of an undirected static graph, this condition is equivalent to implying the graph is a tree-graph.

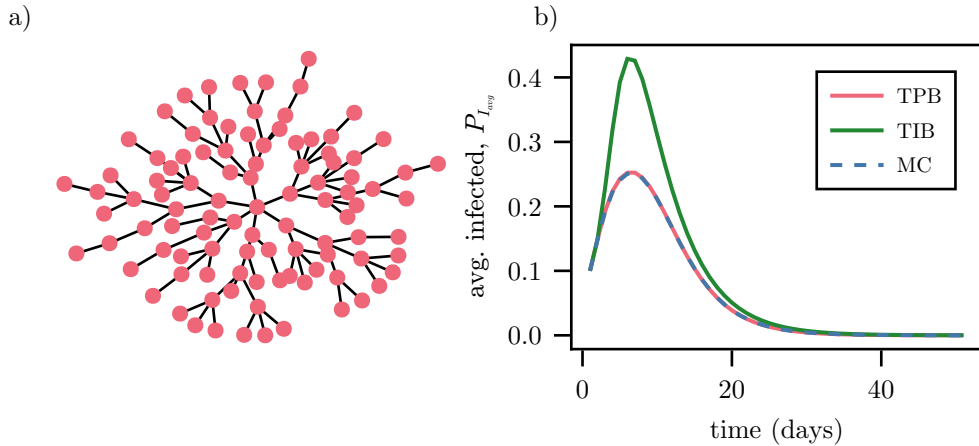


Figure 3.4: (a) A random tree network made up of 100 vertices. The tree is generated by taking the breadth first search tree starting from a randomly selected vertex of an Erdős-Rényi graph with connection probability $p = 0.05$. (b) Time series of the TIB (solid green) and TPB (solid red) SIR model as well as 10^5 Monte-Carlo (MC) simulations (dashed blue) for the tree network shown in panel (a). The parameters used were $\beta = 0.4$, $\mu = 0.02$, and $P_{I_k}(0) = 0.1$ for all vertices.

To illustrate this reasoning, we consider a static tree graph. In order to generate the graph, we start with a randomly generated Erdős-Rényi graph where the probability of two vertices being connected by an edge is $p = 0.05$. We then

randomly choose a vertex and perform a breadth first search (see Refs. [28, 145] for more details on graph search algorithms). The resulting breadth first search tree produces a random tree graph. All vertices start from some initial non-zero probability $P_{I_i}(0) = 0.1$ of being infected. We then run the TIB model and the TPB model for the parameters $\beta = 0.4$ and $\mu = 0.2$ and compare it to the ground truth, which is the average of a number of MC realisations. Fig. 3.4 b) plots the average probability of a vertex belonging to state I according to each model, that is $P_{I_{\text{avg}}} = \frac{1}{n_v} \sum_{k=1}^{n_v} P_{I_k}$. The TIB model is depicted as the solid red curve, the TIB model is shown as the solid green curve and the average of the MC realisations is shown as the dashed blue curve. The figure shows how the TIB model fails to capture the true SIR process on the graph due to the previously discussed echo chamber induced by assuming statistical independence of vertices. It becomes clear that the TPB model accurately describes the underlying SIR process for this simple example as each vertex is able to recover the dynamic correlations of past interactions with direct neighbours. As we will see from the next section, temporal graphs that are well approximated by tree-graphs are also well approximated by the TPB model.

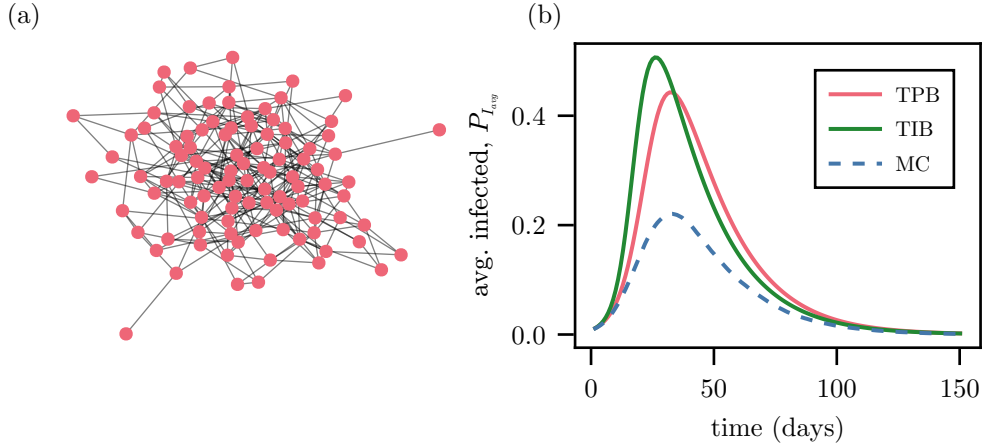


Figure 3.5: (a) A random Erdős-Rényi graph made up of 100 vertices. The probability of connection was taken as $p = 0.05$. (b) Time series of the TIB (solid green) and TPB (solid red) SIR model as well as 10^5 Monte-Carlo (MC) simulations (dashed blue) for the Erdős-Rényi graph shown in panel (a). The parameters used were $\beta = 0.05$, $\mu = 0.005$, and $P_{I_k}(0) = 0.01$ for all vertices.

As we have established the case in which our TPB model is exact, we turn

our attention to general graphs which permit more than 1 time-respecting path between any two vertices and thus, we should see our model deviate from the MC average. However, the question remains, in what cases does our model provide a substantial improvement over the IB model? We start with testing our model on an Erdős-Renyi random graph made up of 100 vertices. We set the probability of connection between vertices at $p = 0.05$. In Fig. 3.5 (b), we show the results of running the TIB, TPB, and the average of 10^5 MC realisations of the SIR model on a realisation of the Erdős-Renyi graph. We run each model for 500 time steps and set the parameters to $\beta = 0.05$ and $\mu = 0.05$. The average probability of being in the infected state across the entire graph is plotted for each model, with the TPB model given by the solid red curve, the TIB model given by the solid green curve, and the average of the MC realisations given as the green dashed curve. Looking at the curves, we see both models fail to line up with the MC average, however the IB model appears to perform worse by attaining a larger peak of average probability of infection when compared to the PB model. The TPB would appear to perform worse in the later stages, however this is explained by the IB depleting its pool of “susceptible probability” early on, as seen by the higher peak, thus in the later stages there is a higher probability that vertices have already recovered, and thus, less of a probability of them being currently infected.

Next we turn to the Barabási-Albert model. We generate a random Barabási-Albert directed graph consisting of 100 vertices. We start the graph with 2 unconnected vertices, then at each step of constructing the graph, we add a new vertex with 2 out edges, the probability of which vertices these edges connect to is outlined in Sec. 2.1.1. This process is repeated until 100 vertices are reached (see Fig. 3.5 (a) for a visualisation of the generated graph). In a fashion similar to the previous example, we run the TPB, TIB models, as well as compute the average of 10^5 MC realisations of the SIR model on our random graph. The results of running the models using $\beta = 0.05$ and $\mu = 0.05$ is given in Fig. 3.6 (b), which shows the average probability of being in the infected state across the entire graph with the TPB model given by the solid red curve, the TIB model given by the solid green curve, and the average of the MC realisations given by

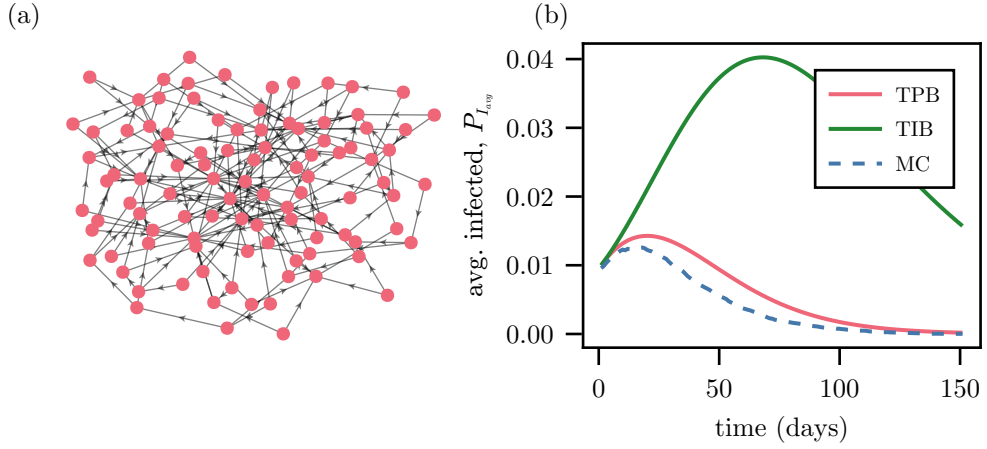


Figure 3.6: (a) A random Barabási-Albert directed graph made up of 100 vertices. The graph construction starts with unconnected vertices with a vertex with two out edges being added at each step of the construction. (b) Time series of the TIB (solid green) and TPB (solid red) SIR model as well as 10^5 Monte-Carlo (MC) simulations (dashed blue) for the Barabási-Albert graph shown in panel (a). The parameters used were $\beta = 0.05$, $\mu = 0.005$, and $P_{I_k}(0) = 0.01$ for all vertices.

the dashed blue curve. In this case, it is clear that the TPB produces far more accurate results by lying closer to the MC average when compared to the TIB model which appears to produce quite different dynamics.

The last synthetic graph type we consider is the Watts-Strogatz graph. Like in the previous examples, we construct a graph with 100 vertices. We initialise a graph in a ring, where each vertex is connected to the neighbour to its left and right (thus each vertex has a degree of 2), then with probability $p = 0.05$, each of the edges has one of its incident vertices randomly reassigned. The generated graph is depicted in Fig. 3.7 a). We then run the TPB and TIB SIR models on the graph and compare it to the average of 10^5 MC realisations. The parameters used in this case were $\beta = 0.15$ and $\mu = 0.05$. Fig. 3.7 b) shows the average probability of being in the infected state across the whole graph for the TPB model as the solid red curve, the TIB as the solid green curve, and average of the MC realisations as the dashed blue curve. For this graph, we achieve remarkable agreement between the TPB model and MC average, likely due to the fact that the graph is very close to a tree structure. The TIB model on the other hand overestimates the prevalence of the disease by a huge amount.

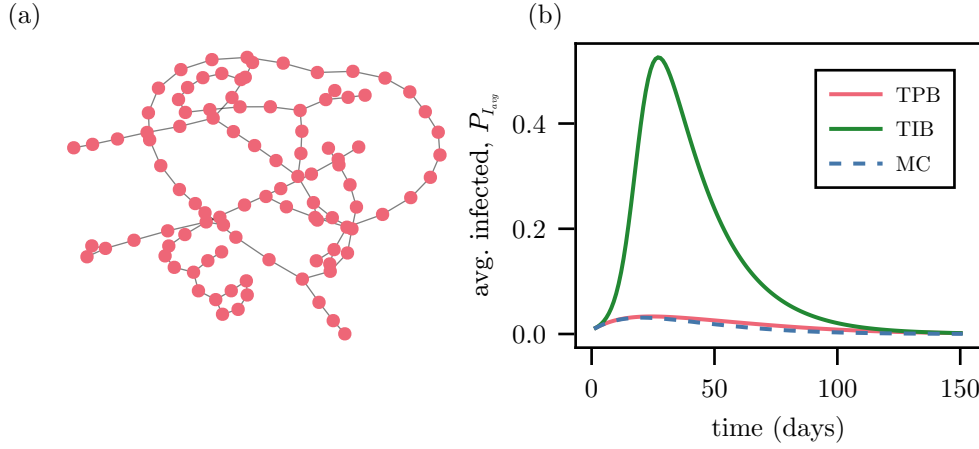


Figure 3.7: (a) A random Watts-Strogatz graph made up of 100 vertices. The graph starts as a ring with each vertex connected to the vertex to its left and right. Then each edge has an incident vertex reassigned with probability $p = 0.05$. (b) Time series of the TIB (solid green) and TPB (solid red) SIR model as well as 10^5 Monte-Carlo (MC) simulations (dashed blue) for the Watts-Strogatz graph shown in panel (a). The parameters used were $\beta = 0.15$, $\mu = 0.005$, and $P_{I_k}(0) = 0.01$ for all vertices.

We have seen that our TPB model appears to perform better on particular graph structures with few possible time-respecting NBT paths between vertices. As a result, we look at the number of possible time-respecting NBT paths in each of the synthetic networks analysed and compare this to the performance of the TPB models in each case. In order to quantify the number of time-respecting NBT paths are possible in the network, we introduce the non-backtracking accessibility matrix, a concept inspired by the accessibility matrix in Ref.[122]. First, we define the non-backtracking matrix of a temporal graph as,

$$B_{e,f}^{[t_{k_1}, t_{k_2}]} = \begin{cases} 1, & \text{if } e_2 = f_1, e_1 \neq f_2 \text{ and } e \in E_{k_1}, f \in E_{k_2}, \\ 0, & \text{otherwise,} \end{cases} \quad (3.49)$$

where t_{k_1}, t_{k_2} are time steps such that $t_{k_1} < t_{k_2}$ and $e = (e_1, e_2)$ and $f = (f_1, f_2)$ are edges active at those times, respectively. Of course for static graphs, all edges are active for all time, this description becomes more useful when we consider the temporal empirical networks in the following section. Note that the NBT matrix is defined over two time-steps and is indexed over the aggregated edge set $E_{agg} = \bigcup_{k=1}^{n_t} E_k$. This matrix tells us if it is possible to traverse an edge e at time

t_{k_1} and then traverse edge f at time t_{k_2} given that the edge f starts from where edge e finished and f does not bring us back to where e started from. Using this matrix, we define the NBT accessibility matrix as,

$$\mathcal{B}^{[t_l]} = \prod_{k=2}^l \otimes (\text{Id} \oplus \mathbf{B}^{[t_{k-1}, t_k]}), \quad (3.50)$$

where the two operations \otimes and \oplus are Boolean multiplication and addition respectively [131], and so the matrix \mathcal{B} is a binary matrix. Thus, the element $\mathcal{B}_{e,f}^{[t_l]}$ tells us if there is a NBT path that starts with traversing e and ends by traversing f which is up to length l at up to time t_l . Now, in order to determine how many possible paths there are between any two vertices up to length l , we define two new matrices, the in and out incidence matrices. Let the in-incidence matrix of a graph, J^{in} , be given by,

$$J_{i,e}^{\text{in}} = \begin{cases} 1, & \text{if edge } e \text{ is an in edge of vertex } i \\ 0, & \text{otherwise,} \end{cases} \quad (3.51)$$

and let the out-incidence matrix of a graph, $J_{i,e}^{\text{out}}$, be given by, temporal graph, where,

$$J_{i,e}^{\text{out}} = \begin{cases} 1, & \text{if edge } e \text{ is an out edge of vertex } i \\ 0, & \text{otherwise.} \end{cases} \quad (3.52)$$

Now, we transform $\mathcal{B}^{[t_l]}$ from the edge space to the vertex space by using the two incidence matrices defined above. This will allow us to determine how many unique NBT paths (unique in the route taken and not the times edges are traversed) there are between any two vertices up to length l at up to time t_l from the expression,

$$\mathcal{C}^{[t_l]} = \mathbf{J}^{\text{out}} \mathcal{B}^{[t_l]} \mathbf{J}^{\text{in}^T}. \quad (3.53)$$

The quantity $\mathcal{C}_{ij}^{[t_l]}$ is a matrix indexed over the vertices, which tells how many unique NBT paths there from vertex i to j . In a graph for which the TPB model is exact, each entry in this matrix would be at most one. We call the proportion of entries in the matrix $\mathcal{C}^{[t_l]}$ greater than one, the NBT reachability proportion

and denote it by $c(t_l)$.

In Fig. 3.8 we plot the NBT reachability proportion from time 1 up to 50 for each of the synthetic networks shown in Figs. 3.5, 3.6, and 3.7. In other words we plot the proportion of vertex pairs which have more than 1 NBT path connecting them. The red curve refers to the Erdős-Rényi graph, the green curve refers to the Barabási-Albert graph, and the blue curve refers to the Watts-Strogatz graph.

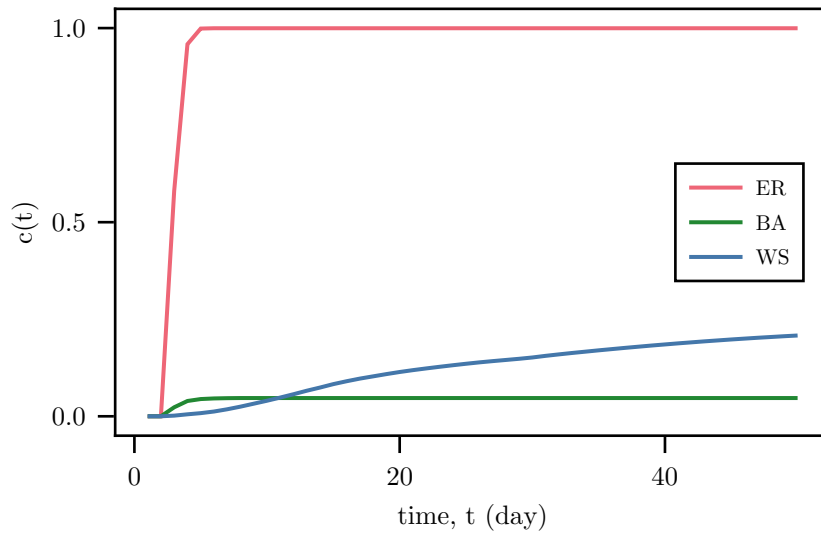


Figure 3.8: The NBT reachability proportion, $c(t)$ of the synthetic networks given in Figs. 3.5, 3.6, and 3.7. The red curves refer to the Erdős-Rényi (ER) graph, the green curves refer to the Barabási-Albert (BA) graph, and the blue curves refer to Watts-Strogatz graph. For each graph, the $c(t)$ was computed for 50 time steps.

We see that the NBT reachability proportion in the Erdős-Rényi graph approaches one almost immediately, far surpassing both the Barabási-Albert graph and the Watts-Strogatz graph. The Barabási-Albert and Watts-Strogatz graphs attain far lower values, with the Watts-Strogatz graph starting lower, but eventually surpassing the Barabási-Albert graph. These results appear to line up with the agreement between the MC averages and the TPB models for each of the considered synthetic graphs. The Erdős-Rényi graph, with the highest NBT reachability proportion, performs almost as poorly as the IB model, whereas the other 2 graphs, with very low proportions, perform far better than the IB model.

Now, we will validate our analytical findings for the epidemic threshold of the TPB SIR process. For this purpose, we fix a value for μ and then for increasing values of β , perform a number of MC simulations for long times in order to get a distribution of the final outbreak size, which is given by $R_\infty = \lim_{n \rightarrow \infty} \frac{1}{n_v} \sum_{k=1}^{n_v} P_{R_k}(n)$. Again, we use the same generated synthetic graphs as given in Figs. 3.5, 3.6, and 3.7, on which we run the models and MC simulations. In the long-term dynamics of the SIR process, R_∞ , will usually exceed the observation time of the network. Therefore, periodicity of the networks is assumed in a similar way to Ref. [189] when computing the final outbreak sizes.

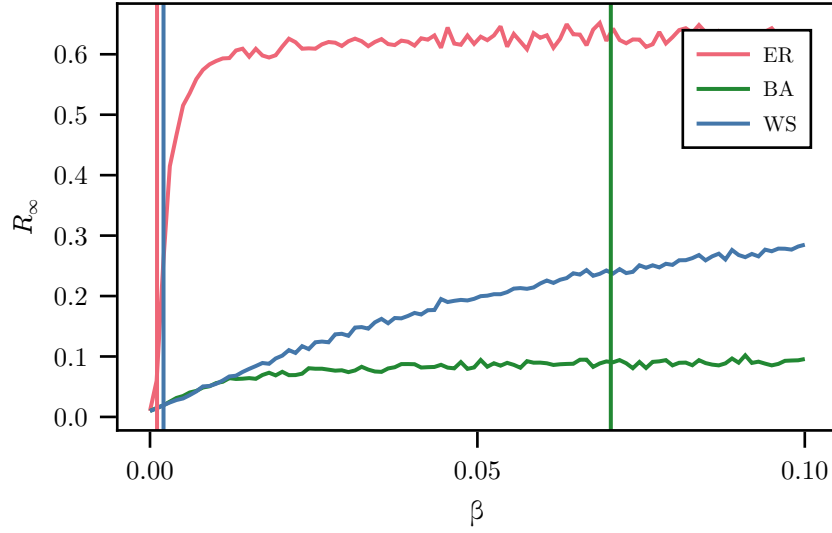


Figure 3.9: The final outbreak size, R_∞ , for the random graphs given in the Figs. 3.5, 3.6, and 3.7. The red curves refer to the Erdős-Rényi (ER) graph, the green curves refer to the Barabási-Albert (BA) graph, and the blue curves refer to Watts-Strogatz graph. R_∞ was computed for different values of β with a fixed value of $\mu = 0.05$. For each graph, R_∞ was taken as the average of the final number of recovered individuals of 10^3 MC simulations for each value of β . The initial conditions of each simulation was set so that each individual had a 0.01 chance of starting infected. For each graph, the analytically computed critical β at which the epidemic threshold becomes greater than one is plotted as a vertical curve of the same colour.

In Fig. 3.9 we see the distribution of final outbreak proportions for each random graph against their critical β as computed from the epidemic threshold of the TPB model. For the parameters, we fix μ at the value 0.05 and then vary β for from 0 up to 0.1, running 10^3 MC simulations for each of the values of β . We then plot the average final outbreak size, R_∞ , of each of these 10^3 simulations as the red curve for the Erdős-Rényi graph, the green curve for Barabási-Albert

graph and the blue curve for the Watts-Strogatz graph. We then compute the analytical epidemic threshold for this value of μ from Eq.3.40 for each of the considered graphs, and plot those values as vertical lines. The epidemic threshold for the Erdős-Rényi graph is given as the red vertical line, for the Barabási-Albert graph as the green line, and the Watts-Strogatz graph as the blue line. Note that the epidemic threshold of the Erdős-Rényi and Watts-Strogatz lie very close together.

For values of β that are greater than the computed epidemic threshold in the Erdős-Rényi and Watts-Strogatz graphs, there is an obvious but gradual change in dynamics as local outbreaks no longer die out, but now propagate throughout the network leading to larger final outbreak sizes, thus showing agreement with the analytical result for the epidemic threshold. However, this change in dynamics is not as clear in the case of the Barabási-Albert graph, where the epidemic threshold is far higher than in the other two cases. It is important to note as well that this difference in the epidemic threshold is due to the difference in network structure as the value for μ is held constant in each case. The Barabási-Albert R_∞ values appear to level off before the epidemic threshold and don't increase after it. This likely due to the network structure itself being particularly robust against epidemics, in part because of its directedness.

Overall, for the considered synthetic graphs, our model offers large improvements over the individual based model for all cases except the case of the Erdős-Rényi graph, but still does not overestimate the peak as much as the IB model, thus still offering an improvement. We have also confirmed that our model is exact on tree graphs. So far we have not considered temporal graphs or graphs generated from empirical data, and so, in the next section we test the performance of our model on 2 real world temporal networks.

3.5.2 Empirical Networks

In this section, we consider two empirical temporal networks that both vary in structure and temporal activity. For each of the empirical networks we wish to

test our findings that the TPB model offers an increase in accuracy over the TIB model. Similarly to previous section where we test our models on synthetic networks, we run the TIB and TPB SIR models for all the empirical networks for given values of β and μ and then compare them to the average of a sufficiently large number of MC simulations. This allows us to quantify how well the different models approximate the dynamics of the true SIR process. The considered networks are now discussed and an overview of their properties are given in Tab. 3.1.

Table 3.1: List of empirical networks.

Network List				
Network	Vertices	Agg. Edges	Avg. Edges	Snapshots
Conference	405	9699	20.02	3509
Cattle Trades	111513	1041054	347.17	365

Irish Cattle Trade

The Cattle Trades network consists of all trades between herds within the Republic of Ireland during the year 2017 with a temporal resolution of one day [187] (cf. Tab. 3.1). Due to the nature of the trade data, interactions are directional. Thus, this data set is modelled by a directed graph, where each vertex represents a herd and each edge represents a trade weighted by the number of animals traded. The aggregated degree distribution of the graph as shown in Fig. 3.10 (b) indicates a scale-free behaviour often seen in empirical networks. The graph appears to be quite sparse as is evident from Fig. 3.10 (a), with an average of only 347 edges per day while having an aggregated 1,041,054 edges over the entire year. The data also displays a strong bi-modal seasonal trend with there being two distinct peaks while there tends to be very little trades occurring on Sundays when the data points lie near zero. Although we ignore external drivers of the disease, this model still offers insight into how susceptible to epidemics the graph is as trade is the main vector of non-local transmission. There are a number of infectious diseases that affect cattle, such as Foot and Mouth Disease and Bovine Tuberculosis, the latter of which is still a major problem in Ireland, thus effective models for the spread of infectious diseases among herds are particularly useful tools. In

the present study, we focus on the SIR dynamics, but the TPB model framework can easily be extended to other models,

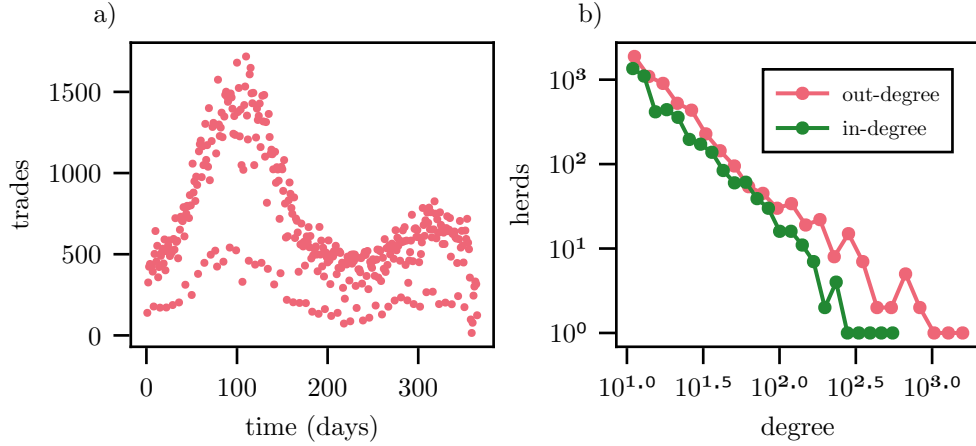


Figure 3.10: (a) Time series of number of active edges per day in the network. (b) In- and out-degree of the network aggregated over the entire year worth of data.

From Fig. 3.11 we can compare the performance of the TIB and TPB models on the cattle trades network. The figure shows a year worth of the average probability of being infected $P_{I_{\text{avg}}}$ of both models and the average of 10^3 MC realisations for the same choice of parameters. In both plots, the solid red curve refers to the TPB model, the solid green curve refers to the TIB model, and the dashed blue curve refers to the average of the MC realisations. The parameters used were $\beta = 0.5$ for the panel a) and $\beta = 0.3$ for panel b), in both cases $\mu = 0.005$ and the initial conditions were set to $P_{I_i}(0) = 0.01$ for every vertex.

As in the case of the synthetic graphs, we now look at what proportion of vertex pairs are connected by more than one NBT path, i.e., the NBT reachability proportion, as well as the final outbreak sizes, R_∞ , in comparison to the analytical epidemic threshold. In Fig. 3.12 (a) we see the evolution of the NBT reachability proportion over the course of a full year for the cattle trade network. It is quite clear from the figure that the proportion is particularly low over the time period, staying relatively close to zero for nearly 100 days. This helps provide insight into why the TPB model performs so well on this particular data set in comparison to

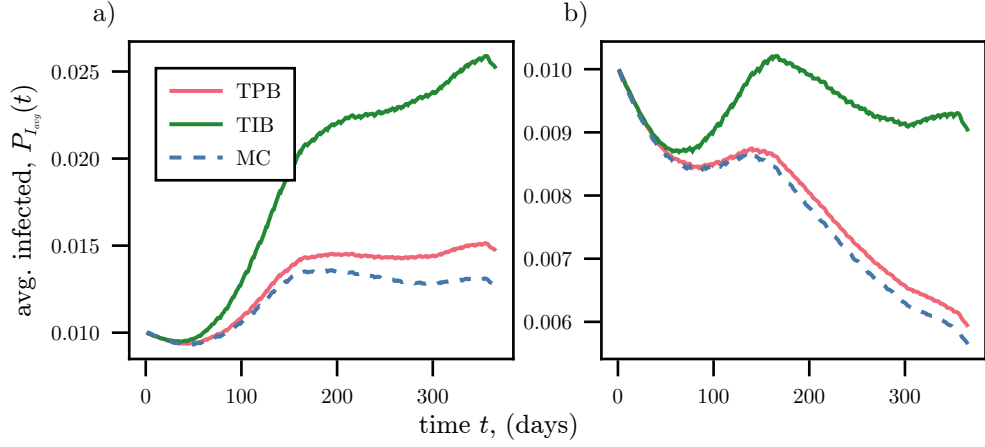


Figure 3.11: TIB (solid green) and TPB (solid red) SIR models on the Irish cattle trade network together with the average of 10^4 Monte-Carlo simulations (dashed blue). Panels (a) and (b) show the time series for the average probability of being infected $P_{I_{\text{avg}}}$, for different sets of parameters. Both panels assumed that $\mu = 0.005$ and initial conditions of $P_{I_i}(0) = 0.01$ for every vertex i , panel (a) uses $\beta = 0.5$ and panel (b) used $\beta = 0.3$.

the TIB model. The low NBT reachability proportion means that there are few opportunities for echo chambers to occur as in the example given in Sec. 3.3.2, and so, this allows us to justify the use of the TPB model on this data set while the NBT reachability proportion remains low.

According to the analytical epidemic threshold as given by Eq. (3.40), we find the critical β for the cattle trade network to be 0.0049, given the value for μ as 0.005. This is plotted as the vertical line given in Fig. 3.12 (b). The other curve in this figure is the final outbreak sizes R_∞ for the same value of $\mu = 0.005$, but for varying values of β . We compute the final outbreak size, R_∞ by running 10^3 MC realisations for each of the values of β until there are no infected individuals left, the initial condition of each run is set such that each individual has a random chance of 0.0001 of starting the simulation as infected. We then take the average of the final number of recovered individuals. The epidemic threshold in this case is very small and we can see that near the critical β , R_∞ stays very close to initial proportion of infected, but as β begins to increase further away from the critical value, R_∞ begins to increase rapidly.

As is evident from Fig. 3.11, the TPB model offers a significant improvement

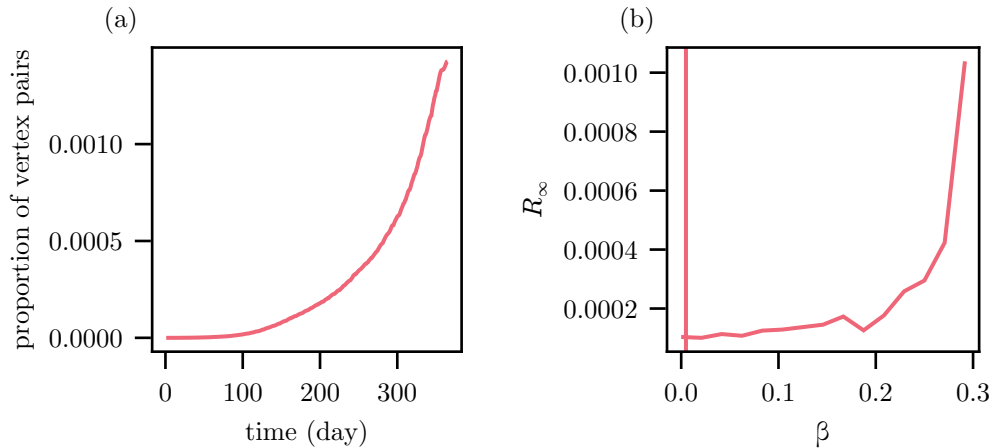


Figure 3.12: (a) The NBT reachability proportion of the cattle trade network over one year. (b) The final outbreak size, R_∞ , for different values of β with a fixed value of $\mu = 0.005$. R_∞ was computed from the average of the final number of recovered individuals of 10^3 MC simulations for each value of β . The initial conditions of each simulation was set so that each individual had a 0.0001 chance of starting infected. The analytically computed critical β at which the epidemic threshold becomes greater than one is plotted as the vertical line.

over the TIB model as there is far better agreement with the MC average for both sets of parameters, with the IB model deviating quite far. The reason for such a significant improvement can be explained by the fact that the TPB model is exact on graphs where the NBT reachability proportion is zero. However, because the cattle trade network is a production network, there exist very few scenarios where there are many possible NBT paths between herds, making the graph structure highly tree-like in its supra-adjacency embedding. This can be explained by the fact that the existence of such cycles are inefficient and cost prohibitive in the trade process. As a result the graph is well approximated by a tree-graph. Therefore, the SIR process is well approximated by the TPB model for such a graph.

Conference Contacts

The second data set (cf. Tab. 3.1) is the Conference network described in Ref. [75]. It includes the face-to-face interactions of 405 participants at the SFHH conference held in Nice, France 2009. Each snapshot of the network represents the

aggregated contacts in windows of 20s. Since this data set describes face-to-face interactions, each contact is bi-directional and so an undirected graph is the natural choice to model these interactions.

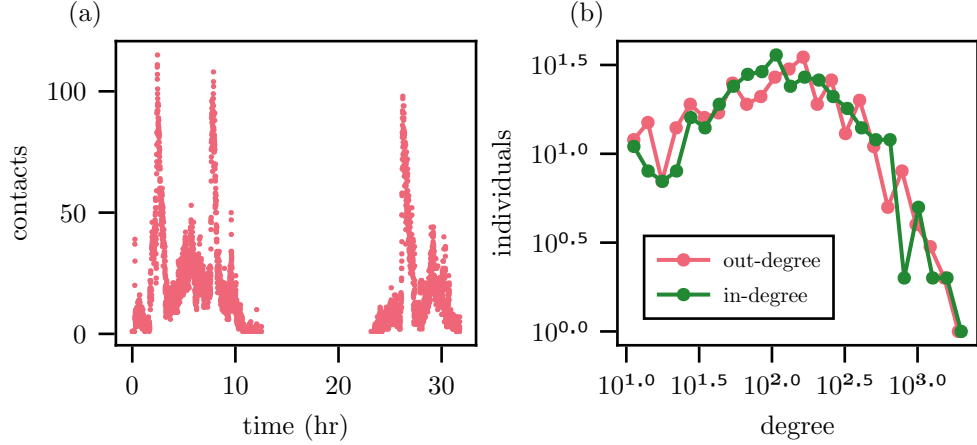


Figure 3.13: (a) Time series of number of active edges per time-step in the network. (b) In- and out-degree of the network aggregated over the entire data set.

In Fig. 3.13 (a) we see that the edge activity in this case shows a number of peaks occurring then quickly dying out with a large break of no activity for many hours. These are explained by breaks between sessions at the conference during which the participants converse and interact as well as an overnight break as the conference lasted more than 24 hours. Because of the time scale and observation period of this particular temporal graph, it is not feasible to model the spread of disease as infection and recovery is unlikely to occur within the observation period, which is approximately 30 hours. However, we can use our model to simulate the spread of viral information or “gossip” using the same dynamics as the SIR model. Infection is equivalent to receiving some information in such a way that it becomes interesting enough to for the individual to try and spread to those they contact in the future and recovery is equivalent to growing tired of the information and no longer inform others they meet. As shown in Fig. 3.13(b), there is a clear heavy tail with most vertices having a relatively small aggregated degree, meaning most individuals had relatively few interactions in comparison to the most popular individuals.

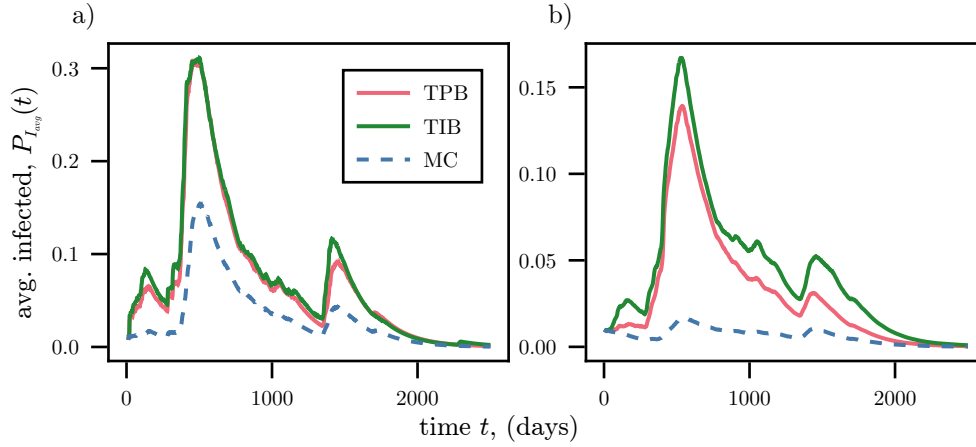


Figure 3.14: TIB (solid green) and TPB (solid red) SIR models on the conference network together with the average of 10^4 Monte-Carlo simulations (dashed blue). Panels (a) and (b) show the time series for the average probability of being infected $P_{I_{\text{avg}}}$, for different sets of parameters. Both panels assumed that $\mu = 0.005$ and initial conditions of $P_{I_i}(0) = 0.01$ for every vertex i , panel (a) uses $\beta = 0.5$ and panel (b) used $\beta = 0.05$.

Fig. 3.14 shows the time series of the different models for two probabilities of infection: $\beta = 0.5$ in (a) and $\beta = 0.05$ in (b). In both cases the $\mu = 0.05$ and the initial condition for each vertex is given as $P_{I_i}(0) = 0.01$. In both panels, the average probability of belonging to the infected compartment, $P_{I_{\text{avg}}}$, is plotted for the TPB model as the solid red curve, for the TIB curve as the solid green curve, and the average of the 10^4 MC realisations as the dashed blue curve. Again, one can observe that in every case the TPB approximation offers an improvement over the TIB. However, compared to the MC simulations, it still performs quite poorly, barely outperforming the IB model in panel (a).

In order to explain why the TPB model fails to provide a reasonable increase in accuracy when compared to the TIB model for this particular data set, we look at the NBT reachability proportion over time in Fig. 3.15 (a). When compared to the equivalent plot for the cattle trade dataset in Fig 3.12 (a), the NBT reachability proportion in this data set is far higher, with approximately a 10 times difference between scales. This can be compared to the NBT reachability proportion of the Erdős-Rényi graph in Fig. 3.8, which has a similar scale in NBT reachability proportion and performs approximately the same as the TIB model in the SIR

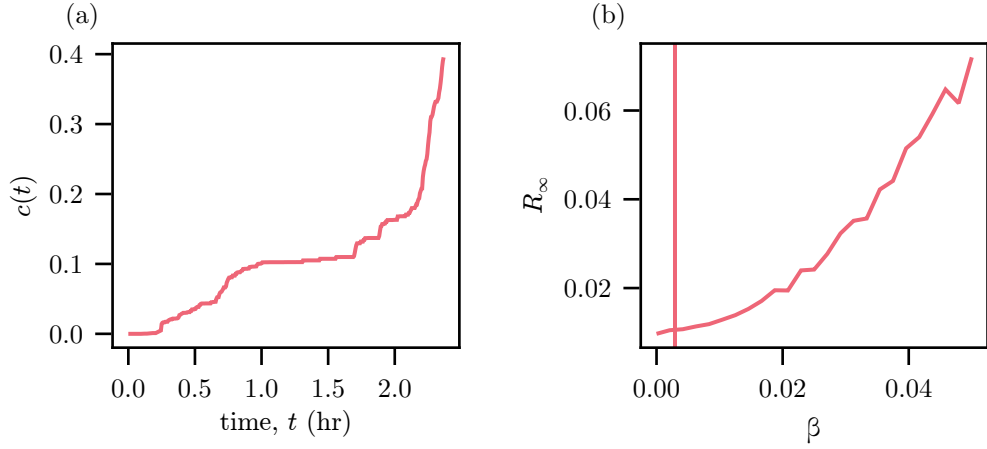


Figure 3.15: (a) The NBT reachability proportion of the conference network over the first 2.5 hours. (b) The final outbreak size, R_∞ , for different values of β with a fixed value of $\mu = 0.005$. R_∞ was computed from the average of the final number of recovered individuals of 10^3 MC simulations for each value of β . The initial conditions of each simulation was set so that each individual had a 0.01 chance of starting infected. The analytically computed critical β at which the epidemic threshold becomes greater than one is plotted as the vertical line.

simulations (cf. Figs. 3.5 and 3.14)

The reason we do not see a good agreement with the MC average for this particular data set is due to the underlying topology of the graph, which is a physical social interaction network where individuals congregate in groups and most or all in the group interact with one another. This leads to large clusters that give rise to many possible NBT paths between vertices. The more time-respecting NBT paths that exist between any two vertices, the worse the TPB model will perform. It is for this reason that we see a relatively large deviation from the MC simulations for the TPB model.

For the conference network, we computed the critical β to be 0.0029 for given the value of μ was taken to be 0.005. In Fig. 3.15 (b), we show how the final outbreak size R_∞ increases for varying values of β where we fix the value of μ at 0.005 and show the computed critical β as a vertical line. To compute R_∞ we run 10^3 simulations until there are no infected individuals left for each of our values of β and then take the average of the final number of recovered left. The initial conditions of each simulation was such that each individual had a probability

of 0.01 of starting infected. Similarly to the other scenarios, we see agreement between the analytical epidemic threshold critical β and the final outbreak sizes R_∞ . As the values of β move further away from this critical β , the final outbreak size R_∞ also begins to increase, whereas, below the critical value, R_∞ stays very close to the initial conditions.

3.6 Summary

In this chapter, we have presented work done on SIR PB models by systematically extending them to a temporal setting and investigating the effect of non-backtracking cycles on the accuracy of the model on arbitrary network structures. We have found that the existence of many such non-backtracking cycles leads to a deviation in the PB model from the true SIR process due to the echo chamber effect they induce. Thus, the PB model is best suited to network structures which do not contain many cycles, such as production networks. We also find that our analytical finding for the epidemic threshold holds up when compared to numerical simulations by, showing a qualitative change in the final outbreak proportion.

Chapter 4

A Meta-Population Model for the Spread of SARS-CoV-2

In this chapter we present results on an all-Ireland network modelling approach to simulate the spreading the Severe Acute Respiratory Syndrome Corona Virus 2 (SARS-CoV-2), commonly known as the *coronavirus*. In the model, vertices correspond to locations or communities that are connected by edges indicating travel and commuting between different locations. While this proposed modelling framework can be applied on all levels of spatial granularity and different countries, we consider the island of Ireland as a case study.

The network comprises 3440 Electoral Divisions (EDs) in the Republic of Ireland and 890 Super Output Areas (SOAs) in Northern Ireland, which corresponds to local administrative units far below the NUTS 3 regions. The local dynamics within each vertex follows a phenomenological SIRQ compartmental model including classes of Susceptibles, Infected, Recovered and Quarantined inspired from Ref. [132]. For better comparison to empirical data, we extend that model with a compartment for Deaths. We consider various scenarios including the 5-phase roadmap laid out by the Government for Ireland of Spring and Summer 2020. In addition, as proof of concept, we investigate the effect of dynamic non-pharmaceutical interventions that aim to keep the number of infected below a

given threshold. This is achieved by dynamically adjusting containment measures on a national scale, which could also be implemented at a regional (county) or local (ED/SOA) level. We find that – in principle – dynamic interventions are capable to limit the impact of future waves of outbreaks, but on the downside, in the absence of a vaccine, such a strategy can last several years until herd immunity is reached.

4.1 Overview

On 30th January 2020, the World Health Organisation (WHO) declared the newly emergent novel coronavirus pathogen, Severe Acute Respiratory Syndrome CoronaVirus 2 (SARS-CoV-2), to be a *public health emergency of international concern* [48, 148]. This characterisation was later updated to pandemic status on 11th March 2020 [44]. Following its initial detection in a cluster of patients experiencing acute respiratory symptoms in the city of Wuhan, in the Hubei province of China [38], the spread of SARS-CoV-2, which causes the coronavirus disease (COVID-19), globally in the months following led to unprecedented social and economic disruption [46, 55]. Despite widespread efforts to contain the virus through a series of non-pharmaceutical, and later, pharmaceutical interventions, global figures show cumulative reported cases standing at over 500 million, with deaths from the virus totalling over 6.3 million. From the start of the pandemic it was clear that there was an urgent and ongoing need to understand how the virus spreads, in order to effectively protect populations as the race to produce a vaccine began: an undertaking that in most cases would take years.

On the 16 March 2020, the first COVID-19 vaccine entered human trials [182]. In the coming months, mass vaccination campaigns began around the globe, with Ireland’s first dose given on 29 December 2020 [178]. Within the first month of vaccination campaigns beginning globally on 14th December, approximately 35 million doses were administered in 49 countries worldwide [50]. Immunisation of billions of people around the world was logistical tour de force, with the current figure standing at 4.78 billion individuals with at least one dose of vaccine, that

is, 61.2% of the world's population.

As COVID-19's grip on the world, as well as our daily lives begins to slip into distant memory, it is our duty to look back on events passed in order to assess the effectiveness of our models so that when, and not if, we are faced with another pandemic, we are better equipped with the proper mathematical tools to face the challenge swiftly and effectively. The effects of a global disease are most pronounced in the absence of an effective vaccine, thus, the models we will look at assume the absence of such. Until such pharmaceutical means are widely available, the best available mitigation strategies include the use of face masks, sanitisation, and social distancing. During the course of the COVID-19 pandemic, authorities implemented lockdowns to promote these measures. Mathematical models are invaluable in providing us with an insight into the processes by which the disease spreads [27, 112, 119, 130, 132, 154] and are able to help inform decisions on the best course of action to take in the form of non-pharmaceutical interventions [9, 157, 158, 168].

The model proposed in this chapter and the numerical results arising from it are to be understood as a contribution to the scientific and public discussion of possible spreading scenarios and the impact of intervention measures including realistic levels of compliance. We will clearly state the model ingredients and assumptions and elaborate on conclusions that can be drawn based on these limitations; some of which are unlikely for any practical purpose, but worth exploring, e.g., for worst-case scenarios.

We start with an introduction of the model equations for the local and networked dynamics in sections 4.2 and 4.3, respectively. This includes a discussion of the local dynamics from a geometric point of view, where we sketch the trajectories and equilibria in phase space. Then, we continue with a case study of Ireland in section 4.7 including realistic mobility data and compliance levels with respect to movement restrictions. Besides an unlikely, worst-case scenario, we consider different levels of increased awareness during the post-lock-down period in section 4.7.1. In addition, in section 4.7.2, we explore effects of dynamic interventions to keep the prevalence below a given level. These dynamic lockdowns

are considered at different levels of spatial granularity.

4.2 Local Dynamics

We start with the model for the local, well mixed dynamics at a single vertex as the basis for the network model. We assign proportions of the population belonging to one of 5 compartments, Susceptible (S), Infected (I), Quarantined (Q), Recovered (R) and Dead (D). Hence, we call this the SIQRD model. These compartments are defined as follows,

Susceptible S Individuals who have not been infected by the disease.

Infected I Individuals who are infected with the disease and are capable of transmission.

Quarantined Q Individuals who are infected with the disease, but are quarantined or self-isolating and thus not transmitting.

Recovered R Individuals who have recovered from the disease and are considered immune.

Dead D Individuals who have died from the disease.

We may model these class of models as a simple extension of the original Kermack and McKendrick SIR model [111], inspired by Ref. [132]. Between these five compartments, we assume that the number of individuals N , remains constant for all time. Note that those belonging to the D compartment do not contribute to the dynamics but still count towards the total population. Given that each individual may belong to just one compartment at any time, we model the flow of individuals from one compartment to another as given in Fig. 4.1. The rate of movement between compartments is given by the quantities which annotate the arrows and movements between compartments are only possible via these transmission/recovery/death routes. We use $S(t)$ to denote the number of

individuals belonging to S at time t and similarly for the other compartments. The reason we do not include a vaccination compartment is that we aim to model the spread of the disease in its absence, as was the case for the first year of the COVID-19 pandemic. It is under this condition in which the virus can have the largest impact.

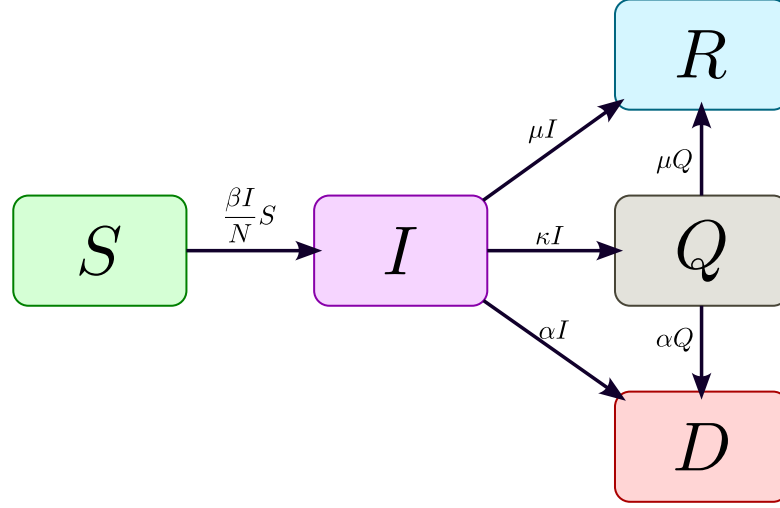


Figure 4.1: The rates at which individuals move from one compartment into another.

The set of equations which govern the dynamics as depicted in Fig. 4.1, are given by,

$$\frac{dS}{dt} = -\frac{\beta I}{N}S \quad (4.1a)$$

$$\frac{dI}{dt} = \frac{\beta I}{N}S - \mu I - \alpha I - \kappa I \quad (4.1b)$$

$$\frac{dQ}{dt} = \kappa I - \mu Q - \alpha Q \quad (4.1c)$$

$$\frac{dR}{dt} = \mu I + \mu Q \quad (4.1d)$$

$$\frac{dD}{dt} = \alpha I + \alpha Q. \quad (4.1e)$$

The above system of Ordinary Differential Equations (ODEs) assume homogeneous mixing of the population, which can be a good approximation for small communities, and small number of deaths. The parameters of the ODE model (4.1) refer to the rates of moving from one compartment to another and population

size:

β the rate of contact multiplied by the probability of infection on contact.

μ rate of recovery.

κ rate of moving from infected to quarantined.

α rate of death.

N total population size such that $N = S(t) + I(t) + Q(t) + R(t) + D(t)$.

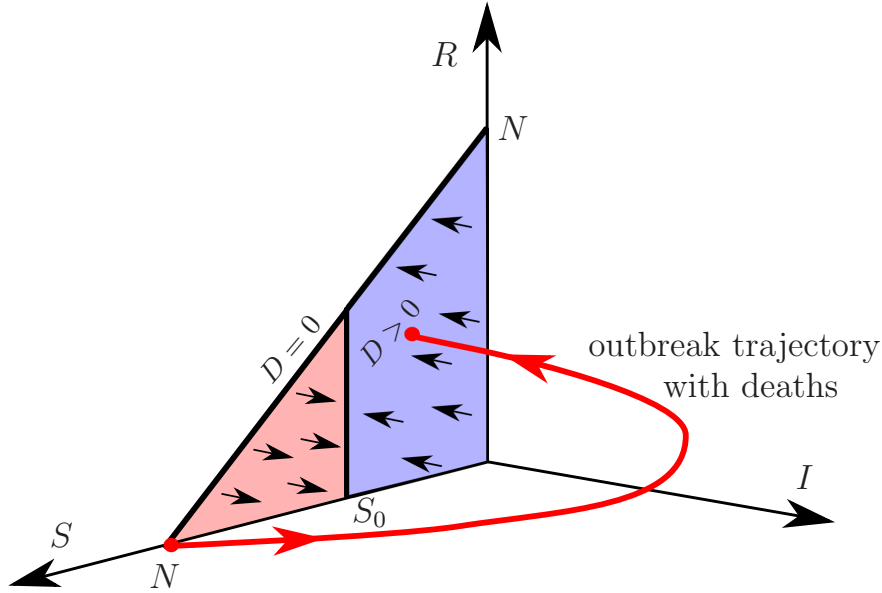


Figure 4.2: Sketch of the outbreak dynamics in the local SIQRD model (4.1) for $R_0 > 1$, shown as a (red) trajectory from the disease-free equilibrium $S_e = N$ to one of the stable equilibria with $0 < S_e < S_0$ in the projection of the (S, I, Q, R, D) phase space onto the (S, I, R) subspace. S_0 is the herd immunity threshold separating the triangular family of equilibria into the (pink) unstable and (blue) stable parts.

Much insight into the network dynamics can be gained from geometric analysis of the local, single-vertex dynamics as given in Eqs. (4.1). In the (S, I, Q, R, D) phase space, system (4.1) has a whole family of stationary solutions (equilibria). They are given by

$$I_e = Q_e = 0 \quad \text{and} \quad S_e + R_e + D_e = N, \quad (4.2)$$

which correspond to disease-free conditions, and form a triangular surface shown in Fig. 4.2. We refer to these state as the Disease-Free Equilibriums (DFEs). This family includes the important Basic Disease-Free Equilibrium (basic DFE),

$$S_e = N \quad \text{and} \quad I_e = Q_e = R_e = D_e = 0, \quad (4.3)$$

which is the state of the system before any infected individuals are introduced. To discuss stability of equilibria, it is convenient to define the basic reproduction number of the system which has been discussed in Chps. 2 and 3. This gives the expected number of secondary cases produced by a single infected individual introduced to the basic DFE. This can be obtained by either linearising the system of Eqs. (4.1) near the basic DFE or by finding the next generation matrix [54] of the system and finding its spectral radius. The latter approach is more useful for complicated models with many infectious compartments, which will be the case for the network model. The necessary condition for an epidemic to occur is that $\frac{dI}{dt} > 0$, thus we have,

$$\begin{aligned} \frac{\beta I}{N} S - \mu I - \alpha I - \kappa I &> 0. \\ \frac{\beta N}{(\alpha + \kappa + \mu) S} &> 1. \end{aligned} \quad (4.4)$$

The quantity on the left of the second inequality above is what we refer to as the *effective reproduction number*,

$$\mathcal{R}_0^* = \frac{\beta N}{(\alpha + \kappa + \mu) S}, \quad (4.5)$$

and gives the expected number infections produced by a single infected individual introduced to a DFE with the number of susceptibles being $S(t)$.

Suppose we perturb the state of the system at the basic DFE such that

$$[S, I, Q, R, D]^T = [N - \delta, \delta, 0, 0, 0]^T. \quad (4.6)$$

Upon substituting in $S = N$, the quantity on the left hand side of the second

inequality in Eq. (4.4), is the *basic reproduction number* of the local SIQRD model, which we denote,

$$\mathcal{R}_0 = \frac{\beta}{\alpha + \kappa + \mu}. \quad (4.7)$$

In other words the basic reproduction number is just the effective reproduction number at the basic DFE. When $0 < \mathcal{R}_0 < 1$, all equilibria are stable, meaning that no disease outbreaks can occur. When $\mathcal{R}_0 > 1$, the basic DFE turns unstable, and disease outbreaks become possible. To be more specific, the family of equilibria is divided into the (pink) unstable part with $\mathcal{S}_0 < S_e \leq N$, which contains the basic DFE, and the (blue) stable part with $0 \leq S_e < \mathcal{S}_0$, shown in Fig. 4.2. The instability threshold separating the two parts is given by

$$\mathcal{S}_0 = \frac{N}{\mathcal{R}_0}. \quad (4.8)$$

Guided by these observations, we define *herd immunity*, whether achieved naturally or by means of vaccination, in terms of stable equilibria. Herd immunity in a broad sense can be described as when the susceptible population becomes low enough that the disease is no longer able to spread as much of the population is already recovered or dead. In the local SIQRD model (4.1), we define herd immunity as a disease-free state of the system such that a small increase in infected I decays monotonically to zero (no outbreak). We say that the system has reached herd immunity when,

$$0 \leq S(t) < \mathcal{S}_0. \quad (4.9)$$

In other words, herd immunity is represented by a stable equilibrium. We call $\mathcal{S}_0 = N/\mathcal{R}_0$ the herd immunity threshold.

In Fig. 4.2, a disease outbreak is depicted as the (red) trajectory from the basic DFE, giving a peak in infected $I(t)$ around the herd immunity threshold \mathcal{S}_0 , to one of the (blue) herd immunity equilibria that lie below \mathcal{S}_0 . The lower the \mathcal{S}_0 , the higher the peak in $I(t)$. Thus, bringing the herd immunity threshold \mathcal{S}_0 closer to N for a period of time and then back to its original position, e.g., via imposing temporary public-health restrictions, can modify the outbreak trajectory so that ultimate herd immunity is achieved in a controlled way, that is, with a peak in

$I(t)$ that remains below some desired level.

4.3 Network Contagion Model

While the ODE model (4.1) can be justified for small communities, it fails at capturing the dynamics that occurs at large spatial scales and cannot account for heterogeneities in a population and interaction between meta-populations via mixing/commuting [22]. For this reason, we develop a network framework by splitting the population up into a number of smaller communities based on their geographic location. Ideally, these communities are small enough to justify a well mixed ODE model at the local level. We model our interaction/travel network as a simple weighted directed graph $G = (V, E, \omega)$. Every community $i \in V = \{1, \dots, M\}$, corresponds to a vertex in the network. The edge weights, $\omega(i, j) := \omega_{ij}$, between two vertices represent the rate of travel per unit time from locations i to j . The existence of an edge (i, j) implies there is travel from locations i to j , conversely, no edge implies there is no travel, and thus $\omega_{ij} = 0$. The rate of travel, ω_{ij} can vary with time or remain static. We denote the population of each vertex at time t as $N_i(t)$ such that the sum of all populations gives the total $N = \sum_{i \in V} N_i$. We also assume that while the populations in each location may change, the total population N must be conserved. Taking this into account, as

in Sec. 2.3.2, the resulting SIQRD meta-population model is given by,

$$\frac{dS_i}{dt} = -\frac{\beta I_i}{N_i} S_i + \sum_{j \in V} (\omega_{ji} S_j - \omega_{ij} S_i), \quad (4.10a)$$

$$\frac{dI_i}{dt} = \frac{\beta I_i}{N_i} S_i - \mu I_i - \alpha I_i - \kappa I_i + \sum_{j \in V} (\omega_{ji} I_j - \omega_{ij} I_i), \quad (4.10b)$$

$$\frac{dQ_i}{dt} = \kappa I_i - \mu Q_i - \alpha Q_i + \sum_{j \in V} (\omega_{ji} Q_j - \omega_{ij} Q_i), \quad (4.10c)$$

$$\frac{dR_i}{dt} = \mu I_i + \mu Q_i + \sum_{j \in V} (\omega_{ji} R_j - \omega_{ij} R_i), \quad (4.10d)$$

$$\frac{dD_i}{dt} = \alpha I_i + \alpha Q_i + \sum_{j \in V} (\omega_{ji} D_j - \omega_{ij} D_i), \quad (4.10e)$$

where the compartments $S_i(t)$, $I_i(t)$, $Q_i(t)$, $R_i(t)$, and $D_i(t)$, represent the number of individuals who are susceptible, infectious, quarantining, recovered or dead in vertex i at time t , respectively. This means we also have $S_i + I_i + Q_i + R_i + D_i = N_i$ for each vertex i . In all cases it is assumed that the travel rate from a vertex to itself, $\omega_{ii} = 0$, which intuitively makes sense as the travel rates only account for movement between vertices, also, as the network is modelled by a simple graph, self loops are not allowed. Also, the net number of individuals leaving/entering a vertex in the susceptible group only due to travel and not transmission/recovery/death, is given by the term $\sum_{j \in V} (\omega_{ji} S_j - \omega_{ij} S_i)$, similarly for the other compartments. The rate of travel in each compartment is assumed to be the same, i.e., the rate of travel is not dependent on the compartment, infected individuals travel just as much as susceptible.

The proposed modelling framework may account for travel as commuting patterns, that is, individuals return to their original location, details on the how this is achieved will be looked at in detail in Sec. 4.6. The distance travelled between locations often follows a power-law or heavy-tail distribution and can be described by a gravity or radiation population model [29, 30, 82, 174, 176, 177]. Thus the probabilities of movement between vertices according to these models can be used to determine the travel rates. Alternatively, empirical movement data can inform the model by using, for example, census data [36]. From these data sources one

can either build a static network or have the rates update depending on the time. Note that the proposed network model does not account for any importation from outside the considered network.

It is often the case that one wants the population of each location to have population remain constant, or at least be periodic over the course of a day. In the case of static travel rates, the only way to ensure that the population of each location remains the same for all time is to have the out travel rates equal to the in travel rates, i.e., $\omega_{ij} = \omega_{ji}$. This ensures that the same number of individuals that leave the vertex also enter it. Otherwise, the population of each vertex will tend towards a diffusive equilibrium given by the solutions of the balance $N_i^s/N_j^s = \omega_{ji}/\omega_{ij}$ [22], where N_i^s represents the population of vertex i in diffusive equilibrium. For travel rates which depend on time, one can have some periodic function, for example $\sin(2\pi t)$. This allows individuals to flow out of a vertex for half a day and then flow back into the vertex at the same (but negative) rates. This will be explored in Sec. 4.6.

Given this model, the next natural question is when does an epidemic occur and how do the quantities of the epidemic threshold as well as the herd immunity threshold change in comparison to the local well mixed model. It is clear that the addition of the travel terms as well as the multiple infected compartments I_i makes their computation significantly more difficult.

4.4 Reproduction Number

For the fully networked case [cf. Eqs. (4.10)], the basic reproduction number \mathcal{R}_0 can be computed from the system's next generation matrix \mathbf{G} [190]. This takes into account the couplings between the nodes when computing the stability of the disease-free equilibria. The entry, G_{ij} , of this matrix corresponds to the expected number of new infections in node i caused by an infected individual introduced in vertex j . In order to derive the next generation matrix, we start

with the *infection subsystem* of the original model, which is simply,

$$\frac{dI_i}{dt} = \frac{\beta I_i}{N_i} S_i - \mu I_i - \alpha I_i - \kappa I_i + \sum_{j \in V} (\omega_{ji} I_j - \omega_{ij} I_i). \quad (4.11)$$

This describes the evolution of all the infected compartments. Note that we don't consider Q an infected compartment as it cannot produce new infections. We now split the infection subsystem into two parts, the terms which produce new infections, and all other terms. Let U_i be the terms which contribute to new infections, thus we find,

$$U_i = \frac{\beta I_i}{N_i} S_i. \quad (4.12)$$

We let V_i denote the rate of movement to other compartments in vertex i not due to infection. This implies that,

$$V_i = -\mu I_i - \alpha I_i - \kappa I_i + \sum_{j \in V} (\omega_{ji} I_j - \omega_{ij} I_i). \quad (4.13)$$

By construction, it is clear that $I_i = U_i + V_i$.

We define two new matrices \mathbf{T} and $\mathbf{\Sigma}$ such that $\mathbf{T} = \text{Jac}(\mathbf{U})$ and $\mathbf{\Sigma} = \text{Jac}(\mathbf{V})$, where $\mathbf{U} = [U_1, \dots, U_M]^T$ and $\mathbf{V} = [V_1, \dots, V_M]^T$ and Jac refers to the Jacobian matrix. This gives rise to a linearised version of Eq.(4.11) at the point the Jacobians are evaluated at, i.e.,

$$\frac{d\mathbf{I}}{dt} = (\mathbf{T} + \mathbf{\Sigma})\mathbf{I} \quad (4.14)$$

where we let $\mathbf{I} = [I_1, I_2, \dots, I_M]^T$ denote the state vector of the infection subsystem. After computing the derivatives of \mathbf{T} and $\mathbf{\Sigma}$ we obtain the following,

$$T_{ij} = \delta_{ij} \frac{\beta S_i}{N_i}, \quad (4.15)$$

where δ_{ij} is the Kronecker delta function and thus, \mathbf{T} is a diagonal matrix. Similarly, we find,

$$\Sigma_{ij} = -\mu - \alpha - \kappa + \omega_{ji} - \delta_{ij} \sum_{k \in V} \omega_{ik}. \quad (4.16)$$

Writing these as matrix equations instead produces,

$$\mathbf{T} = \beta \text{diag}(\mathbf{S} \circ \mathbf{N}^{-1}), \quad (4.17)$$

where $\mathbf{S} = [S_1, \dots, S_M]^T$ and $\mathbf{N} = [N_1, \dots, N_M]^T$. The operator \circ , denotes the Hadamard (element wise) product and the inverse of \mathbf{N} is in relation to this operator. We also find,

$$\mathbf{\Sigma} = -(\mu + \alpha + \kappa)\mathbf{Id} + \mathbf{W}^T - \text{diag}(\mathbf{W}\mathbf{1}), \quad (4.18)$$

where \mathbf{W} is the weighted adjacency matrix of the network where $W_{ij} = \omega_{ij}$. Finally, following [190], the next generation matrix is given by

$$\mathbf{G} = -\mathbf{T}\mathbf{\Sigma}^{-1} = -\beta \text{diag}(\mathbf{S} \circ \mathbf{N}^{-1}) \left(-(\mu + \alpha + \kappa)\mathbf{Id} + \mathbf{W}^T - \text{diag}(\mathbf{W}\mathbf{1}) \right)^{-1}. \quad (4.19)$$

Then, the *effective reproduction number* \mathcal{R}_0^* for the networked system is given by the spectral radius ρ of the next generation matrix,

$$\mathcal{R}_0^* = \rho(\mathbf{G}). \quad (4.20)$$

That is, the largest eigenvalue by magnitude of the matrix \mathbf{G} . This provides a condition necessary for the stability all disease-free equilibria ($I_i = Q_i = 0, S_i + R_i + D_i = N_i$ for all $i \in V$). It also gives a natural definition for herd immunity in the network which we define as all states \mathbf{S} such that the reproduction number, $\mathcal{R}_0^* < 1$ (cf. the definition of herd immunity for the local dynamics in Sec. 4.2). This critical point of the effective reproduction number we refer to as the herd immunity threshold. All scenarios discussed in the next sections are simulated using our library for modelling epidemics on networks, EPIGRAPH [97], which is implemented in C++ and freely available on GITHUB.

4.5 Network Data

The travel network we consider combines the Republic of Ireland and Northern Ireland for a total of 3409 vertices. For the Republic of Ireland, it makes up 2992 of vertices in the network and they represent an *electoral division* as defined by the Central Statistics Office (CSO), for which small area population statistics are published from the 2016 census [58]. Similarly, for Northern Ireland, vertices refer to 417 *superoutput areas* which are administrative areas of a similar size as defined by the Northern Ireland Statistics and Research Agency (NISRA) [147]. In both cases the spatial resolution corresponds to the local administrative units below the category-3 regions of the Nomenclature of Territorial Units for Statistics (NUTS) [11]. The edges in network we take to be the travel rates from one vertex to another which will be computed in the next section. Due to the availability of detailed statistics on travel between EDs from the CSO, the construction of travel rates will be constructed from movements seen in the Republic of Ireland and Northern Ireland will be assumed to follow similar patterns.

The EDs and SOAs, which are the vertices in our network, can be seen in Fig. 4.3, coloured by their population density (population per km²). As evident from the figure, this gives us a relatively fine grained view of the islands population statistics. This is important for determining the rate of travel between vertices, which is heavily dependent on population size.

For example, take Fig. 4.4, this shows the number of travellers in and out of each vertex in the Republic of Ireland, compared to its population size. In the cases of both travellers into a vertex and out of a vertex, there is a clear linear relationship between the number of travellers entering/exiting. Although, the relationship in number of travellers into a vertex vs population of that vertex is not as clear as the case of travellers out, the relationship is still there.

Each of these EDs and SOAs belong to 1 of 32 counties on the Island. This alternative designation of areas is important, as often, in the case of the Republic of Ireland, decisions in the later stages of the COVID-19 pandemic, decisions were

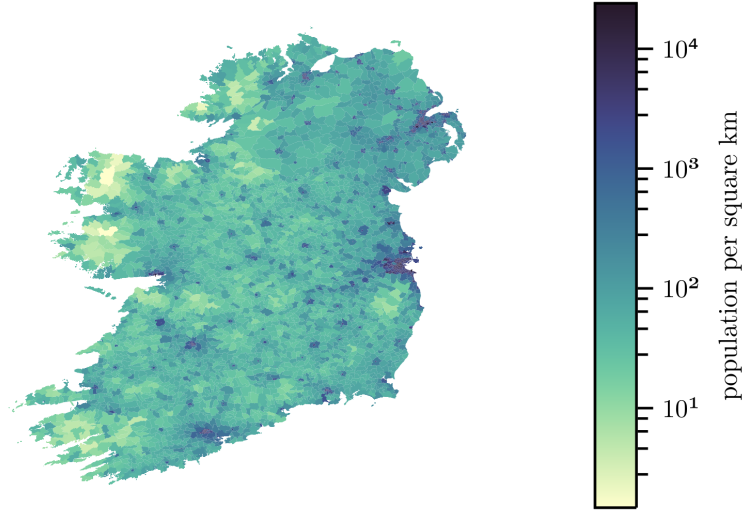


Figure 4.3: A plot of the EDs and SOAs administrative regions of the island of Ireland using the TM75 (EPSG:29903) projection. The colour of each area represents the number of population per km². Note that the color gradient is log₁₀ scaled.

made specific to these county regions. See Fig. 4.5 for a visual representation of the counties and their population density.

4.6 Mobility Model

In this section we discuss the mobility model used to generate the travel rates ω_{ij} , between vertices. As discussed in Sec. 2.4, when determining possible values for the travel rates ω_{ij} , much of the time empirical movement data is used [168]. However, unless there is much data available under enough varied conditions, the data can be difficult to use, especially during times in which the data is not a good representation of current travel trends (such as in government mandated travel restrictions). As empirical data only provides a snapshot into the behaviour of individuals movement patterns at a particular moment in time, it can be more useful to make use of mobility models which can react to changes in various scenarios for which the data is not available.

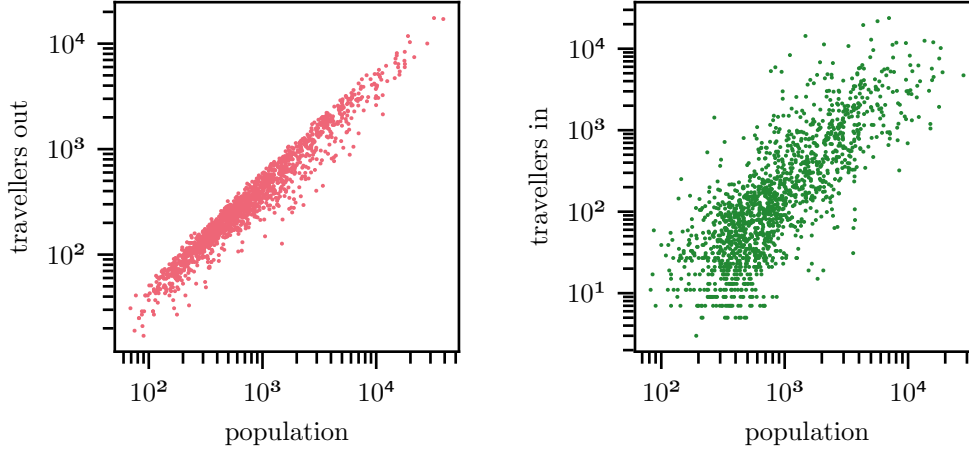


Figure 4.4: The plot on the left (red) shows the population of an ED against the number of individuals travelling out. The plot on the right (green) shows the population of an ED against the number of individuals travelling in. The data in both cases is from the 2016 census in the Republic of Ireland [36].

As we only have movement data available which was collected from a census questionnaire [36] we would face such difficulties. The census gives commuter flows between “Electoral Divisions”, these are the Republic of Ireland’s smallest administrative areas. Another drawback when using empirical movement data is that it can be difficult to amalgamate data from different sources. As we are attempting to model COVID-19 across the island of Ireland, we require data from various governing bodies which may differ in approach and availability of data. For example we don’t have the same level of commuting data in Northern Ireland as we do in the Republic of Ireland and we also do not have any data on cross border travel/commuting. Thus, we turn to the radiation model [129, 134, 174] which has seen much success in the last decade in terms of modelling human mobility.

We use the radiation model (as first discussed in Sec. 2.4) to generate the rate of commuting in the SIQRD contagion model. In the radiation model, the probability that a single traveller who leaves from i goes to j is given by,

$$q_{ij} = \frac{n_i n_j}{(n_i + s_{ij})(n_i + n_j + s_{ij})}, \quad (4.21)$$

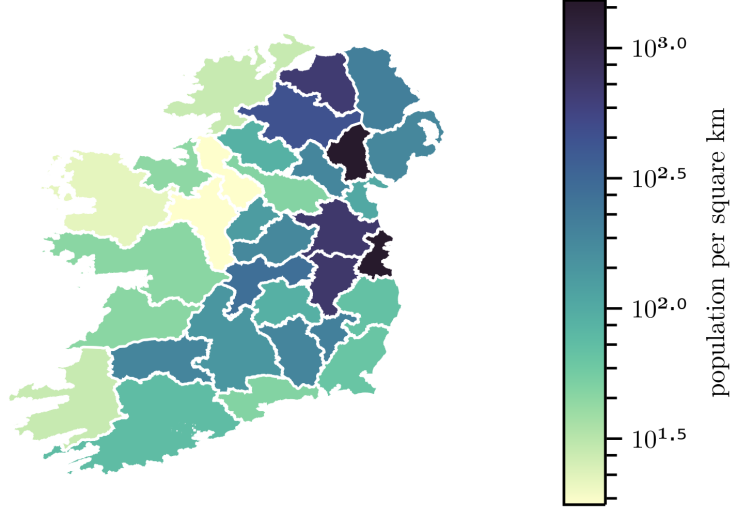


Figure 4.5: A plot of the counties of the island of Ireland using the TM75 (EPSG:29903) projection. The colour of each area represents the number of population per km^2 . Note that the color gradient is \log_{10} scaled.

where n_i is the population at vertex i and,

$$s_{ij} = \sum_{\substack{k; d_{ik} < d_{ij} \\ k \neq i \neq j}} n_k, \quad (4.22)$$

is the sum of all populations within a circle centered at i whose radius is the distance between i and j . d_{ij} is the distance between vertex i and j . The sum does not include the populations of i and j themselves.

Then we assume that the probability that an individual in vertex i decides to travel out on a given day and then chooses vertex j is given by,

$$u_i q_{ij} = u_i \frac{n_i n_j}{(n_i + s_{ij})(n_i + n_j + s_{ij})}, \quad (4.23)$$

where u_i is the probability that an individual in vertex i travels on a given day. We take this number u_i , to be average proportion of travellers out of an ED in the CSO [36] data. In Fig. 4.6 we see the distribution of the proportion of travellers out of vertices, with the green vertical line showing the average proportion to be 0.43, thus we take $u_i = 0.43$ for all $i \in V$. We assume that this value of the

average proportion of travellers out of a vertex also holds for Northern Ireland where we do not have the data available in the same level of detail.

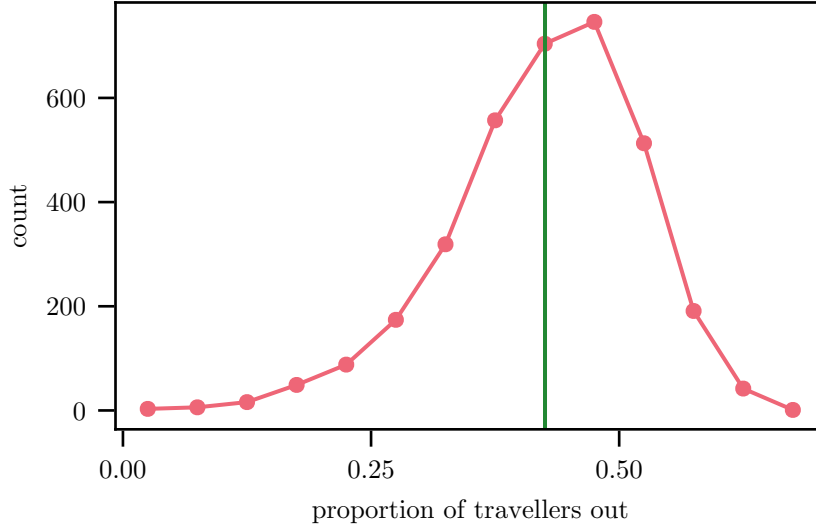


Figure 4.6: The distribution of the proportion of travellers out (red line) of all electoral divisions in the Republic of Ireland as reported from the 2016 census [36]. The vertical green line shows the average value on the horizontal axis of proportion of travellers out.

We can now test the performance of this model against empirical data. To do this we only consider the sub-network which consists of the Republic of Ireland. For each individual in every ED i , we randomly decide they travel *and* go to ED j according to Eq. (4.21). We then compare the generated travel distance distribution from our randomly assigned travellers to the empirical data in order to compare the performance of the radiation model. From Fig. 4.7, it is clear that the standard radiation model performs quite poorly (green line with triangle markers) when compared with the empirical distance distribution (red line with circle markers). It quite clearly overestimates the number of travels which occur below 10km and underestimates the number of travels which occur above that distance. There are a number of reasons why this might be the case, either the data we have is a poor representation of the true travel patterns in the country, or else the radiation model is that as universal as often assumed as shown in Refs. [6, 105]. These Generalised Radiation Models (GRMs) are better able to capture some of the underlying properties specific to the scale of the area as well

as properties such as difficulty of movement which would be higher in countries with less developed transport systems and road networks. However, GRMs come at the cost of parameters which require fitting, losing some of the advantage of gained over using a gravity model. We will look at a very simple extension to the gravity model, in line with the definition of GRM in Ref. [6] rather than Ref. [105]. We introduce 2 exponents to the model such that Eq. (4.23) becomes,

$$u_i q_{ij}^* = u_i \frac{n_i^{\gamma_1} n_j^{\gamma_2}}{(n_i^{\gamma_1} + s_{ij}^*)(n_i^{\gamma_1} + n_j^{\gamma_2} + s_{ij}^*)}. \quad (4.24)$$

This new quantity q_{ij}^* is the probability an individual travels to vertex j given they leave from i under the new GRM. The quantity s_{ij}^* is given by,

$$s_{ij}^* = \sum_{\substack{k; d_{ik} < d_{ij} \\ k \neq i \neq j}} n_k^{\gamma_2}. \quad (4.25)$$

We fit the two parameters, γ_1, γ_2 , using maximum likelihood estimation techniques. Specifically, using all pairs of home and destination travels, Γ , according to the 2016 census data, we maximise the quantity,

$$L(\gamma_1, \gamma_2) = \sum_{(i,j) \in \Gamma} \log(u_i q_{ij}^*). \quad (4.26)$$

Using the LBFGS algorithm to maximise the above, we found the parameters which best fit the data be $\gamma_1 = 1.456$ and $\gamma_2 = 0.748$, decreasing the effect of destination vertices and increasing the effect of home vertices. The value for u_i was taken to be the quantity 0.43 as discussed previously. In the same fashion as described above, we generate travels according to the new GRM with the best fit parameters and compare the generated distance distribution to the empirical distribution. The generated distance distribution can be seen in Fig. 4.7 as the blue line with square markers. When compared to the standard Radiation Model (RM) there is much better agreement between the data and the GRM, and so we use this model in generating the travel rates for the model.

As the quantity given above, $u_i q_{ij}^*$, is the probability of an event happening

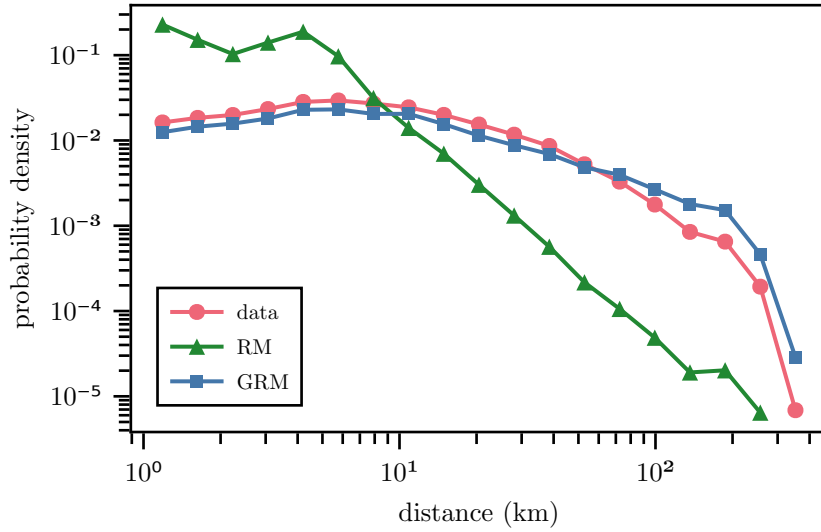


Figure 4.7: The distribution of travel distances in the Republic of Ireland as reported from the 2016 census [36] (red line with circle markers) as well as the RM (green line with triangle markers) and GRM (blue line with square markers).

over the course of day, we first need to convert that probability into a rate [66] in order to use it in our model and assign it to ω_{ij} . Assuming that the time between travel events is exponentially distributed, the rate of travel from vertex i to vertex j is given by,

$$\omega_{ij} = -\ln(1 - u_i q_{ij}^*). \quad (4.27)$$

This defines the average rate of travel out of a vertex. However, with a constant travel rate we run into the problem, as mentioned in Sec. 2.4, that the population of each vertex does not stay constant and heads towards a diffusive equilibrium. In order to prevent this from happening, we make our travel rates depend on time in a manner similar to Ref. [121], such that,

$$\omega_{ij}(t) = -\frac{\pi}{2} \sin(2\pi t) \ln(1 - u_i q_{ij}^*). \quad (4.28)$$

This new travel rate has a period of 1 day with the travel rates turning negative in the second half of the day. As the function is odd about all times $t = k + \frac{1}{2}$ for $k \in \mathbb{N}$, it ensures that the same number of travellers that leave a vertex in a given day return by the end of day. The reason for the $\frac{\pi}{2}$ coefficient is that it implies the

average rate of travel in the time intervals $(k, k + \frac{1}{2})$ is exactly $-\ln(1 - u_i q_{ij}^*)$ and in the time intervals $(k + \frac{1}{2}, k + 1)$, it is exactly $\ln(1 - u_i q_{ij}^*)$ (note the difference in signs), in both intervals, $k \in \mathbb{N}$. The intuition behind the form of our temporal travel rates is to roughly approximate the daily commuting flow of individuals in the network.

4.7 Case study: Ireland

For the remainder of this chapter, we elaborate on the spreading of COVID-19 in Ireland as a case study, under the assumption of no viable vaccine. The network model given by Eqs. (4.10) is informed by publicly available data detailed in the next section.

4.7.1 First Wave of COVID-19

In order to demonstrate the general feasibility of the proposed modelling framework, we attempt to model the first outbreak of COVID-19 on the island of Ireland. However, due to the difference in approaches between the Irish and UK government, with restrictions coming into effect and lifting at different times, we make the assumption that Northern Ireland has the same restrictions as the Republic of Ireland and shares the number of infections and deaths for the sake of fitting the model.

After the initial outbreak and first restriction of initial movements (lock-down), the plan for reopening the Republic of Ireland was first published in May 2020 as the 5-phase *roadmap for reopening society & business* for reducing lock-down restrictions as outlined by the Irish Government in May 2020 [162]. However, as was seen, the roadmap had to be continuously changed and adapted as new information became available and the effectiveness of lock-down efforts became known. Of the first 5 phases of reopening outlined by the government, the first 3 were followed according to the original plan without alteration [149].

CHAPTER 4. A META-POPULATION MODEL FOR THE SPREAD OF SARS-COV-2

This saw the number of infected in the country fall to almost 0 detected cases. Thus we consider the first *wave* of COVID-19 as the date of first infection to the end of phase 3. See Fig. 4.9. Prior to the reopening phases, two important dates in the first wave of COVID-19 are the dates during which schools first closed and the issue to work from home and restrict movement. These dates, along with the dates the reopening phases became active, and a broad outline of the restrictions associated with them are given in Tab. 4.1.

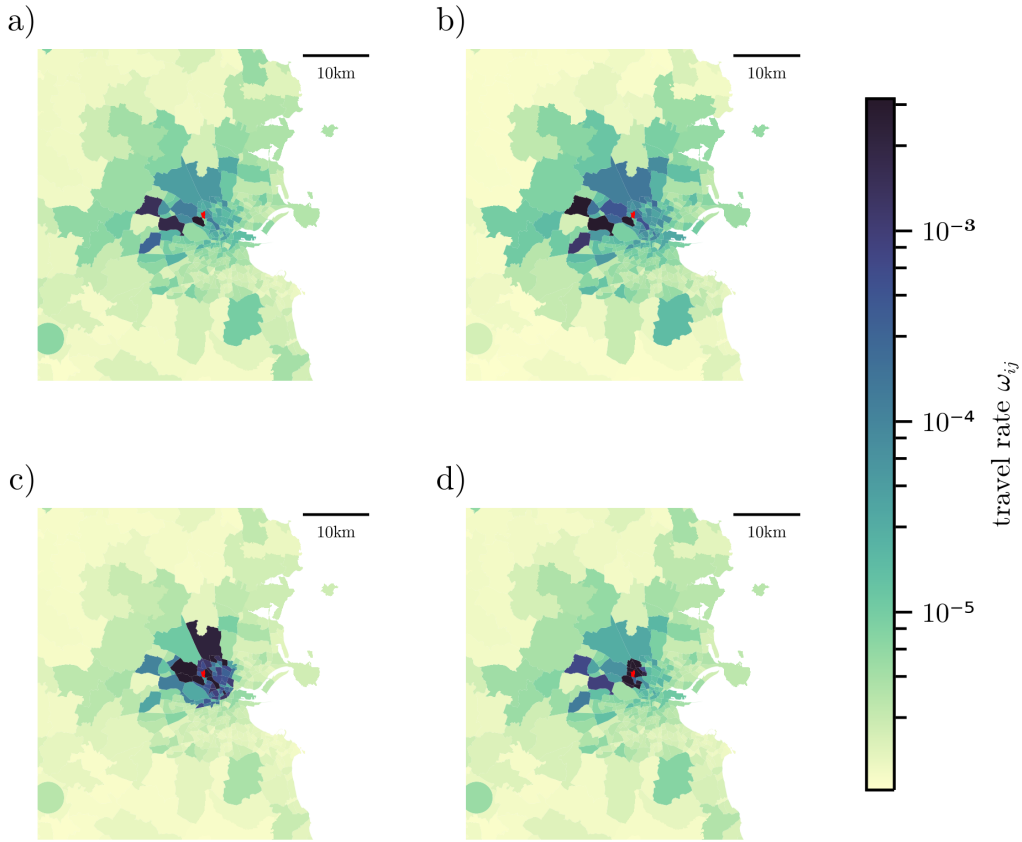


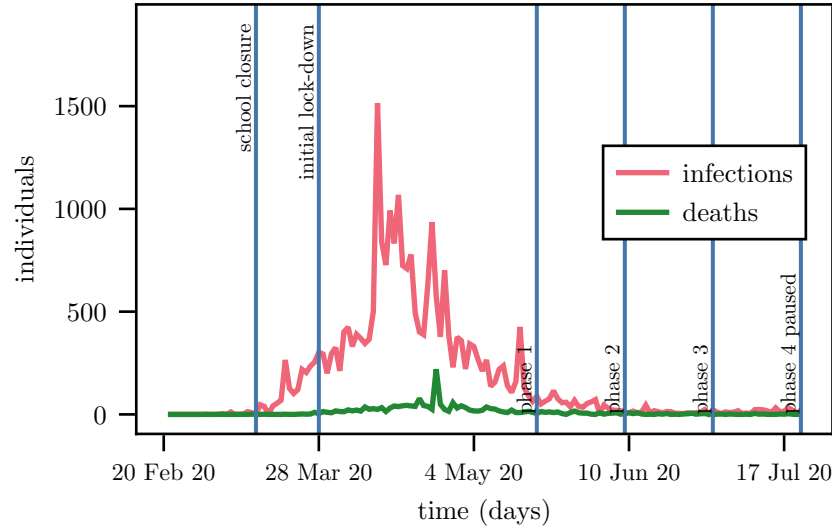
Figure 4.8: A visual representation of the journeys out of a particular electoral division in the Dublin area (red area) to surrounding electoral divisions with different restrictions in place with a compliance of 70%. Labels (a), (b), (c), and (d) correspond to travel restrictions of none, 20km, 5km, and 2km, respectively.

The effect of the movement restrictions on the travel rates as defined in Sec. 4.6 can be seen in Fig. 4.8 which depicts the travels out of a particular area (here an electoral division in Dublin; red area) are affected by the different travel re-

Table 4.1: Travel and gathering restrictions during the first wave of the COVID-19 outbreak. Restriction come into effect on the given date of the event.

Event	Date	Max Distance	Social distancing
school closure	12-03-20	no restrictions	recommended reduction
initial lockdown	27-03-20	2km	essential meetings only
phase 1	18-05-20	5km	essential meetings only
phase 2	08-06-20	20km	maximum of 4 people
phase 3	29-06-20	no restrictions	maximum of 4 people
phase 4 paused	20-07-20	no restrictions	small gatherings

strictions as given in Tab. 4.1. As the travel radius is reduced, the movement is confined to a more local vicinity. Note that travel beyond the travel radius is still present due to non-compliance. Specifically, the rate of travel between locations which are outside of the allowed travel radius are scaled by 1 minus the compliance factor, which we take to be 0.7. This level of compliance is supported by findings of a nation-wide series of phone interviews accounting for essential/justified and non-essential travel [108].

**Figure 4.9:** The number of new daily recorded infections (red) and deaths (green) in the Republic of Ireland during the year 2020 as published by Ordinance Survey Ireland [47]. The vertical lines indicate when a new phase with associated restrictions in being entered.

Our model attempts to follow the historic evolution of the disease during

the first wave of the outbreak. In order to fit our model to the data, we assume reasonable parameters for the SIQRD model, with β being the only free parameter we fit against. That is, the rate of contact multiplied by probability of infection on contact. We allow β to take on a different value for the duration of each of the phases listed in Tab. 4.1.

When fitting to the reported deaths [47], we let the initial condition of the model be a very small quantity of infected individuals (0.01) added among locations. We then integrate the model and fit the model deaths to the number of actual deaths, shifted by back 20 days, by means of least squares. Looking at Fig. 4.10, we see the total number over time of deaths across all vertices in the network (red line), with the reported deaths (green dashed line), with a 20 day backwards shift, plotted over the model deaths. We denote the total number of deaths across all vertices in the network as $D(t) = \sum_{i \in V} D_i(t)$ and similarly for all other compartments. Comparing the two curves, we see reasonable fit to the deaths is achieved.

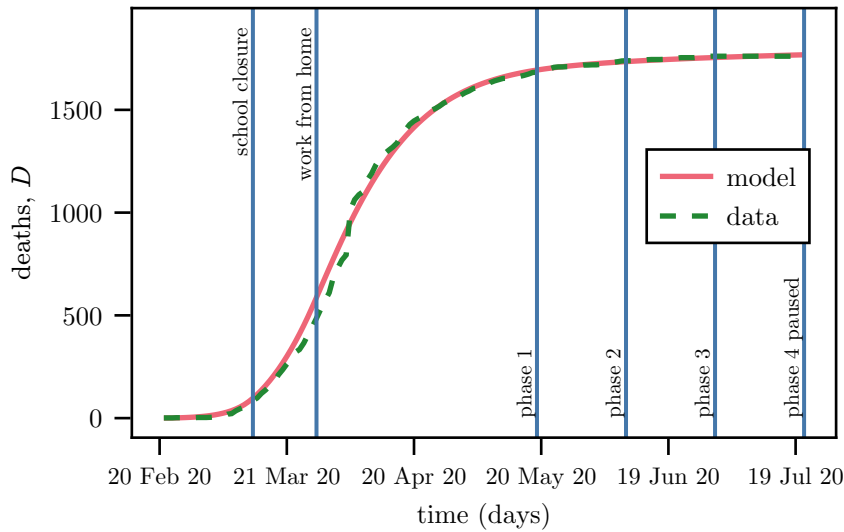


Figure 4.10: The cumulative number of deaths in the Republic of Ireland shifted back 20 days (red solid line) during the year 2020 as published by Ordinance Survey Ireland [47] and the cumulative deaths according to the SIQRD model (green dashed line) using the parameters given in Tab. 4.2. The vertical lines indicate when a new phase with associated restrictions in being entered.

Using deaths to fit the model gives the best chance at producing realistic

parameters for the model, the reason being that the recorded number of deaths is far likely to be closer to the true value than the recorded infections. The reason for fitting to the deaths with a 20 day delay is due to the fact that the data which reports daily deaths in Fig. 4.9 is the date the death is reported rather than date of actual death, this lag in reporting can vary quite a bit, with a median time to report of 18 days and mean of 63 days as reported by the CSO [101]. With this in mind we tested fitting the model against deaths with delays ranging from 1–30 days and found 20 days to give the best fit. For the parameters, we assume that the average time before recovery or death is 10 days, with a proportion of 0.03 of all cases ending in death [34, 133]. Hence we choose $\mu = 0.97/10$ and $\alpha = 0.03/10$. We assume that the average time before quarantining is 2.5 days, hence we choose $\kappa = 1/2.5$, we do not have as strong an argument for this value of κ other than it seems to be a reasonable assumption and was used in Ref. [5]. See Tab. 4.2 for a list of the parameters for each stage of the first wave of the infection, including the fitted values for β .

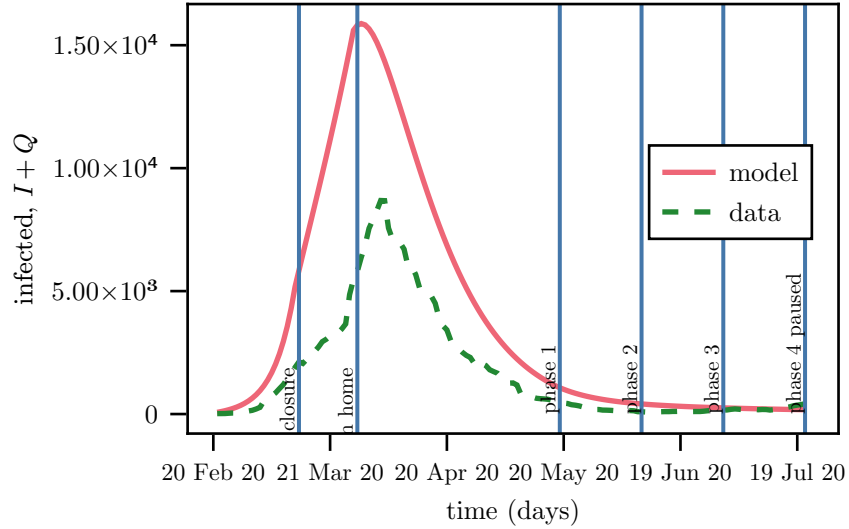


Figure 4.11: The 10 day incidence rate of infections in the Republic of Ireland shifted back 8 days (red solid line) during the year 2020 as published by Ordinance Survey Ireland [47] and the total number of infected across the entire network ($I + Q$) according SIQRD model (green dashed line) using the parameters given in Tab. 4.2. The vertical lines indicate when a new phase with associated restrictions in being entered.

Now, using the β parameters from each phase from fitting the number of

CHAPTER 4. A META-POPULATION MODEL FOR THE SPREAD OF SARS-COV-2

Table 4.2: Parameters used to model the first wave of COVID-19 in Ireland during the events given in Tab. 4.1. \mathcal{R}_0 is computed from the system parameters.

Event	β	μ	κ	α	\mathcal{R}_0
pre restrictions	0.69	0.097	0.4	0.003	1.38
school closure	0.55	0.097	0.4	0.003	1.1
initial lock-down	0.43	0.097	0.4	0.003	0.86
phase 1	0.49	0.097	0.4	0.003	0.98
phase 2	0.49	0.097	0.4	0.003	0.98
phase 3	0.49	0.097	0.4	0.003	0.98

deaths, we can check how well the model compares to the reported number of infections [47]. We do at expect quite as good a fit as with the number of deaths, as the number of reported infections is heavily dependent on the rate of testing over time which was known to be highly variable [49]. In Fig. 4.11, we see the total number of infected according to our model, $I+Q$, as the red line and the 10 day (the same as our assumed average time to recovery or death) incidence rate of the reported infections as the dashed green line. Similar to the deaths, we shift the 10 day incidence rate back by 8 days. This is to account for the average 6 day lag between contracting the disease and becoming infectious [59] (which our model does not account for), as well as the reported expected time for reporting positive results of PCR tests of 2 days. We see that our model gives a higher number of infected compared to the reported figures, however, we see that the curves follow the same patterns with their peaks lining up. It is expected that the model produces a higher number of infected as the reported number of infections only gives the number of infected within the small testing pool of individuals and will not capture asymptomatic individuals or those who self isolate without being tested.

Now, we run the model using the fitted parameters to simulate the first wave, we then allow the model to return to pre-lock-down conditions with no restrictions on movement or gatherings, with the parameters returning to the pre-restriction state as in Tab. 4.2. It is important to note that at this stage, we do not consider any reintroduction or roll back to earlier phases during the course of the simulated outbreak. This corresponds to a worst-case scenario (which is how we shall refer to this scenario), should the island have not have introduced any subsequent

lock-downs in the presence of rising infections and deaths.

As defined in Eq. (4.7), the basic reproduction number of the local dynamics [cf. Eqs. (4.1)] only exceeds the critical value of $\mathcal{R}_0 = 1$ during pre lock-down and school closure. Conversely, initial lock-down, phases 1, 2 and 3 have a \mathcal{R}_0 value below unity and – neglecting network-related effects – exhibit a burn out of an outbreak and self-guided decrease of the number of infected.

We introduce a very small number of infected individuals to every vertex in the network (0.01 individuals), on 20th February, 2020, that is, 21 days before the school closure date, and run the model such that the disease spreads naturally and without control. On the 12th March, we introduce the initial lock-down measures, which take some time to reach full effect. Individuals’ movement is limited to 2km and this is adhered to with 70% compliance, as discussed previously. The level of compliance to movement restrictions is kept constant at 70% in the simulations. In Sec. 4.7.2 we will investigate the effect of different levels of compliance with restrictions in the context of lock-down restrictions that are location dependent (cf. Fig. 4.20).

We account for social distancing by reducing the rate of mixing within communities, this is accounted for with the parameter β (cf. Tab. 4.2 for the respective parameter values). During phases 1 and 2, the travel radius increased to 5km and 20km, respectively, and we assume the same level of compliance. Travel restrictions are removed in phase 3 (cf. Tab. 4.1). Each of the numbered phases have a duration of 21 days.

Fig. 4.12 depicts the time series of all five compartments – aggregated over all vertices. In the network case of the SIQRD model, we denote the sum of the total number of individuals in each vertex belonging to compartment S as $S(t) = \sum_{i \in V} S_i(t)$, and similarly for the other compartments. The S, I, Q, R and D compartments are given by the red, green, blue, yellow and cyan coloured curves respectively. The number of individuals is shown on a \log_{10} scale and the grey vertical lines show when the various events given in Tabs. 4.1 and 4.2 begin, and thus what restrictions are in place and what parameters are in use. For the

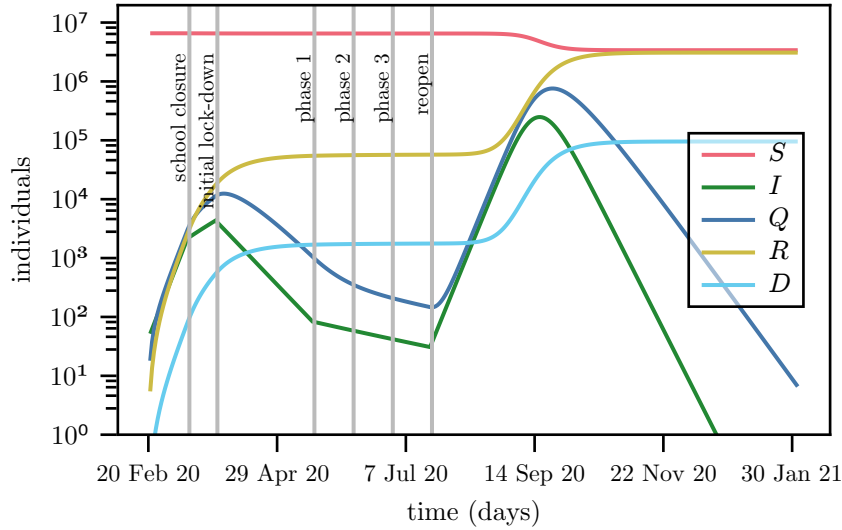


Figure 4.12: Total number of individuals in the worst-case scenario across the entire network belonging to each compartment, as stated in the legend, over time with a \log_{10} scale on the y-axis. Parameters as in Tab. 4.2 and a 70% compliance to movement restrictions. The beginning of each successive event is indicated by the grey labeled vertical lines in the plot. After the initial wave (post phase 3), the parameters are set back to that of the pre lock-down values.

reopening phase, the parameters and restrictions are assumed to be the same as that of the pre-restriction phase.

One can see two distinct peaks: (i) a small peak that occurs before the lock-down and (ii) a second peak that occurs once all lock-down measures are lifted. It is clear that unless some of the measure are maintained, then the lock-down will just have the effect of delaying the epidemic and result in a second wave with a prevalence that – in this unlikely worst-case scenario – is 100 times higher than the first one and exceeds any realistic capacity of the health-care system. The number of infected eventually reaches zero due to a depletion of the pool of susceptibles.

Following the geometric analysis of the local dynamics (cf. Sec. 4.2), the trajectory lands at one of disease-free equilibria $I_e = 0$. A change in parameters, e.g., rate of contact time probability of infection on contact, β , or a rescaling of the population to the number of remaining susceptibles can render this state unstable

again. Then, a perturbation to the networked system, for instance, introduction or importation from outside, has the potential to trigger an additional outbreak.

For the simulation run given in Fig. 4.12 we compute the next generation matrix as in Eq. (4.19) at each day and find its spectral radius giving rise to the network's effective reproduction number \mathcal{R}_0^* . That is, the expected number of infections generated by a single infected individual for the given number of susceptible individuals in each vertex. This is in comparison to the basic reproduction number, \mathcal{R}_0 , which is the expected number of infected individuals generated by a single infected individual in the basic DFE, the values for which are given in Tab. 4.2. The time evolution of \mathcal{R}_0^* is plotted as black dashed curve in Fig. 4.13.

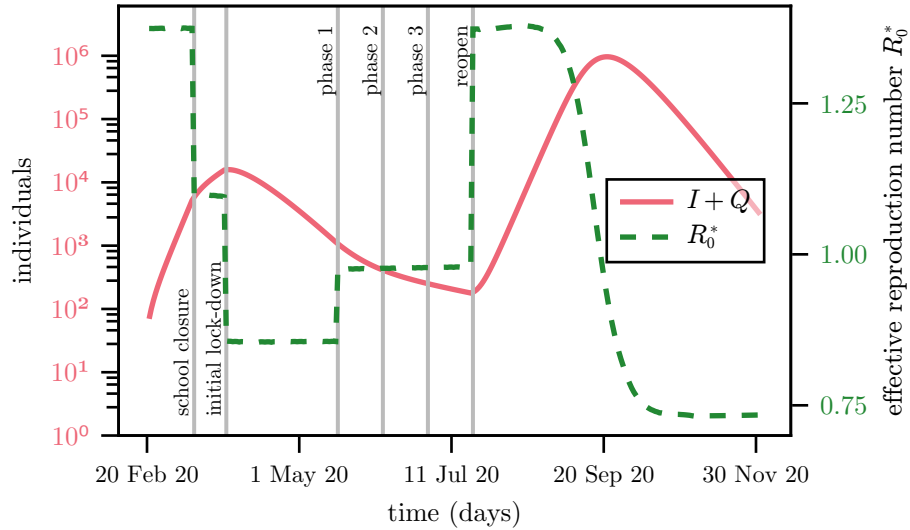


Figure 4.13: The effective reproduction numbers \mathcal{R}_0^* (green dashed, values on right y-axis) over time as calculated from the basic reproduction number and spectral radius of the next generation matrix given by Eq. (4.19), respectively, together with the number of infected and quarantining (red solid, values on left y-axis) in the network in the doomsday scenario as shown in Fig. 4.12.

The value of \mathcal{R}_0^* shows the potential for the disease to spread at each phase in the simulation. From Fig. 4.13 we can see clearly that when \mathcal{R}_0^* falls below unity, the number of infected also begins to fall. We also note the point of herd immunity is reached is in when the number of susceptibles crossed the point where the \mathcal{R}_0^* goes below 1 in the final reopen phase which has no restrictions.

As stated above, the parameters are chosen to match the actual number of deaths in the Republic of Ireland. See Figs. 4.10 and 4.11 for a detailed comparison to reported data. The simulated results, however, are not meant to reflect this range of confirmed cases, but following the logic of the model, refer to all infected individuals including asymptomatic, non-diagnosed and untested.

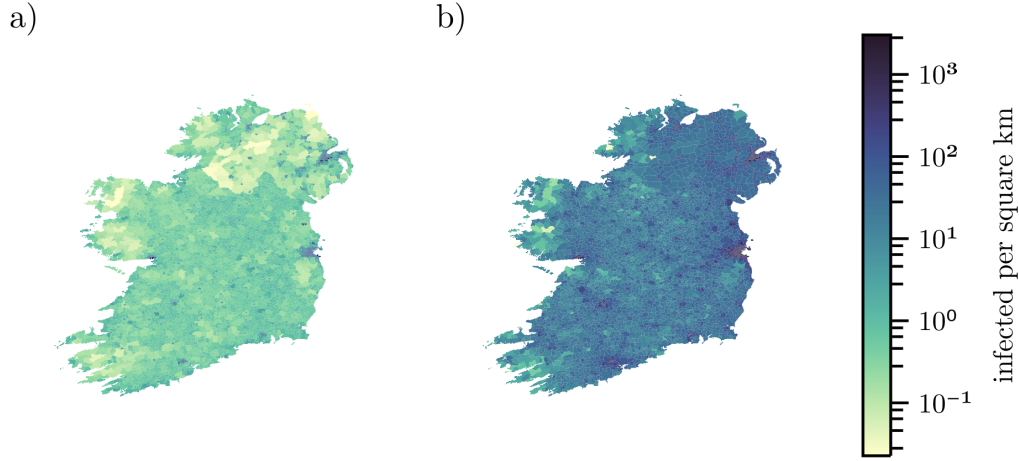


Figure 4.14: The spatial distribution of infected individuals per km^2 around the two distinct peaks shown in Fig. 4.12 at (a) 26th March 2020 (b) 17th September 2020. Parameters as in Tab. 4.2.

Figure 4.14 shows spatially resolved snapshots of the prevalence of the disease per km^2 on March 26th 2020 and 17th September 2020 respectively (cf. Ref. [103] for a map based on data of reported, confirmed cases) according to the SIQRD model simulation in Fig. 4.12. Fig 4.14 (a) corresponds to the disease prevalence at the first peak before the lock-down. The disease remains in the East of the country for the most part with the exception of big towns and cities. In contrast, on 17th September 2020, see Fig 4.14 (b), the outbreak covers the entire country and affects every electoral division. So far in our model we have assumed that after leaving the phase 3 reopening, the parameters return to their values pre-pandemic, which is an unlikely scenario and was not seen after the initial outbreak of COVID-19, which saw that individuals were far more careful with taking preventative measure such as social distancing and wearing face masks [108].

We investigate the degree to which the effect of the preventative measures

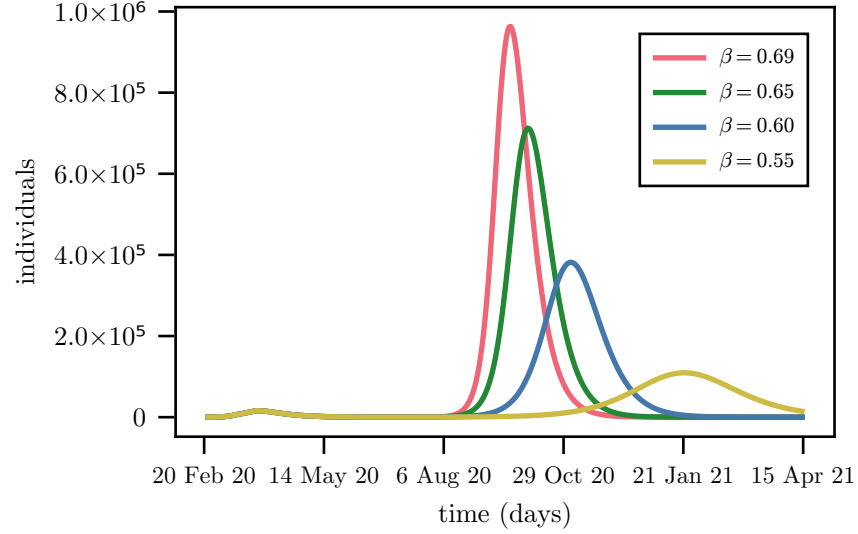


Figure 4.15: Evolution of the combined infected and quarantined compartments $I + Q$, aggregated over the entire network for varied post-lock-down conditions. The red curve corresponds to the parameters given in Tab. 4.2 (cf. Fig. 4.12). The other curves vary the parameter β in the post-lock-down phase as stated in the legend: $\beta = 0.65$, $\beta = 0.6$ and $\beta = 0.55$. Other parameters are as given in Tab. 4.2.

mentioned above have on reducing the size of the peak in the so called worst-case scenario as modelled in Fig. 4.12. As shown in Fig. 4.15, we model the effect of different levels contact rates by varying the parameter β during the final lifting of restrictions after phase 3. The plots depict the time series of the aggregated infected and quarantined compartments $I + Q$. A reduction to 0.55 from the original rate of contact times probability of infection, i.e., β , leads to a significantly smaller and delayed second peak (yellow curve), while the basic reproduction number of the local dynamics remains above unity (cf. Tab. 4.2). This value for β is the same as the fitted value during the school closure phase, indicating that a consistent low level lock-down, although with a basic reproduction number greater than 1, could be a means to reach herd immunity while keeping the peak of infections relatively low. However, this peak of hundreds of thousands of infected is still likely to overburden the island’s healthcare capacity.

We now investigate the effect of the heavy-tail distribution of travel across the network and whether or not it causes a lack of sensitivity in initial conditions. We run the model for a number of random initial seeds under a no lock-down

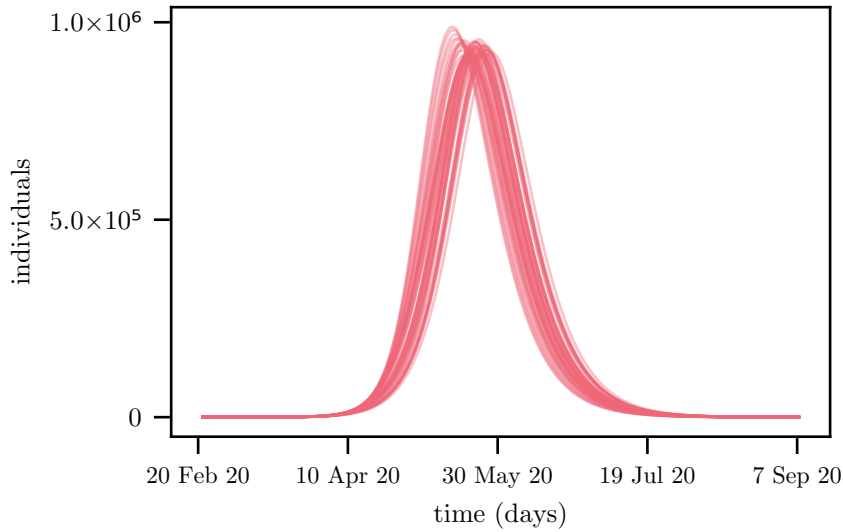


Figure 4.16: Time series of the sum of the combined I and Q compartments over the entire network for 50 random initial locations under a no lock-down scenario, that is, the parameters used for the entire simulation are those listed under pre lock-down in Tab. 4.2. For each scenario, the initial location started with a single individual.

scenario (see Fig. 4.16) where for each run only a single individual is placed in one ED or SOA at the start of the simulation. The resulting time series are shown in Fig. 4.16.

One can see that the timing of the peaks are all within ~ 1 week of each other and their amplitudes are near identical. In the presented 50 cases, the initial location is selected uniformly at random from all network vertices. We note that deliberately selecting urban or rural locations appears to have little qualitative impact. While there are definite differences in amplitude and timing of the peaks due to initial conditions, they qualitatively all behave quite similar, thus showing a large degree of insensitivity to initial conditions.

4.7.2 Dynamic Interventions

In this section, we discuss the scenario of a flexible lock-down policy as was seen in use globally, including in the republic of Ireland [149]. The policy monitors the

prevalence of the disease within the island and aims to keep it below the capacity of the health-care system. There are 2 policies which we consider, they are i) Island Interventions and ii) Regional interventions. The island intervention policy considers some threshold, I_{th} , as the maximum number of infected throughout the entire island that can be present before an all island lock-down is triggered. Whereas, the regional intervention policy considers some threshold, I_{th}^c , as the maximum number of infected permitted in each county (cf. Fig. 4.5). Any county which surpasses this threshold goes into a lock-down scenario independent of the other counties.

Such a procedure corresponds to dynamic [39, 113, 115] or active [9] interventions. In both policies, we simulate until phase 3 as before to maintain the agreement with reported deaths. Afterwards, if the conditions for lock-down are met, the island/county goes back an into initial lock-down and then progresses from there through phases 1 – 3, until the condition is met again.

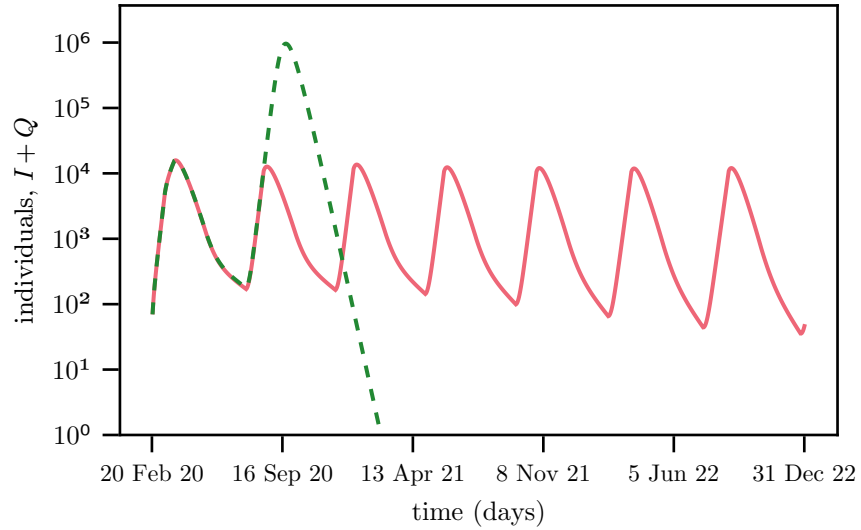


Figure 4.17: The number of individuals, aggregated over the entire network, belonging to the combined I and Q compartments over time (using the parameters in Tab. 4.2) under a dynamic lock-down strategy taking $I_{th} = 10^4$. The model simulates the historic events up to phase 3 before implementing the island wide dynamic lock-down process. The dashed line shows the equivalent model without the dynamic lock-down strategy shown in Fig. 4.12.

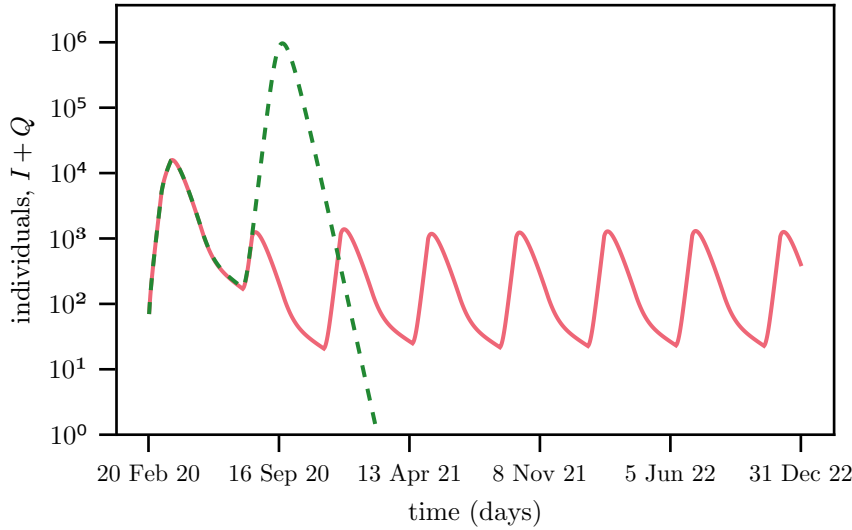


Figure 4.18: The number of individuals, aggregated over the entire network, belonging to the combined I and Q compartments over time (using the parameters in Tab. 4.2) under a dynamic lock-down strategy taking $I_{th} = 10^3$. The model simulates the historic events up to phase 3 before implementing the island wide dynamic lock-down process. The dashed line shows the equivalent model without the dynamic lock-down strategy shown in Fig. 4.12.

Island Interventions. In detail, we consider two scenarios with different threshold parameters, which are inspired by the reported, maximum number of hospitalized cases during the first wave in April 2020 [103]: (i) $I_{th} = 10^4$, as shown in Fig. 4.17 and (ii) $I_{th} = 10^3$ as depicted in Fig. 4.18. In both figures, the worst-case scenario of Fig. 4.12 is added as dashed curves. For the case of $I_{th} = 10^4$, the number of susceptible individual left is approximately 6.3×10^6 out of the starting 6.6×10^6 , and thus, is far below the required level for herd immunity to take effect.

Under the assumptions of the considered network model, it would take many years for a significant depletion of the pool of susceptibles. From Eq. 4.8, we find the herd immunity threshold, given the parameters in pre-lock-down phase of Tab. 4.2, to be approximately 4.5×10^6 susceptible individuals. Extrapolating from Fig. 4.17, we see that approximately 3×10^5 individuals recover over a period of 1 year and 9 months, or 1.6×10^5 per year. Assuming this rate of depletion from the susceptible population is maintained over the entire course of

the pandemic (which it would certainly not be, it does however give us an upper bound), it would take approximately 28 years for the number of susceptibles to reach the herd immunity threshold. By the same reasoning, this would lead to a total number of approximately 1.4×10^5 deaths over the course of many waves. Even with a large threshold $I_{\text{th}} = 10^4$ for the maximum number of infected cases, the feasibility of such a strategy is questionable due to the time it would take to reach herd immunity of on the island.

The re-introduction of lock-down measures to account for rising numbers of infected can change the stability of the disease-free equilibria $I_e = 0$. However, as soon as the restrictions are relaxed, e.g., after phase 3, an unstable family of these equilibria re-emerges and the outbreak pattern repeats. Suppressing the occurrence of unstable disease-free equilibria requires other forms of interventions. One could consider, for example, a fishing-type extension of the model [8, 24, 40]. This will basically turn the rate κ in the local dynamics (4.1) into a function of the number of infected, e.g., $\kappa(I) = \frac{h}{1+I/I_c}$ with a consumption/fishing rate h (here: rate of isolation) and a reference capacity I_c for $\kappa(I) = h/2$. This I dependence will account for contact-tracing effects, which are especially effective for low numbers of infected. As a consequence, a high rate h of isolation will be able to push the basic reproduction number [cf. Eq. (4.7) or Eq. (4.20)] below the critical value of $\mathcal{R}_0^* = 1$ and change the stability of the equilibria $I_e = 0$.

Regional Interventions. Next, we consider another scenario that accounts for regional lock-downs at the level of counties. In our dynamic intervention model this corresponds to each county having its own I_{th}^c , that is, the threshold of infected individuals belonging to the sum of the I and Q compartments in each county. Thus, once the county surpasses this threshold, another lock-down is triggered sending the county back to the initial lock-down as listed in Tab. 4.2, after which the county progresses through the various phases 1 – 3, before reopening and assuming the parameters of the pre-lock-down state. This entering and lifting lock-down is repeated ad infinitum. When lock-down phases differ between counties, we assume that the travel restrictions in and out are followed with the compliance of the county being travelled to. When we run the simulations using

the regional interventions, the model operates at the level of ED and SOA but their travel and interaction dynamics are consistent across counties. The parameters used for each phase are the same as those given in Tabs. 4.1 and 4.2. For this run we took the maximum number of infected per county $I_{th}^c = 1400$ and again, the model is allowed to run without intervention until phase 3 to match the historic number of deaths.

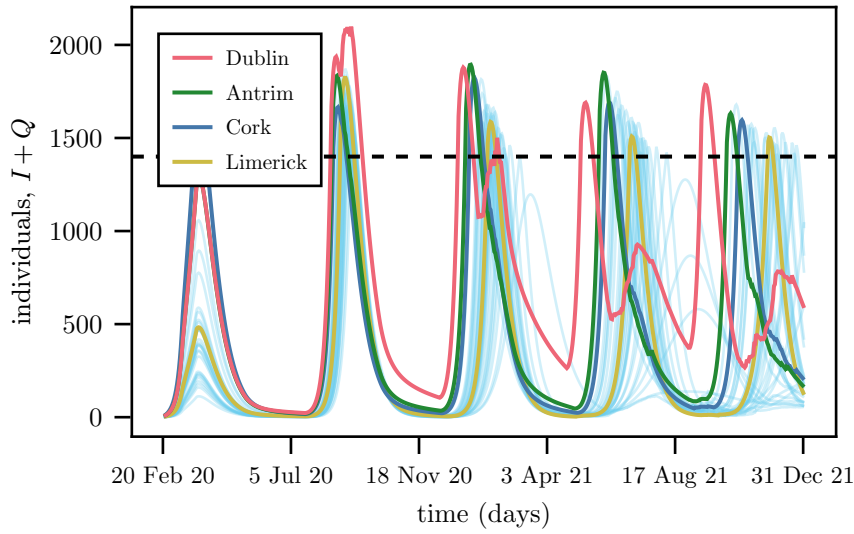


Figure 4.19: Total number of individuals (aggregated over counties) belonging to the sum of the I and Q compartments. Parameters as in Tab. 4.2. The simulation follows the historic events up to phase 3 as before after which the dynamic county lock-down strategy is used and the total number of infected in each county becomes desynchronised. The four counties with the largest cites in the island are explicitly denoted in the legend. Every other county is shown as a transparent cyan line. The threshold quantity used was $I_{th}^c = 1400$, and is shown as a black horizontal dashed line.

From Fig. 4.19 we see some interesting dynamics when we view the evolution of the number of infected in each county. Each time after Dublin re-enters lock-down due to dynamic lock-down, after only a few days to weeks the numbers start rising again. This is not due to its own dynamics, but due to its interaction with neighbouring counties, which are either not yet in lock-down, or have a high number of infected and are still travelling, though at far reduced rates, due to a level of non compliance with restrictions.

It can be seen that the secondary peaks in Dublin, when it is in lock-down, lines up with the bulk of peaks in the cyan curves. It is only once all the other

counties enter lock-down do we see the numbers in Dublin begin to drop. We conclude that treating such counties in isolation is not a good strategy due the strong coupling between each county that is not eliminated when some counties remain free to travel even only within their own borders.

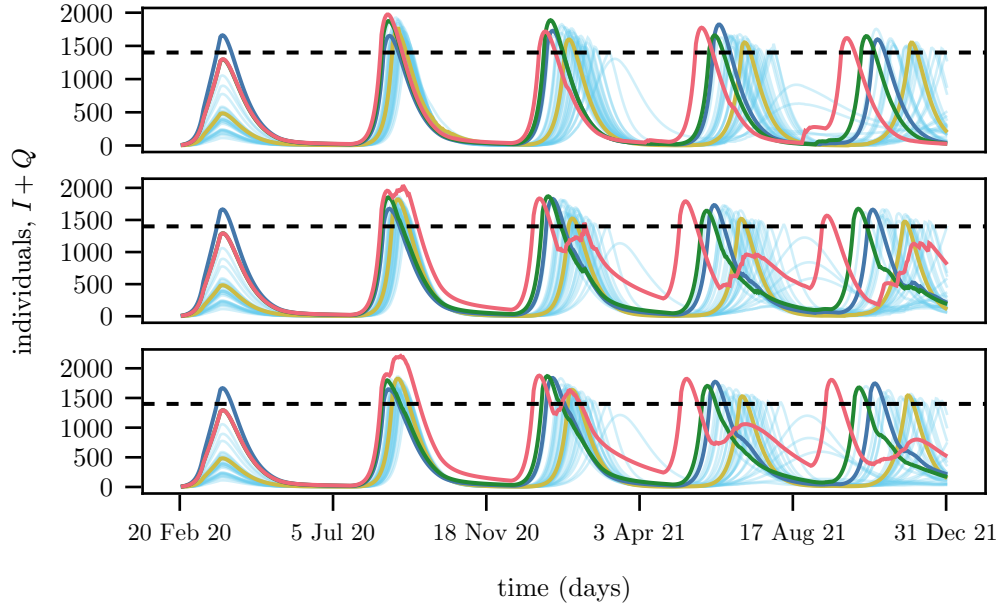


Figure 4.20: Number of individuals (aggregated over counties) belonging to the combined $I+Q$ compartments for compliance of 100% (top), 90% (middle) and 0% (bottom). The colours of the curves are the same as that in the legend of Fig. 4.19. Other parameters as in Tab. 4.2. The simulation follows the historic events up to phase 3 as before, after which, the dynamic county lock-down strategy is used and the total number of infected in each county becomes desynchronised. The threshold quantity used was $I_{th}^c = 1400$, and is shown as a black horizontal dashed line.

Next, we investigate the impact of compliance to movement restrictions. Previously, we considered a compliance level of 70%, as such, we now look at the two extreme value of compliance as well as close to full compliance in order to compare the effects of the 70% compliance, that is, we consider 0%, 90%, and 100% compliance. Fig. 4.20 depicts the evolution of the disease using a dynamic county lock-down strategy as in Fig. 4.19, but using 100% compliance in the top panel, 90% in the middle panel and 0% in the bottom panel. As previously, the model is run to match the historic deaths up until phase 3. The rest of the parameters used in each simulation are the same.

One can see that even with 0% compliance (bottom plot of Fig. 4.20), the secondary peaks that occur in Dublin (the peaks that line up with the bulk of the cyan curves) due to travel from outside the county are very similar to the equivalent simulation using 70% (cf. Fig. 4.19) as well as 90% (cf. middle panel of Fig. 4.20). Only in the plot with 100% compliance (cf. top panel of Fig. 4.20), do we see the lack of large secondary peaks that keep the number of infected in Dublin above the threshold level of $I_{\text{th}}^c = 1400$, or else bring it back beyond that level. And so, we conclude that unless near 100% percent compliance with travel restrictions is observed, the effect of a county level dynamic lock-down strategy will not have the desired effect as Dublin will be greatly effected by the lock-down status of the rest of the island's lock-down status. Thus, an alternative strategy could be to consider a lock-down strategy which considers restrictions in only Dublin and the rest of the island.

4.8 Summary

We have proposed a dynamical network model to study the spreading of SARS-CoV-2 that accounts for travel or commuting between vertices of a network. As a case study, we have presented results from numerical simulations for Ireland, where the model is informed from publicly available data on geographical regions, population, and mobility in both the Republic of Ireland and Northern Ireland. The network model is flexible in terms of spatial granularity and parameter selection. We have focused on the first 3 phases of the governmental 5-phase roadmap for reopening society and business in order to model the first wave of the disease on the island and considered different initial conditions, parameters, and mobility data including realistic levels of adherence to movement restrictions. We have observed that the roadmap will lead to a decline of case numbers. However, once the restrictions are lifted, the numbers will rise again, even if an increased level of awareness is considered.

Finally, we have elaborated on a procedure of dynamic interventions that re-introduce lock-down measures, if a certain threshold of infection is reached.

Following such a protocol, the overall number of infected cases can be controlled and safely kept below a prescribed threshold, which can be selected according to the capacity of the health-care system. We have considered that containment measures would be re-introduced on a country-wide level, but a more regional approach (county level) appears feasible as well. It is likely that in the long term, the disease will be contained best by vaccination and not by the development of natural herd immunity [7]. While we have not considered the effects of vaccination in this work, in our model naturally acquired herd immunity, or population resistance, will develop slowly over a long period of time. This is true even with our assumption that infection confers long-lasting resistance, and it is far from clear that this actually the case.

In this chapter we introduced a generalised radiation model which was able to generate commuting patterns, and matched the distance distribution of empirical travel distances as was reported from the 2016 census in Ireland. In the next chapter we look at the applicability of this radiation model to cattle trade.

Chapter 5

Models for Cattle Trade

Despite the importance of trade networks in understanding the spread of infection and disease in farm animal populations, we still lack models that are able to accurately predict these movements on a temporal and spatial scale. Many of the trade networks that have been studied from the context of infection spread have been undertaken as static time-aggregated approximations [143, 187]. Using this approach, we lose the underlying dynamics which characterise animal movement due to trade. An understanding of the mechanisms that influence animal trade is needed to improve our ability to optimise and predict future disease outbreaks in these animal populations.

Beef and dairy farming are important contributors to the economy within the Republic of Ireland, with the agri-food and drink sectors generating 10% of Ireland's exports to the value of approximately €13 billion in 2020 [104]. The cattle population in Ireland is approximately 6.5 million, which outnumbers the human population by approximately 1.5 million [138]. Given this context, outbreaks of animal disease have the potential to create considerable national disruption and associated adverse economic impact. These impacts were observed during outbreaks of foot and mouth disease in Ireland during 1967 and 2001 [45, 83] and especially in the UK in 2001 [88], where approximately 6.5 million cattle were culled resulting in a staggering loss of £8 billion to their economy [183].

As an example, Bovine Tuberculosis (BTB), caused by infection with *Mycobacterium bovis*, is an important endemic disease of cattle. There has been a national eradication programme in Ireland since the late 1950s, including a range of ongoing surveillance and control activities [142]. Nonetheless, infection remains prevalent and widespread throughout the country. Further, cattle movement is recognised as an important constraint to eradication [142]. There is substantial ongoing movement of cattle in Ireland [138], and an improved understanding of the cattle movement network [186, 187]. With robust models for cattle trade in Ireland, it would be possible to test various scenarios, including trading restriction strategies, and determine their effectiveness as part of a national eradication programme. Within this chapter, we elaborate on a framework for cattle trades, based on trades data within, to and from the Republic of Ireland during the year 2017.

As an initial step, a network is often analysed via many common network measures in order to get a sense of the underlying topology, be it static or time-varying. This enables us to determine whether or not the static aggregated network is a good approximation and what information is lost by temporal aggregation of the data. In our analysis, we look at the network as both a time-aggregated static embedding and a temporal network.

In the context of human mobility, there are two models which have been extensively compared to each other against various empirical data sets, including the radiation [6, 174] and gravity [33, 94] models as introduced in Sec. 2.4. While there has been much research into developing models for human mobility, the same cannot be said for cattle trade. However, there has been much analysis of these networks and their properties [12, 76, 159, 187]. As a result, their behaviour and structure is generally well understood. We will attempt to take advantage of particular aspects of the cattle trade network, which shares similarities with human mobility, in order to develop an accurate model for cattle trade.

The radiation model [134, 174] is a parameter-free probabilistic model that is derived under the assumption of human mobility dynamics and population distributions. Thus is not suitable for cattle trade networks in an unaltered state.

The main issue with the radiation model is that it is assumed the probability of a trade into a vertex is highly dependent on population size of that vertex, which while true for human populations, does not hold for cattle herds. We will look at applying a generalised radiation model [6, 105] which allows for a wider range of dynamics at the cost of adding parameters to the model.

The gravity model [33, 89, 175] is a parameterised model that is a generalisation of the law of gravity applied to trade and mobility settings. It is usually dependent on the in-flow and out-flow of the vertices while being inversely proportional to some function of the distance between them. We include analysis of the gravity model as it sees much use in the context of international trade [155, 191].

The structure of this chapter is as follows. We first discuss construction of cattle trade networks from the available data. As the cattle trade network is a combination of a number of trade processes, we split it up into a number of networks such that each new network represents only a single trading process, i.e., direct herd-to-herd trades, herd-to-mart trades, mart-to-herd trades etc.

We analyse each of the considered cattle trade networks in their time aggregated form by computing centrality measures in order to gain a better understanding of the underlying trade process. Then to determine the applicability of these measures to the full temporal networks we investigate the causal fidelity of the networks. Then, we build on the theory of the generalised radiation model we introduced in Chp. 4, and compare it to the gravity model. Following this, we discuss the application of the trade model to network epidemiological models.

5.1 Analysis of Trade Networks

Before attempting to model cattle trade networks, it is vital to first understand the underlying dynamics. In the following, we provide an in-depth analysis of various aspects of the networks in both their temporal and time-aggregated forms.

In order to properly model these trade networks, the model should be able to reproduce many of the findings in our analysis. Then in Sec. 5.2, we develop a model that accessibility describes the empirical data.

5.1.1 Cattle Trade Data

The data set of cattle trades we consider during our analysis is that of all recorded trades between herds in Ireland (noting that this and all subsequent mentions of Ireland refer to the state and not the island) during 2017. The data was obtained from the Centre for Veterinary Epidemiology and Risk Analysis (CVERA) in University College Dublin, as the result of collaborative work in Ref. [98]. There are many types of trade which may occur, for example, from herd to abattoir, from herd-to-herd, importing from abroad, exporting to abroad, etc. However, we are only interested in modelling trades between herds, thus, we only consider the types of trades which facilitate this. This may happen as either a direct trade from one herd to another ('direct herd-to-herd trades') or as an indirect trade from one herd to another via a mart ('indirect mart trades'). Of these two types of trade, there are approximately 1.2 million over the course of the year, and they will be used to construct the temporal networks. The temporal resolution of the data set is relatively granular at one day. Due to the timescale on which cattle are moved, this provides an incredibly detailed view of cattle trades.

From this data we construct four different temporal networks which show varying topological and qualitative behaviours. Due to the fact that trades between herds occur via two distinct process (direct trade between herds or indirect trade via mart), it is worthwhile to consider these processes in their own networks. Thus, we consider the four following distinct networks:

1. Direct herd-to-herd trades.
2. Indirect herd-to-herd trades via marts.
3. Herd to mart trades.

4. Mart to herd trades.

The direct herd-to-herd trade network represents trades which happen directly between herds, i.e., the animals were not bought via a mart. The indirect herd to herd trades via marts represents the trades between herds which happened via a mart. This network bypasses the marts completely by connecting the selling and buying herd with an edge. Then we consider the herd-to-mart trades and mart to herd trades networks. These networks are represented by bi-partite graphs as the marts do not trade with each other and herd-to-herd trades are considered in the first two networks in list given above. It is important to note that although we consider the herd-to-mart and mart-to-herd networks separately, cattle never reside in the mart, but move on to another herd. Thus, for every herd-to-mart trade, there is a corresponding mart-to-herd trade and vice versa.

5.1.2 Cattle Trade Network Representation

In this section we describe the formulation of the cattle trade networks from the data. In our cattle trade networks, vertices are considered as herds or marts and edges are considered as trades. For these networks we do not consider the number of animals traded, simply whether or not a trade occurred, thus we model the cattle trade networks as discrete-time directed graphs, $\mathcal{G} = (G_{t_1}, G_{t_2}, \dots, G_{t_{n_t}})$ where $G_{t_i} = (V, E_{t_i})$. See Sec. 2.1.1 for a description of temporal graphs.

Suppose we have temporally resolved cattle trade data with n_v herds and the trades aggregated into n_t uniformly spaced windows labeled $1, 2, \dots, n_t$ (see Tab. 5.1.3 for the exact numbers of vertices/edges in each network). These windows could be at the level of one day, week, month, etc. The set of vertices, V , is used to represent the herds/marts, and the set of edges at time t_i , E_{t_i} , is used to represent the trades between herds/marts. Moving forward we represent these temporal networks as a sequence of adjacency matrices, or series of adjacency matrices as in Sec. 2.1.1. Suppose we have two herds i and j , and we let $\mathcal{A}^{[t_k]}$ denote

the adjacency matrix for time t_k , then

$$A_{ij}^{[t_k]} = \begin{cases} 1 & \text{if there is a trade from herd } i \text{ to } j \text{ at time } t_k \\ 0 & \text{otherwise,} \end{cases} \quad (5.1)$$

While this representation is useful for analysing the temporal graph in its full form, we first wish to examine each of our cattle trade networks in their time aggregated form as explained in the next section.

5.1.3 Static Network Analysis

We begin the investigation of the cattle trade networks by looking at their aggregated static representations [93]. This flattens our previously defined directed temporal graphs, $\mathcal{G} = (G_{t_1}, G_{t_2}, \dots, G_{t_{n_t}})$, into weighted directed graph, $\tilde{G} = (V, \tilde{E})$, by removing the temporal dimension. The set of vertices, V , remains the same and the set \tilde{E} is the aggregated set of edges and is specified by $\tilde{E} = \bigcup_{i=1}^T E_{t_i}$. The weight of an edge in the aggregated static graph is equal to the number of times it appears in the corresponding temporal graph. This is simply how many times a given herd trades to another over the total timespan of the temporal graph. The adjacency matrix, $\tilde{\mathbf{A}}$, of the aggregated static representation is defined as,

$$\tilde{\mathbf{A}} = \sum_{i=1}^{n_t} \mathcal{A}^{[t_i]}, \quad (5.2)$$

where A_{ij} represents the weight of the edge connecting i to j or the number of trades from herd i to j over the entire time span of the original temporal graph.

Centrality

We now compute a number of standard centrality measures on the static aggregate graphs in order to better understand the underlying topology and trade process

when aggregated over the entire data set. Knowing which herds or marts are most important can help to inform our choice of trade model. The first centrality measure we compute is the degree distribution [145].

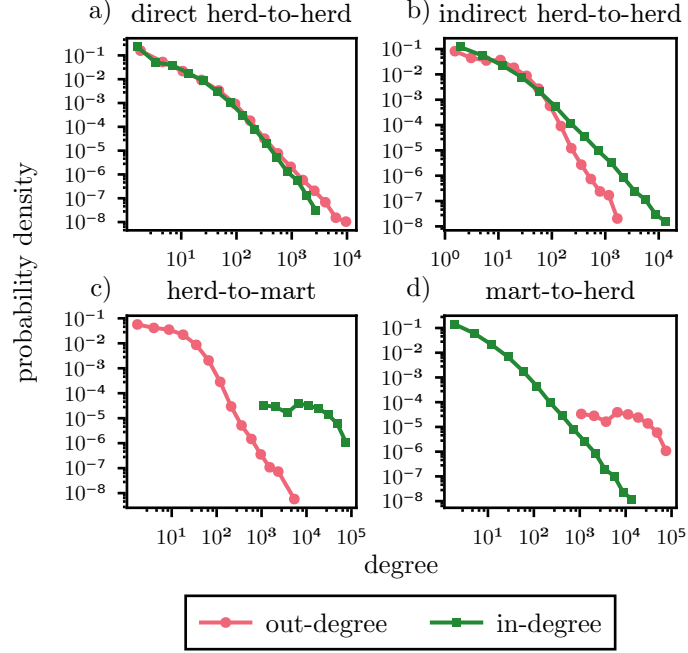


Figure 5.1: The degree distributions for the static network representations of the (a) direct herd-to-herd network, (b) indirect herd-to-herd via mart network, (c) herd-to-mart network, and (d) mart-to-herd network. The red curves with circle marker denote the out degree and the green curves with square marker denote the in degree.

The degree distribution of the static aggregated graph of each network tells us the total number of trades that occur in and out of each herd/mart. In Fig. 5.1 we see the degree distribution for the direct herd-to-herd trade trades in panel (a), for the indirect herd-to-herd trades via marts in panel (b), for the herd-to-mart trades in panel (c), and mart-to-herd in panel (d). The out-degree for each graph is given as the red curves with circle markers and the in-degree for each graph is given by the green curves with square markers. We notice that all 4 plots quite clearly display the properties of a scale-free graph, i.e., a distribution that asymptotically tends to the form $p(x) = x^{-\theta}$ [16]. This corresponds to a linear curve with slope $-\theta$ when plotted on a log scale, as $\log(p(x)) = -\theta \log(x)$,

However, there is quite a difference in the distributions for two of the curves, the in-degree in panel (c) and the out-degree in panel (d). This is because these curves relate to the trades in and out of the marts respectively. As there are only 86 marts in our data set, in which approximately 9.6×10^5 trades occur, they will of course have much higher degrees than the herds as there is far less choice of which mart to trade with than which herd to trade with.

While degree centrality is a useful measure for its simplicity and ease of understanding, it does not take into account the importance of a vertex relative to others through interaction. Two such measures of centrality which take this into account are betweenness centrality [197], which measures importance based on the number of shortest paths which go through a vertex, and page rank centrality [151], which is a type of eigenvector based centrality originally developed for ranking web pages and used in Google’s search engine. For a detailed introduction and discussion on both of these types of centrality, see Sec. 2.1.1.

For the betweenness centrality, we computed this for the aggregated static graphs of the direct herd-to-herd trade and indirect herd-to-herd trade networks only. This is because, in the case of the herd-to-mart and mart-to-herd networks, the marts only trade in or out and herds don’t trade with each other. This leads to a situation in which the betweenness centrality is zero for every vertex in these networks due to the directionality edges and bi-partedness of the graphs. For the betweenness centrality in both cases, the scores were normalized such that they are between zero and one. The distribution of the betweenness centrality measure is plotted in Fig. 5.2 (a) on a double \log_{10} scale. From the figure, we see similar results to that of the degree centrality in that there is some scale free behaviour resulting in a few vertices that are central to network. In terms of disease spread these are often referred to as “sentinel nodes”, as they have the capacity to act as early indicators of epidemics, as they are likely to see the disease very quickly after it enters the network [23, 150].

For the page rank centrality, we also computed this on the aggregated static graphs of the networks, like before, only on the direct herd-to-herd trades and the indirect herd-to-herd trades via marts. This is again due to the bi-partite and

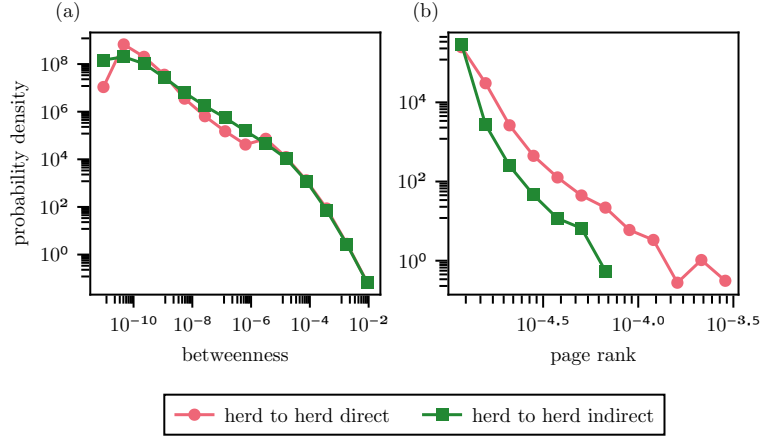


Figure 5.2: Distributions of the (a) betweenness and (b) page rank centrality for the direct herd-to-herd trade network (red line circle markers) and the indirect herd-to-herd via mart network (green curve square markers).

directed structure of the herd-to-mart and mart-to-herd networks which make quantifying importance difficult as the network is largely disconnected, as we will see later in this section. For these two networks degree distribution provides a better picture of vertex centrality.

For this measure of centrality, the importance is influenced by the number of edges pointing into a vertex, but also the importance of the vertices the edge is coming out of. The distribution of page rank centralities is given in Fig. 5.2 (b) where the direct herd-to-herd trades is given as the red curve with circle markers and the indirect herd-to-herd trades via marts is given as the green curve with square markers. The centralities were both normalised such that the sum of all centralities is one. From the plots, it is clear there is some agreement between both centrality measures of the herd-to-herd direct and herd-to-herd indirect networks. The bulk of herds appear to be unimportant in connecting the network via trades, however, there exists a relatively small number of particularly influential herds which are responsible for a significant portion of all trades, and also, important in connecting herds to one another. Thus, care should be taken in the modelling to ensure that the importance of these nodes are reproduced. This is because these nodes play a vital role, not just in terms of their trade, but also in terms of the spread of infection and disease. That is, if one of these important nodes

were infected while trading freely, a large portion of the network would be quickly infected. If a goal of these trade models is to allow for the investigation of various disease control strategies by means of trading strategies, then the activity of these influential herds should be reproduced by the models.

Connectivity

We now turn our focus to large scale network measures, as given in Tab. 5.1.3. These measure give a sense of how connected the network is, i.e. how easy it is to travel from one node to another. The first measure computed is the size of the Giant Strongly Connected Component (GSCC), i.e., the number of nodes it is composed of. The GSCC is the (not necessarily unique) largest subgraph of a directed graph for which a path exists between any two vertices. For the considered trade networks we found the sizes of their GSCC to be 17649 (8.83%), 21975 (10.99%), 1, ($\sim 0\%$) and 1, ($\sim 0\%$) for the direct herd-to-herd, indirect herd-to-herd via mart, herd-to-mart and mart-to-herd trade networks respectively. The reason for the difficulty in measuring centrality for herd-to-mart and mart-to-herd is evident from the size of their GSCC, which is 1. In other words, there exist no paths in which you can return to the starting vertex of that walk.

The next measure computed is the size of the Giant Weakly Connected Component (GWCC). The GWCC is the largest subgraph of an undirected realisation of a directed network for which a path exists between any two nodes. For the considered trade networks, the sizes of the GWCC were computed to be 73256 (36.64%), 94313 (47.17%), 82584 (42.31%) and 58099 (29.06%) for the direct herd-to-herd, indirect herd-to-herd via marts, herd-to-mart and mart-to-herd trade networks respectively. Looking at the edge density of all four networks, we notice that they are very sparse with quite a majority of the trades occurring via marts. With such sparse static representations, we would expect the temporal realisations of these trade networks to be even more sparse as these static networks ignore any temporal causality which is an important aspect of temporal networks. Finally, we look at the diameter of the networks. This quantity is

the longest shortest path that exists between any two vertices. Given that no path exists between most pairs of vertices (as indicated by a small GSCC), we restrict the diameter to just the largest GSCC of the networks, otherwise the diameter would be infinite (a distance between nodes for which no path exists is infinite). The diameter is found to be 30, 20, 0, and 0 for the direct herd-to-herd, indirect herd-to-herd via marts, herd-to-mart, and mart-to-herd trade networks, respectively.

	direct	indirect	herd to mart	mart to herd
No. Vertices	199,908	199,908	199,908	199,908
No. Edges	243,531	968,418	382,035	382,035
Edge Density	6.09×10^{-6}	2.42×10^{-5}	9.56×10^{-6}	9.56×10^{-6}
GSCC	17,649	21,975	1	1
GWCC	73,256	94,313	82,584	58,099
Diameter	30	20	0	0

Up to now in this chapter we have only considered the trade networks in their static form, aggregated over time. While this offers a useful insight into the structure of the network, it does not account for any temporal patterns, which are important aspects of the true network. This is especially true in the case of cattle trade which sees very seasonal activity (see Fig. 3.10). We look at the network in its full temporal setting in the next section.

5.1.4 Temporal Network Analysis

We now consider the full temporal network representation of the cattle trade data sets. Temporal networks is an area that is currently under much active research, as such, the approach to their analysis is not as standard as their static network counterparts. The first measure we look at is what is referred to as causal fidelity, a measure based on the accessibility matrix as given in Ref. [122]. We saw a temporal matrix based on this concept in Chp. 3 which we called the Non-Backtracking (NBT) matrix. Given the analysis on the static aggregated

representations of the networks, we would like some sense of how close they are to their temporal networks. Without some measure of closeness, it is difficult to interpret the static measures from the context of the temporal networks. Causal fidelity is a very simple measure that gives the fraction of paths in the static network which can be realised in a time respecting manner. In order to calculate this quantity we first need the accessibility matrices of both the aggregated and temporal networks. The accessibility matrix of a temporal network including paths up to length n and up to time t_n is given as the following,

$$\mathcal{H}(n) = \prod_{k=1}^n \left(\mathcal{A}^{[t_k]} + \mathbf{Id} \right), \quad (5.3)$$

where $\mathcal{A}^{[t_i]}$ is the adjacency matrix of the temporal graph at time t_i as defined in DEc. 2.1.1. The quantity $\mathcal{H}_{ij}(n)$ tells us how many time respecting paths of length n there are between vertex i and j up to time t_n . The accessibility matrix of a static graph including paths up to length n is given as,

$$\mathbf{H}(n) = \sum_{k=0}^n \tilde{\mathbf{A}}^k, \quad (5.4)$$

where $\tilde{\mathbf{A}}$ is the adjacency matrix of the static time-aggregated graph as given by Eq. (5.2). The quantity H_{ij} tells us how many (not time-respecting) paths there are between vertex i and j of length n in the static time aggregated graph.

With the definition of the accessibility matrices in mind, the causal fidelity up to time step t_n is defined as

$$\frac{\phi(\mathbf{H}(n))}{\phi(\mathcal{H}(n))}, \quad (5.5)$$

where the function ϕ is simply the number of non-zero values in the matrix. For the three considered networks, we computed the causal fidelity at up to day 60 for both the direct herd-to-herd network and the indirect herd-to-herd network and plot the results in Fig 5.3.

The times at which the minimum values for causal fidelity occur are at $t_n = 31$

with a value of 1.3×10^{-4} for the direct herd-to-herd trades and at $n = 14$ for the indirect herd-to-herd trades with a value of 8.3×10^{-5} . From the results of the causal fidelity, it is clear that the time-aggregated static network representations only tell a small part of the story. Unless the total time being looked at is a small number of days, i.e., less than approximately ten days, most paths, which exist in the time-aggregated static networks, will not be possible to realise in a time respecting manner in their temporal counterparts. It may be the case that the time-aggregated static network gives a good approximation after many months, however the computation of causal fidelity is quite a computationally expensive process, and so we only compute up to 60 days. It can be seen in both trades networks (Fig 5.3) that the causal fidelity begins to increase after a certain point when most of the edges that are appearing in time have been seen before, making many of the paths that were possible in the time-aggregated static networks now also possible in the full temporal networks.

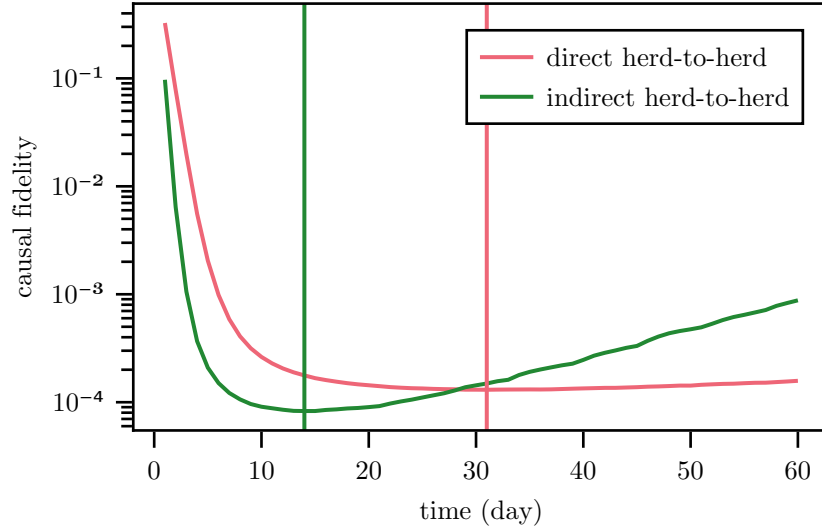


Figure 5.3: Plot of the causal fidelity for the direct herd-to-herd network (red curve) and indirect herd-to-herd via marts network (green curve) for the first 60 days of the date set. The minimum value of each curve occurs at the time indicated by the vertical line of the same colour.

In order to reason why the causal fidelity is so low for these networks, we investigate the waiting-times between successive trades in or out of a herd, this is sometimes referred to as the inter-event time [164]. Fig 5.4 shows the distribution

of these waiting-times for all four of our networks. The distribution of waiting-times which were computed are only for herds which had more than one trade during the year our data set spans, this is because waiting-times require at least two trades to have occurred. With the double \log_{10} scale, it is clear that the possible waiting-times vary over orders of magnitudes with the average being 26.4, 13.2, 39.4, and 0.075 days for the direct herd-to-herd, indirect herd-to-herd, herd-to-mart, and mart-to-herd networks respectively. These waiting-times however, do not indicate how many trade partners a herd had during a particular time step, only that at least one trade occurred. Going by the average waiting-times, days during which a herd makes a trade is quite rare, being approximately between every one to one and a half months, except in the case of the mart-to-herd trades, but this expected as marts only exist to be platforms to trade, thus they will have very high rates of activity. The chance then of a herd making a trade with a partner they have traded with before is even lower and depends on some measure of loyalty or chance of an edge reoccurring in the network. Because an edge exists in the time-aggregated static network for every time step it makes sense the causal fidelity is so low. It is because most of the paths in the time-aggregated static networks are not time-respecting as it takes so long for edges to reappear in the temporal network, which when they do, gives rise to new time respecting paths that occur in both the time-aggregated static networks and temporal networks, increasing causal fidelity.

We have introduced and analysed a number of cattle trade networks and gained a deeper understanding of their structure. In the next section we introduce a number of potential models which attempt to recreate the cattle trade networks. The metric by which we determine good fit is by how well the distance distribution of trades is matched.

5.2 Models for Cattle Trade

We now have a broad sense of the structure of our four cattle trade networks, in both their full temporal realisation, as well as their time aggregated static forms.

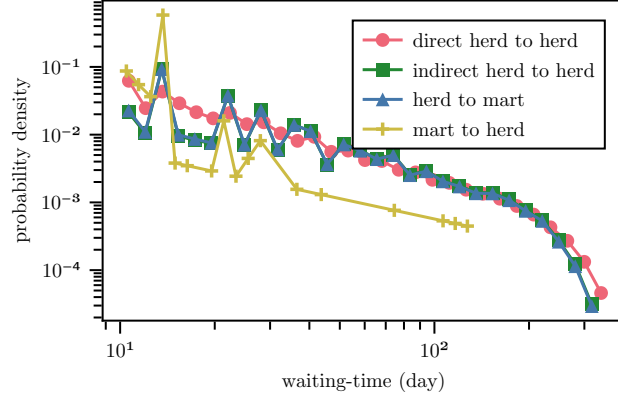


Figure 5.4: Plot of the distribution of waiting-times between trades for each vertex in the direct herd-to-herd network (red curve with circle marker), the indirect herd-to-herd via marts network (green curve with square marker), the herd-to-mart network (blue curve with triangle marker), and the mart to herd network (yellow curve with cross marker).

In this section we, look at a number of models, specifically, forms of the gravity model [175] and the gravity model [174] and investigate which of these gives the best fit to our data.

5.2.1 Gravity Model

In this section, we present a number of potential gravity models for modelling cattle trades in the Republic of Ireland. The gravity model is a relatively simple model and thus has seen much popularity over the years in modelling things such as international trade flow [191] and human mobility [134]. Following this, we believe that the gravity model would be a good starting point for modelling cattle trades. The model is a heuristic model based on Newton’s classic formulation for gravity (hence the name). As discussed in Sec. 2.4, the general form of the gravity model is given as the following,

$$G(i, j) = \frac{x_i^\alpha y_j^\beta}{f(d_{ij})}. \quad (5.6)$$

The two parameters α and β do not always appear in the formulation, in fact, using maximisation of entropy techniques finds that the parameters are both one [200]. However, this often leads to a poor fit to data. This equation describes the attraction between two vertices i and j where x_i and y_j are some quantity of attractiveness, i.e., a quantity which makes interaction with a vertex more likely. In human mobility, this is often population size [188] and in the context of international trade can be Gross Domestic Product (GDP) [136]. The quantity d_{ij} , is the distance between the vertices i and j , and f is a distance kernel. This function f describes the rate at which the attractiveness between two locations increases or decreases with the distance between them. The choices for the function f will be discussed below. The parameters α and β have no real significant meaning other than to help with fitting the model.

In order to apply the cattle trade data to this model, we assume that the attractiveness is proportional to the herd size. We determine the herd size as the total number of cattle in a herd on the first date in our data, which is 01/01/2017. Herd sizes will of course change over time, but we assume they stay approximately the same over the course of a year. For the marts, which have no herd size, we assume that their attractiveness is proportional to the historic in-degree and out-degree of their static time-aggregated graph representations.

The particular form of the gravity model we will use is the production constrained gravity model [67, 84] (see Sec. 2.4). This is to ensure that we have a number of trades out of a vertex that is proportional to its actual out degree, thus ensuring the out-degree in the actual networks can be matched. According to production constrained gravity model, the expected number of trades from vertex i to j is given by

$$T_{ij} = \frac{u_i N_j^\beta f(d_{ij})}{\sum_{k \in V} N_k^\beta f(d_{ik})}, \quad (5.7)$$

where u_i is the out degree of vertex i and N_i is the herd size of vertex i .

Given the above formulation, we fit the parameters of the model by means of maximum likelihood estimation [175]. It is quite common to fit gravity models by means of multinomial regression, however, this can have serious problems in the

presence of many zero trades [33] which is the case for our very sparse networks. We have found much better fits to the data by means of maximum likelihood estimation. To fit via maximum likelihood estimation, we define the probability of a trade from vertex i to j , given i is selling as,

$$P_{\text{grav}}(i, j) = \frac{T_{ij}}{\sum_{x, y \leq N} T_{xy}}. \quad (5.8)$$

This probability now allows us to define our likelihood function to optimise.

For the choice of distance kernel, f , we investigate two possibilities. The two most common kernels found in literature are the power-law [94] and exponential functions [13]. The kernels we consider are given below as,

$$f(d; \gamma) = \begin{cases} e^{\gamma d}, \\ d^{\gamma}. \end{cases} \quad (5.9)$$

While these are the most common choices, there are sometimes others seen, such as a combination of power-law and exponential [128] or even a log-normal distribution [74].

5.2.2 Radiation Model

Next, we introduce the radiation model, first introduced in the seminal paper [174], with many extensions since [6, 118, 127, 129, 160]. The radiation model aims to predict the flow of people between physical locations based on first principles, in a manner similar to that of the process of radiation, hence the name. As the radiation model is based on first principles in that it produces a probability distribution with expected value and variance, thus overcoming many of the problems associated with the gravity model, which has no such derivation but is heuristic in nature. A useful benefit of the radiation model is that it often does not require any parameter fitting and thus needs no empirical mobility data in order to use it. However, this is not always the case [6, 118] as we shall see with

our data.

Traditionally, the radiation model is used in the context of human mobility, however, our goal is to model cattle trades within the Republic of Ireland. While similar in scope, we shall see that a slight generalisation is required. We now describe the radiation modelling framework similarly to [174] in terms of cattle trade.

A herd owner seeks a selling opportunity, i.e. the herd owner wishes to sell, among all other herds or marts. The number of selling opportunities available in a herd is proportional to some function of the herd size, which we assume to take the form $g(n) = n^\alpha$. Thus, each herd has n^α/c_α selling opportunities, where c_α is some constant that represents the number of cattle per selling opportunity in a herd. Similarly, the number of buying opportunities available in a herd is proportional to some function of the herd size, $h(n) = n^\beta$, which has the same functional form as the selling opportunities but has a different exponent. Thus, each herd has n^β/c_β buying opportunities, where c_β is some constant that represents the number of cattle per buying opportunity in a herd.

The benefit of a selling/buying opportunity, z , captures information such as price, herd quality, herd health history etc. This quantity z is randomly chosen from a probability distribution $p(z)$, where the form of the distribution does not matter as the final probability is not dependent on it. Each herd with a size of n has n^α/c_α random selling benefits and n^β/c_β random buying benefits drawn from $p(z)$, associated with it. When a herd owner is looking to buy from another herd, they compare their buying benefits with the selling benefits of all other herds. They choose the closest selling opportunity which is higher than their own maximum buying benefit.

The probability of herd i with size N_i selling to herd j with size N_j is given by,

$$P_{\text{rad}}(i, j) = \int_0^\infty P_{N_i^\beta}(z) P_{s_{ij}}(< z) P_{N_j^\alpha}(> z) dz, \quad (5.10)$$

where $s_{ij} = \sum_{k \in r(i, j)} N_k^\alpha$ is the sum of all herd sizes, to the power of α , for each

herd in k in $r(i, j)$. The set $r(i, j) = \{k : d(i, k) < d(i, j), k \notin \{i, j\}\}$ is the set of all herds within (Euclidean) distance $d(i, j)$ of herd i , not including herd i or j . Finally, $P_x(z)$ is the probability of having a maximum value of z after x samples from $p(z)$ ($P_x(< z)$ and $P_x(> z)$ are the probabilities of attaining a max value less than or greater than z respectively, after x samples from $p(z)$). Therefore, from Ref. [174], we find,

$$P_{\text{rad}}(i, j) = \frac{N_i^\beta N_j^\alpha}{(N_i^\beta + s_{ij})(N_i^\beta + N_j^\alpha + s_{ij})}. \quad (5.11)$$

This quantity describes the exact same probability as Eq. (5.8), the probability of a trade from vertex i to vertex j given that herd i is selling. Note that the parameters α and β in this model represent different quantities to those in the gravity model.

We now have a description of a generalised radiation model with which we can model cattle trade. There are a few such radiation models that already go by the name generalised radiation model [6, 134], though they are both different in scope, ours would fall under the description of Ref. [6]. With our two potential models for cattle trade, we now move onto fitting and testing how well these models recreate the properties of the cattle trade networks.

5.3 Results

In this section, we present our results on how well both the gravity model and generalised radiation model are able to fit the cattle trade data. In terms of the networks we test the models against, we only use the direct herd-to-herd, herd-to-mart, and mart-to-herd trade networks. The reason we do not include the indirect herd-to-herd via mart trade network is that it is a compound process of trading to a mart and then trading to a herd. This adds a complication when attempting to model this process. So instead, we simply model to two separate processes using the herd-to-mart and mart-to-herd trade networks.

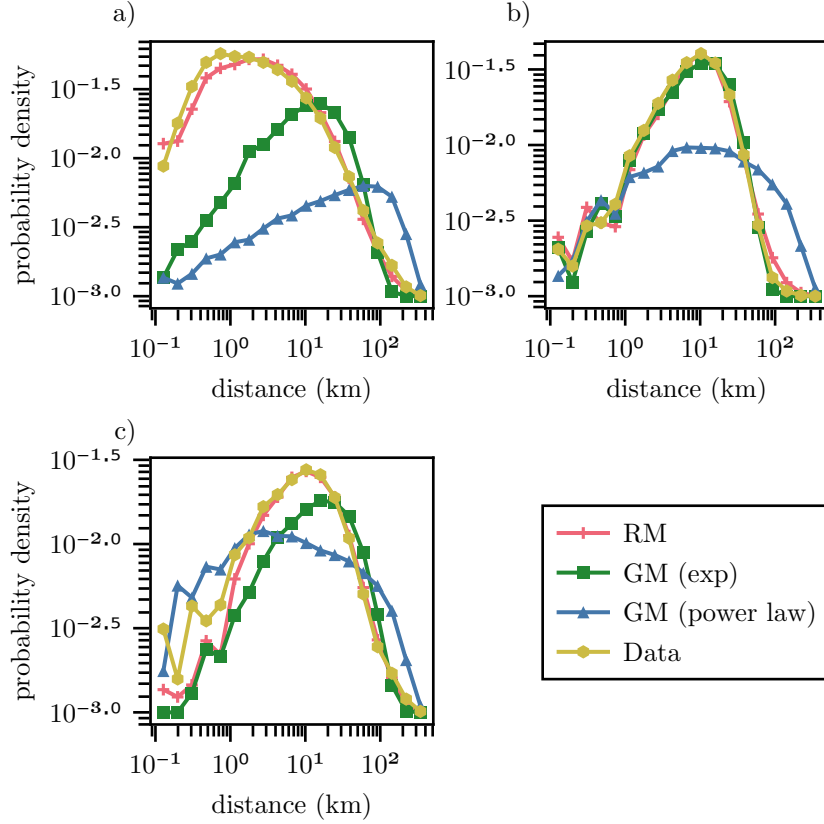


Figure 5.5: Distance distributions generated by 10^5 random samples from the exponential gravity model (GM (exp)), power-law gravity model (GM (power law)), and the radiation model (RM). The models were run with their best fit parameters as given in Tabs. 5.1, 5.2, and 5.3. Panel (a) shows the direct herd-to-herd cattle trades network, panel (b) shows the herd-to-mart cattle trade network, and panel (c) shows the mart-to-herd cattle trade network. In all cases the red curve with cross markers refers to the radiation model, the green curve with square markers refers to the exponential gravity model, the blue curve with triangle markers refers to the power-law gravity model, and the yellow curve with circle markers refers to the distance distribution of the actual network.

We fit the models given by Eqs. (5.8) and (5.11) to three cattle trade networks as described above by means of maximum likelihood estimation. The parameters fit to the direct herd-to-herd trades are given in Tab. 5.1, to the herd-to-mart trades in Tab. 5.2, and to the mart-to-herd trades in Tab. 5.3.

In order to investigate how well these models reproduce the original data sets, the first thing we compare them to is the distribution of trade distances from the trade networks. We simulated a large number (10^5) of trades from each of

Direct herd-to-herd trades			
	Exponential Gravity	Power-Law Gravity	Radiation
α	—	—	1.48
β	0.31	0.25	0.0326
γ	5.95×10^{-5}	0.53	—

Table 5.1: The parameters found after fitting the exponential gravity model, the power-law gravity model and the radiation model to the direct herd-to-herd cattle trade data.

the models on each network in order to produce robust distributions to compare against. In Fig. 5.5 we plot the distance distributions for generated by each model for the direct herd-to-herd cattle trades in panel (a), for the herd-to-mart cattle trades in panel (b) and the mart-to-herd cattle trades in panel (c). In each panel, the radiation model is plotted as the red curve with cross markers, the gravity model with exponential distance kernel is plotted as the green curve with square markers, the gravity model with power-law distance kernel is plotted as the blue curve with triangle markers, and the distance distribution of the cattle trade network is plotted as the yellow curve with circle markers.

In Fig. 5.5 we see remarkable agreement between the distance distribution of the cattle trade networks and the radiation model in every case. In panel (a) both of the gravity models completely fail to capture the true distance distribution in the direct herd-to-herd cattle trade network, whereas the radiation model appears to almost completely agree. Interestingly, in panel (b) both the radiation model and the exponential gravity model perform very well on the herd-to-mart cattle trade network, capturing the distance distribution across all scales. On the other hand, the power-law gravity model again fails to capture the true distribution. Finally, in panel (c) this is the worst performing for the radiation model with it slightly overestimating trades at shorter distances. That being said, it still fits the bulk of the data very well and again outperforms both gravity models.

From these plots, it reveals that the radiation model very accurately recreates the distribution of trade distances in every case. The exponential gravity model appears to produce a good fit to the herd-to-mart cattle trades, and a moderate fit in the mart-to-herd cattle trades, but fails in the direct herd-to-herd trades. The power-law gravity model is the worst performing in each case and does not

Herd-to-mart trades			
	Exponential Gravity	Power-Law Gravity	Radiation
α	—	—	0.46
β	2.46	2.204	0.24
γ	1.13×10^{-4}	1.0	—

Table 5.2: The parameters found after fitting the exponential gravity model, the power-law gravity model and the radiation model to the herd-to-mart cattle trade data.

Mart-to-herd trades			
	Exponential Gravity	Power-Law Gravity	Radiation
α	—	—	0.99
β	0.29	0.31	0.30
γ	4.032×10^{-5}	1.0	—

Table 5.3: The parameters found after fitting the exponential gravity model, the power-law gravity model and the radiation model to the mart-to-herd cattle trade data.

produce any convincing fits.

We have shown that our generalised radiation model provides an excellent fit to our data by recreating the distance distributions across all of the considered cattle trade networks. This new model provides opportunities in the context of epidemiological modelling which were not possible before. It allows us to create epidemiological network models in which the trading patterns are reactive to infective state other herds. We discuss such possibilities in the next section.

5.4 Application to the Spread of Disease

A major use of these models for cattle trade is the ability to use them in the context of epidemiological models. In Chps. 3 and 4 we saw that much of our epidemiological network models were run on graphs informed by empirical networks [15], i.e., data-driven models. The use of such data is clearly beneficial in the context of understanding how a disease spreads in the given context. However, we often want to be able to model a disease under the assumption of some change in the network structure. The use of empirical data does not allow us to do this, but with an accurate and flexible model such as the radiation model, we would be able make changes to the network structure, such as by removing vertices or changing herd sizes, and we would expect the radiation model to handle such changes and respond by producing likely trading patterns under the new altered network.

As discussed in the introduction of this chapter, the cattle industry is incredibly important to Ireland. As such, the evolution of disease that affect cattle are monitored very closely and there is active effort to try and eradicate many of them, such diseases include Johne's disease [72, 80] Bovine Viral Diarrhoea (BVD) [20, 72, 76] and BTB [142]. BTB has been a problem in Ireland for many years, whereas the previously mentioned diseases have seen significant reductions in prevalence thanks to testing and control measures [137, 185]. The disease appears to be difficult to eradicate in part because it is endemic in the surrounding wild life and is carried by both badgers and deer [32]. As a result, more serious measures must be taken if it is to be eradicated as current control measure do not appear to be enough [142].

In Ref. [72], we introduced a stochastic model for the spread of BVD among cattle. This paper looks specifically at the effects of stochastic components on the spread of the disease. However, the model does not take into account network effects, and assumes a well mixed population. A benefit of our radiation model is its probabilistic nature. This means it would fit into the stochastic analysis of an extension to this paper, and we could analyse the effects of a stochastic network

on the spread of BVD by considering the probability of trade between herds.

In Australia an effective risk based trading strategy was implemented [141] which saw the country totally eradicate the disease. This strategy saw herds unable trade with others depending on their level of risk. As a result, there has been some research into whether or not this would be possible in Ireland or the UK [2, 126].

By modelling the effectiveness of risk based trading in Ireland from the viewpoint of networks, it could lead to some very interesting results. The problem with developing such a model is that it would be difficult to use empirical data in the form of our cattle trade networks. This is because the effect of preventing particular herds from trading would require a model for building the trade network under the particular restrictions, very similar to how we built different commuting patterns under various lock-down effects in Chp. 4.

5.5 Summary

In this chapter we have analysed cattle trade in Ireland from the viewpoint of a number of networks, which split the cattle trades into their various trade processes. They are the direct herd-to-herd, indirect herd-to-herd via mart, herd-to-mart, and mart-to-herd cattle trade networks. We have studied the networks in both their temporal and time-aggregated forms computing a number of centrality measures in order to determine the importance of herds in the trading process.

We looked at a production constrained gravity model and developed a new radiation model which described the trading patterns among herds in a probabilistic way. After fitting the models to the cattle trade data, we have found that the new radiation model provides an exceptional fit to the distance distributions of cattle trades in Ireland for each of the networks we considered. We then discussed the potential for the use of models for cattle trade in the context of epidemiology and risk-based trading.

Chapter 6

Conclusion and Outlook

This thesis contributes to the theory of mathematical epidemiology and network science by combining the two areas of study. In recent years, with the outbreak of SARS-CoV-2 we are reminded of the importance of accurate mathematical models in the context of epidemiology, especially in the absence of pharmaceutical intervention when public health measures and policy is the only tool available to prevent the spread of disease. Human life is often not the only cost of epidemics, quite often animals are affected, as in the case of the 2001 foot and mouth outbreak, and with that comes great economic cost as well.

Thanks to the explosion in the amount of data available, we are now able to study the interplay between contact patterns and the spread of disease, allowing for far more accurate models of disease spread, which are also spatially resolved. There are many such models which are used to describe the evolution of diseases on networks such as the individual and pair based models. In order to aid the development of mitigation strategies, it is necessary to extend these models to a temporal setting in order to take advantage of much of the temporally resolved data available.

An integral part of accurately modelling the spread of disease on networks is understanding the contact patterns which define the network and how they are

generated. Models for generating contact patterns that can accurately recreate patterns in the true system can be very useful when there is a lack of data available or for testing how certain scenarios would change current contact patterns.

Chapter 2 In Chp. 2, we introduced the theoretical background required for the rest of the chapters in the thesis. We introduced the basic concepts of networks science, including definitions of various graphs, as well as their extension to the temporal domain. We also discussed the concept of centrality, which is an important concept in many areas of network science, including epidemiology, which classifies importance of vertices based on a number of metrics like number of neighbours or average distance to all other vertices. Moving on from basic network theory, we introduced the original generalised Susceptible-Infected-Recovered (SIR) model for well mixed populations as given by Kermack and McKendrick and showed how the modern SIR is derived from it with the assumption of constant parameters.

After the basics of networks and epidemiological models are introduced, we then presented the current state of epidemiological network models by discussing two common frameworks by which to model epidemics, they are the Individual-Based (IB) model and the meta-population model. In both cases the models are realised as the SIR model. An important concept in epidemiology is that of the basic reproduction number, which is the expected number of new infection generated by a single infected individual. For both the models, we analytically derived this quantity and show they are equivalent to the well mixed SIR model in the absence of any contacts/travel.

The final concept discussed in Chp. 2 are models for mobility. We introduced the two most common models with which to generate the movement of individuals in a network. They are the gravity model and the radiation model. We saw the radiation model used in Chp. 4 for generating rates of travel of individuals which changes depending on current movement restriction, and in Chp. 5 we discussed the use of the gravity and radiation models and show how they can be extended in order to model cattle trade.

Chapter 3 In Chp. 3 we introduced a general framework for modelling the spread of epidemics on temporal networks. We showed that this framework unifies many of the already existing network models by deriving the individual-based, pair-based, and contact-based models from it. We also derived a new formulation of the pair-based model which is exact as it does not depend on the linearisation of terms. In the derivation of these models, we do so with temporal networks so that we end up with Temporal Individual-Based (TIB) and Temporal Pair-Based (TPB) models.

By means similar to in Chp. 2, we derived the conditions necessary for an epidemic according to the TPB SIR model by analytically deriving the basic reproduction number, and showing that it is the same condition as in a previously derived TIB SIR model.

A defining feature of the pair-based model is that it is derived under the assumption of a particular network structure, which is there is no more than one Non-Backtracking (NBT) path between any two vertices. For an undirected graph this implies a tree structure. We showed that the proportion of vertex pairs in a graph which have more than one NBT path between them is a useful metric to indicate the accuracy of the TPB model when compared to the ground truth which is the average of a large number of Monte-Carlo (MC) realisations.

An opportunity for future work in this area is to derive a triple-based model from our framework. Though the derivation would be more complicated it would lead epidemiological network models which would be able to account for triangles (cycles of length 3) and prevent the formation of echo chambers even further than that of the TPB model.

Another further area of study would be designing a decision based algorithm which can use the proportion of pairs of vertices which have more than one NBT path between them. It may be possible to determine the actual error of the TPB model from this proportion, or to at least approximate it. At times which see a large increase in this proportion, we could instead switch to a MC algorithm which could move the evolution of a disease forward in time more accurately (for

some graph structures), but at the cost of longer running time. When the $c(t)$ settles, we could then switch back to the TPB model and expect decent accuracy.

Chapter 4 In Chp. 4 we presented a new meta-population model for the spread of SARS-CoV-2 on the island of Ireland. We started by introducing a Susceptible-Infected-Quarantined-Recovered-Dead (SIQRD) model for small well mixed communities in the as the origin Kermack and McKendrick SIR model. For this well mixed model we derived the basic reproduction number by means similar to Chps. 2 and 3. We also derived the condition necessary for herd immunity in this model, that is, the required number of individuals that need have left the susceptible state. We defined this quantity the herd immunity threshold.

Next we extended this SIQRD model using the meta-population framework, in order to model the spread of SARS-CoV-2 in Ireland. The network on which the model was defined is such that each vertex in the network corresponds to an electoral division/super output area, which are the smallest administrative units in Ireland and Northern Ireland respectively, and the edges correspond to travel rates between areas/vertices. For the network case, we again derived the basic reproduction number and herd immunity threshold.

The travel rates in the network were generated using a radiation model which is informed by data from the 2016 Irish census. We made a small extension to the radiation model which leads to a far better fit to the actual distance distribution of trips reported by the census. We then made the rates depend on time by multiplying them by a sine function in order to simulate the process of commuting where individuals leave and return. This also had the effect of keeping populations of vertices periodic.

We then applied our model in order to simulate the spread of the disease in Ireland. We justified the use of our parameters from various sources except for the rate of contact times probability of infection, β . We fit this parameter from historic data, with the parameter taking on a different value for each phase in the early stages of Ireland's lock-down and reopening phases. When compared to

the actual deaths and infections, our model provides a convincing fit.

We presented two different lock-down scenarios, one at the level of island and one at the level of county. If the island/county surpassed some threshold of infected, we put the island/county back into lock-down and it must go through the reopening phases of the first historic lock-down. This is a simple model of the lock-down-reopen strategies employed by many countries. We wished to test if it was possible to reach herd immunity in a controlled way, such that deaths were minimised. However, we found that for the parameters used in our lock-down model, which was informed by actual public health measures, that herd immunity would take at least 28 years. This implied that such a strategy for reaching herd immunity is not feasible. We also found that county level lock-down, without 100% compliance of lock-down restrictions, the largest county Dublin, was at times unable to reduce its level of infected individuals due to interaction with bordering counties.

The work in this chapter was completed under the assumption of no effective vaccine, which we know is not the case. It would be beneficial to include the effects of vaccination in an extension to this study, and model the possible scenarios in which herd immunity could be reached. As we tried to keep the model simple while retaining the key characteristics of the disease, there are a number of possible extensions to the model itself. For example, we do not take into account incubation time of the disease or the fact that a significant proportion of infected individuals are asymptomatic. It has also been reported that the mortality rates of disease are very age dependent, and so it may be useful to split the population into different age strata in order to better model deaths within the population.

Chapter 5 In Chp. 5 we presented an analysis of the properties of a temporal cattle trade network in Ireland. The network is the same as the cattle trade network presented in Chp. 3 on which our TPB and TIB models were tested. We split the cattle trade network up into four unique networks, each of which represented a different trading process in network. These were the direct herd-to-herd trades, herd-to-mart trades, mart-to-herd trades, and finally the indirect

herd-to-herd trades which combine the herd-to-mart and mart-to-herd trades such that the mart is bypassed and only the selling and buying herds are considered.

On these networks we computed a number of centrality measures on their static time aggregated representations. This gave us an insight into the relative importance of herds in the network. We then analysed the networks in their full temporal realisation by looking the causal fidelity which gives us a sense of how applicable the analysis on the static network representations is.

We then developed 3 separate models for cattle trade, two of which are versions of the gravity model and the third is a generalised radiation model developed specifically for cattle trade. We found that the radiation model provides an excellent fit to the data. When compared to the actual distance distributions of cattle trades for each of the temporal networks, the distance distributions generated by our radiation model are incredibly close. Thus, we show that our radiation model provides an excellent description of the trading process among herds in Ireland.

This model is particularly applicable in the context of network epidemiological models. An area in which we would like to see this model developed further is in the context of risk based trading among cattle herds in Ireland, similar to a strategy implemented in Australia which saw the eradication of Bovine Tuberculosis (BTB). The availability of an accurate and flexible model for cattle trade would let us model how different trading strategies would potentially affect the spread of disease, particularly BTB.

To sum up, this thesis contributed new results to the field of mathematical epidemiology and network science. We discuss a number of new results as well as their implications.

Appendix A

Vertex Pair Transition Rates for the PB Model

$$W_{S_i, I_j | S_i S_j}(t_n) = \prod_{\substack{k \in V \\ k \neq j}} \left(1 - \beta \mathcal{A}_{ki}^{[t_n]} \frac{P_{S_i, I_k}(t_n)}{P_{S_i}(t_n)} \right) \left[1 - \prod_{\substack{k \in V \\ k \neq i}} \left(1 - \beta \mathcal{A}_{kj}^{[t_n]} \frac{P_{S_j, I_k}(t_n)}{P_{S_j}(t_n)} \right) \right] \quad (\text{A.1})$$

$$W_{I_i, S_j | S_i S_j}(t_n) = \left[1 - \prod_{\substack{k \in V \\ k \neq j}} \left(1 - \beta \mathcal{A}_{ki}^{[t_n]} \frac{P_{S_i, I_k}(t_n)}{P_{S_i}(t_n)} \right) \right] \prod_{\substack{k \in V \\ k \neq i}} \left(1 - \beta \mathcal{A}_{kj}^{[t_n]} \frac{P_{S_j, I_k}(t_n)}{P_{S_j}(t_n)} \right) \quad (\text{A.2})$$

$$W_{I_i, I_j | S_i S_j}(t_n) = \left[1 - \prod_{\substack{k \in V \\ k \neq j}} \left(1 - \beta \mathcal{A}_{ki}^{[t_n]} \frac{P_{S_j, I_k}(t_n)}{P_{S_j}(t_n)} \right) \right] \\ \times \left[1 - \prod_{\substack{k \in V \\ k \neq i}} \left(1 - \beta \mathcal{A}_{kj}^{[t_n]} \frac{P_{S_j, I_k}(t_n)}{P_{S_j}(t_n)} \right) \right] \quad (\text{A.3})$$

$$W_{I_i, I_j | S_i I_j}(t_n) = (1 - \mu) \left[1 - (1 - \beta \mathcal{A}_{ji}^{[t_n]}) \prod_{\substack{k \in V \\ k \neq j}} \left(1 - \beta \mathcal{A}_{ki}^{[t_n]} \frac{P_{S_i, I_k}(t_n)}{P_{S_i}(t_n)} \right) \right] \quad (\text{A.4})$$

$$W_{S_i, R_j | S_i I_j}(t_n) = \mu \left[(1 - \beta \mathcal{A}_{ji}^{[t_n]}) \prod_{\substack{k \in V \\ k \neq j}} \left(1 - \beta \mathcal{A}_{ki}^{[t_n]} \frac{P_{S_i, I_k}(t_n)}{P_{S_i}(t_n)} \right) \right] \quad (\text{A.5})$$

$$W_{I_i, R_j | S_i I_j}(t_n) = \mu \left[1 - (1 - \beta \mathcal{A}_{ji}^{[t_n]}) \prod_{\substack{k \in V \\ k \neq j}} \left(1 - \beta \mathcal{A}_{ki}^{[t_n]} \frac{P_{S_i, I_k}(t_n)}{P_{S_i}(t_n)} \right) \right] \quad (\text{A.6})$$

Acknowledgements

I would like to offer my undying gratitude my two supervisors Dr. Philipp Hövel and Dr. Kieran Mulchrone for being truly amazing. They were endless sources of positivity and understanding even when things got difficult. Much of this Ph.D. was completed during the many lock-downs of COVID-19 and without the two of them supporting my work, I may not have made it to the finish line.

To my parents Lisa and Fergus, I would like to thank them for convincing me to undertake this venture and continuing to support me the whole way through. The four years was worth it if it was just to make them proud.

Last but not least, I would like to thank my partner Seán who has put up with me through thick and thin. His unwavering support throughout this Ph.D. was critical in seeing me reach the other side, and so, I dedicate this thesis to him. I can't thank you enough Seán.

List of Publications

- Kearney, P. M. et al. Compliance with local travel restrictions and face masks during first phase of COVID-19 pandemic in Ireland: a national survey. *Journal of public health (Oxford, England)* fdac017–fdac017 (2022).
- Humphries, R., Mulchrone, K., Tratalos, J., More, S. J. & Hövel, P. A systematic framework of modelling epidemics on temporal networks. *Appl Netw Sci* 6, 23 (2021).
- Galler, M., Lüdge, K., Humphries, R., Mulchrone, K. & Hövel, P. Deterministic and stochastic effects in spreading dynamics: A case study of bovine viral diarrhea. *Chaos* 31, 093129 (2021).
- Troya, M. I. et al. HRB Open Research. (2021).
- Troya, M. I. et al. Mental health following an initial period of COVID-19 restrictions: findings from a cross-sectional survey in the Republic of Ireland. *HRB open research* 4, (2021).
- Humphries, R. et al. A metapopulation network model for the spreading of SARS-CoV-2: Case study for Ireland. *Infectious Disease Modelling* 6, 420–437 (2021).
- Troya, M. I. et al. Covid-19 Estimating the burden of symptomatic disease in the community and the impact of public health measures on physical, mental and social wellbeing: a study protocol. *HRB Open Research* 3, (2020).

Bibliography

1. Adamic, L. A. *The Small World Web* in. International Conference on Theory and Practice of Digital Libraries (Springer, 1999), 443–452.
2. Adkin, A. *et al.* Development of Risk-Based Trading Farm Scoring System to Assist with the Control of Bovine Tuberculosis in Cattle in England and Wales. *Preventive Veterinary Medicine* **123**, 32–38. ISSN: 0167-5877 (Jan. 1, 2016).
3. Ajelli, M. *et al.* Comparing Large-Scale Computational Approaches to Epidemic Modeling: Agent-based versus Structured Metapopulation Models. *BMC Infectious Diseases* **10**, 1–13. ISSN: 1471-2334 (1 Dec. 2010).
4. Albert, R. & Barabási, A.-L. Statistical Mechanics of Complex Networks. *Reviews of Modern Physics* **74**, 47–97 (Jan. 30, 2002).
5. Ali, M., Shah, S. T. H., Imran, M. & Khan, A. The Role of Asymptomatic Class, Quarantine and Isolation in the Transmission of COVID-19. *Journal of Biological Dynamics* **14**, 389–408. ISSN: 1751-3758, 1751-3766 (Jan. 1, 2020).
6. Alis, C., Legara, E. F. & Monterola, C. Generalized Radiation Model for Human Migration. *Scientific Reports* **11**, 22707. ISSN: 2045-2322 (1 Nov. 22, 2021).
7. Alwan, N. A. *et al.* Scientific Consensus on the COVID-19 Pandemic: We Need to Act Now. *The Lancet* **396**, e71–e72 (2020).
8. Amann, A. *How to Choose the Best Strategy for Fighting an Infectious Disease* private communication. 2020.

BIBLIOGRAPHY

9. Ames, A. D., Molnar, T. G., Singletary, A. W. & Orosz, G. Safety-Critical Control of Active Interventions for COVID-19 Mitigation. *medRxiv* (2020).
10. Anderson, R. & May, R. *Infectious Diseases of Humans: Dynamics and Control* (1991).
11. *Background - NUTS - Nomenclature of Territorial Units for Statistics - Eurostat* <https://ec.europa.eu/eurostat/web/nuts/background> (2022).
12. Bajardi, P., Barrat, A., Natale, F., Savini, L. & Colizza, V. Dynamical Patterns of Cattle Trade Movements. *PLOS ONE* **6**, e19869. ISSN: 1932-6203 (May 18, 2011).
13. Balcan, D. *et al.* Multiscale Mobility Networks and the Spatial Spreading of Infectious Diseases. *Proceedings of the National Academy of Sciences* **106**, 21484–21489. ISSN: 0027-8424, 1091-6490 (Dec. 22, 2009).
14. Banisch, S. & Olbrich, E. Opinion Polarization by Learning from Social Feedback. *The Journal of Mathematical Sociology* **43**, 76–103. ISSN: 0022-250X, 1545-5874 (Apr. 2019).
15. Bansal, S., Read, J., Pourbohloul, B. & Meyers, L. A. The Dynamic Nature of Contact Networks in Infectious Disease Epidemiology. *Journal of Biological Dynamics* **4**, 478–489. ISSN: 1751-3758. pmid: 22877143 (Sept. 1, 2010).
16. Barabási, A. Emergence of Scaling in Random Networks. *Science* **286**, 509–512. ISSN: 00368075, 10959203 (Oct. 1999).
17. Barabási, A.-L. Scale-Free Networks: A Decade and Beyond. *science* **325**, 412–413. ISSN: 0036-8075 (2009).
18. Barabási, A.-L. & Pósfai, M. *Network Science* 456 pp. ISBN: 978-1-107-07626-6 (Cambridge University Press, Cambridge, United Kingdom, 2016).
19. Barbosa, H. *et al.* Human Mobility: Models and Applications. *Physics Reports* **734**, 1–74. ISSN: 03701573 (Mar. 2018).

20. Barrett, D. J. *et al.* Considerations on BVD Eradication for the Irish Livestock Industry. *Irish Veterinary Journal* **64**, 12. ISSN: 2046-0481 (Oct. 3, 2011).
21. Bavelas, A. Communication Patterns in Task-Oriented Groups. *The Journal of the Acoustical Society of America* **22**, 725–730. ISSN: 0001-4966 (Nov. 1950).
22. Belik, V., Geisel, T. & Brockmann, D. Natural Human Mobility Patterns and Spatial Spread of Infectious Diseases. *Physical Review X* **1**, 011001. ISSN: 2160-3308 (Aug. 2011).
23. Bell, D. C., Atkinson, J. S. & Carlson, J. W. Centrality Measures for Disease Transmission Networks. *Social Networks* **21**, 1–21. ISSN: 0378-8733 (Jan. 1, 1999).
24. Beverton, R. J. & Holt, S. J. *On the Dynamics of Exploited Fish Populations* (Springer Science & Business Media, 1993).
25. Bianconi, G. *Multilayer Networks: Structure and Function* First edition. ISBN: 978-0-19-875391-9 (Oxford University Press, Oxford, 2018).
26. Blackwood, J. & Childs, L. An Introduction to Compartmental Modeling for the Budding Infectious Disease Modeler. *Letters in Biomathematics* **5**. ISSN: 23737867 (2018).
27. Blyuss, K. B. & Kyrychko, Y. N. Effects of Latency and Age Structure on the Dynamics and Containment of COVID-19. *medRxiv* (2020).
28. Bondy, J. A. & Murty, U. S. R. *Graph Theory Graduate Texts in Mathematics* **244**. 651 pp. ISBN: 978-1-84628-969-9 (Springer, New York, 2008).
29. Brockmann, D. & Hufnagel, L. Front Propagation in Reaction-Superdiffusion Dynamics: Taming Lévy Flights with Fluctuations. *Physical Review Letters* **98**, 178301. ISSN: 0031-9007, 1079-7114 (Apr. 2007).
30. Brockmann, D., Hufnagel, L. & Geisel, T. The Scaling Laws of Human Travel. *Nature* **439**, 462–465. ISSN: 0028-0836, 1476-4687 (Jan. 2006).
31. Brockmann, D. & Helbing, D. The Hidden Geometry of Complex, Network-Driven Contagion Phenomena. *Science* **342**, 1337–1342 (Dec. 13, 2013).

BIBLIOGRAPHY

32. Broughan, J. M. *et al.* A Review of Risk Factors for Bovine Tuberculosis Infection in Cattle in the UK and Ireland. *Epidemiology and Infection* **144**, 2899–2926. ISSN: 0950-2688, 1469-4409 (Oct. 2016).
33. Burger, M., van Oort, F. & Linders, G.-J. On the Specification of the Gravity Model of Trade: Zeros, Excess Zeros and Zero-inflated Estimation. *Spatial Economic Analysis* **4**, 167–190. ISSN: 1742-1772, 1742-1780 (June 2009).
34. Byrne, A. W. *et al.* Inferred Duration of Infectious Period of SARS-CoV-2: Rapid Scoping Review and Analysis of Available Evidence for Asymptomatic and Symptomatic COVID-19 Cases. *BMJ Open* **10**, e039856. ISSN: 2044-6055, 2044-6055 (Aug. 2020).
35. Carey, H. *Principles of Social Science Principles of Social Science v. 3* (J.B. Lippincott & Company, 1859).
36. *Census 2016 Profile 6 - Commuting in Ireland - CSO - Central Statistics Office* <https://www.cso.ie/en/csolatestnews/presspages/2017/census2016profile6-commutinginireland/> (2022).
37. Chasnov, J. R. Mathematical Biology, 115.
38. Chen, N. *et al.* Epidemiological and Clinical Characteristics of 99 Cases of 2019 Novel Coronavirus Pneumonia in Wuhan, China: A Descriptive Study. *The Lancet* **395**, 507–513 (2020).
39. Chowdhury, R. *et al.* Dynamic Interventions to Control COVID-19 Pandemic: A Multivariate Prediction Modelling Study Comparing 16 World-wide Countries. *Eur. J. Epidemiol.* **35**, 389–399 (2020).
40. Christensen, V. & Walters, C. J. Ecopath with Ecosim: Methods, Capabilities and Limitations. *Ecol. Modell.* **172**, 109–139 (2004).
41. Colizza, V., Barrat, A., Barthélemy, M. & Vespignani, A. The Role of the Airline Transportation Network in the Prediction and Predictability of Global Epidemics. *Proceedings of the National Academy of Sciences* **103**, 2015–2020. ISSN: 0027-8424, 1091-6490 (Feb. 14, 2006).

42. Colizza, V., Pastor-Satorras, R. & Vespignani, A. Reaction–Diffusion Processes and Metapopulation Models in Heterogeneous Networks. *Nature Physics* **3**, 276–282 (2007).
43. Colizza, V. & Vespignani, A. Invasion Threshold in Heterogeneous Metapopulation Networks. *Physical Review Letters* **99**, 148701. ISSN: 0031-9007, 1079-7114 (Oct. 5, 2007).
44. *Coronavirus Disease 2019 (COVID-19) Situation Report – 51* 51 (World Health Organisation, Mar. 11, 2020). <https://www.who.int/docs/default-source/coronaviruse/situation-reports/20200311-sitrep-51-covid-19.pdf>.
45. Costelloe, J., Gaynor, M., Gaynor, S., Mcateer, W. & O'Reilly, P. Control of Foot and Mouth Disease: Lessons from the Experience of Ireland: -EN- -FR- -ES-. *Revue Scientifique et Technique de l'OIE* **21**, 739–750. ISSN: 0253-1933 (Dec. 1, 2002).
46. *COVID Live - Coronavirus Statistics - Worldometer* <https://www.worldometers.info/coronavirus/> (2022).
47. *COVID-19 HPSC Detailed Statistics Profile - Data.Gov.Ie* <https://data.gov.ie/dataset/covid-19-hpsc-detailed-statistics-profile1> (2022).
48. *COVID-19 IHR Emergency Committee* <https://www.who.int/teams/ihr/ihr-emergency-committees/covid-19-ihr-emergency-committee> (2022).
49. *COVID-19 Laboratory Testing Time Series - Data.Gov.Ie* <https://data.gov.ie/dataset/covid-19-laboratory-testing-time-series> (2022).
50. Covid-19 Vaccine Tracker. <https://www.bloomberg.com/graphics/covid-vaccine-tracker-global-distribution/> (2021).
51. Crossley, N. Small-World Networks, Complex Systems and Sociology. *Sociology* **42**, 261–277. ISSN: 0038-0385, 1469-8684 (Apr. 2008).

- 52. D’Onofrio, A., Manfredi, P. & Salinelli, E. Vaccinating Behaviour, Information, and the Dynamics of SIR Vaccine Preventable Diseases. *Theoretical Population Biology* **71**, 301–317. ISSN: 00405809 (May 2007).
- 53. Davies, N. G. *et al.* Age-Dependent Effects in the Transmission and Control of COVID-19 Epidemics. *Nature Medicine* **26**, 1205–1211. ISSN: 1546-170X (8 Aug. 2020).
- 54. Diekmann, O., Heesterbeek, J. A. P. & Roberts, M. G. The Construction of Next-Generation Matrices for Compartmental Epidemic Models. *Journal of The Royal Society Interface* **7**, 873–885. ISSN: 1742-5689, 1742-5662 (June 6, 2010).
- 55. Douglas, M., Katikireddi, S. V., Taulbut, M., McKee, M. & McCartney, G. Mitigating the Wider Health Effects of COVID-19 Pandemic Response. *BMJ* **369**, m1557 (2020).
- 56. Duncan-Jones, R. P. The Impact of the Antonine Plague. *Journal of Roman Archaeology* **9**, 108–136. ISSN: 1047-7594, 2331-5709 (1996/ed).
- 57. Eckmann, J. *et al.* The Physics of Living Neural Networks. *Physics Reports* **449**, 54–76. ISSN: 03701573 (Sept. 2007).
- 58. *Electoral Divisions - CSO Generalised 20m* https://census2016.geohive.ie/datasets/774b6c87f0ec49c48e0e7999fc0e752b_1 (2022).
- 59. Elias, C., Sekri, A., Leblanc, P., Cucherat, M. & Vanhems, P. The Incubation Period of COVID-19: A Meta-Analysis. *International Journal of Infectious Diseases* **104**, 708–710. ISSN: 12019712 (Mar. 2021).
- 60. Erdos, P. & Rényi, A. On the Evolution of Random Graphs. *Publ. Math. Inst. Hung. Acad. Sci* **5**, 17–60 (1960).
- 61. Erdős, P. & Rényi, A. On the Strength of Connectedness of a Random Graph. *Acta Mathematica Academiae Scientiarum Hungaricae* **12**, 261–267. ISSN: 0001-5954 (Mar. 1964).
- 62. Erdős, P. & Rényi, A. On the Existence of a Factor of Degree One of a Connected Random Graph. *Acta Mathematica Academiae Scientiarum Hungaricae* **17**, 359–368. ISSN: 0001-5954, 1588-2632 (Sept. 1966).

- 63. Euler, L. Solutio Problematis Ad Geometriam Situs Pertinentis. *Commentarii academiae scientiarum Petropolitanae*, 128–140 (1741).
- 64. Ferguson, N. M., Donnelly, C. A. & Anderson, R. M. Transmission Intensity and Impact of Control Policies on the Foot and Mouth Epidemic in Great Britain. *Nature* **413**, 542–548. ISSN: 1476-4687 (6855 Oct. 2001).
- 65. Fisher, R. A. The Wave of Advance of Advantageous Genes. *Annals of Eugenics* **7**, 355–369. ISSN: 2050-1439 (1937).
- 66. Fleurence, R. L. & Hollenbeak, C. S. Rates and Probabilities in Economic Modelling: Transformation, Translation and Appropriate Application. *Pharmacoeconomics* **25**, 3–6. ISSN: 1170-7690 (2007).
- 67. Fotheringham, A. S. Some Theoretical Aspects of Destination Choice and Their Relevance to Production-Constrained Gravity Models. *Environment and Planning A: Economy and Space* **15**, 1121–1132. ISSN: 0308-518X (Aug. 1, 1983).
- 68. Frasca, M. & Sharkey, K. J. Discrete-Time Moment Closure Models for Epidemic Spreading in Populations of Interacting Individuals. *J. Theor. Biol.* **399**, 13–21. ISSN: 00225193 (June 2016).
- 69. Freeman, L. C. A Set of Measures of Centrality Based on Betweenness. *Sociometry* **40**, 35. ISSN: 00380431 (Mar. 1977).
- 70. Freeman, L. C. Centrality in Social Networks Conceptual Clarification. *Social Networks* **1**, 215–239. ISSN: 03788733 (Jan. 1978).
- 71. Frias-Martinez, V., Soguero, C. & Frias-Martinez, E. *Estimation of Urban Commuting Patterns Using Cellphone Network Data* in *Proceedings of the ACM SIGKDD International Workshop on Urban Computing* (Association for Computing Machinery, New York, NY, USA, Aug. 12, 2012), 9–16. ISBN: 978-1-4503-1542-5.
- 72. Galler, M., Lüdge, K., Humphries, R., Mulchrone, K. & Hövel, P. Deterministic and Stochastic Effects in Spreading Dynamics: A Case Study of Bovine Viral Diarrhea. *Chaos: An Interdisciplinary Journal of Nonlinear Science* **31**, 093129. ISSN: 1054-1500 (Sept. 2021).

- 73. Gardiner, C. W. & Gardiner, C. W. *Stochastic Methods: A Handbook for the Natural and Social Sciences* 4th ed. ISBN: 978-3-540-70712-7 (Springer, Berlin, 2009).
- 74. Garske, T. *et al.* Travel Patterns in China. *PLoS ONE* **6** (ed Jones, J.) e16364. ISSN: 1932-6203 (Feb. 2, 2011).
- 75. Géniois, M. & Barrat, A. Can Co-Location Be Used as a Proxy for Face-to-Face Contacts? *EPJ Data Science* **7**, 11. ISSN: 2193-1127 (Dec. 2018).
- 76. Gethmann, J. *et al.* An Epidemiological and Economic Simulation Model to Evaluate Strategies for the Control of Bovine Virus Diarrhea in Germany. **6**, 406 (2019).
- 77. Girvan, M. & Newman, M. E. J. Community Structure in Social and Biological Networks. *Proceedings of the National Academy of Sciences* **99**, 7821–7826. ISSN: 0027-8424, 1091-6490 (June 11, 2002).
- 78. Gleeson, J. P. Binary-State Dynamics on Complex Networks: Pair Approximation and Beyond. *Physical Review X* **3**, 021004. ISSN: 2160-3308 (Apr. 29, 2013).
- 79. Gómez, S., Arenas, A., Borge-Holthoefer, J., Meloni, S. & Moreno, Y. Discrete-Time Markov Chain Approach to Contact-Based Disease Spreading in Complex Networks. *EPL (Europhysics Letters)* **89**, 38009. ISSN: 0295-5075, 1286-4854 (Feb. 2010).
- 80. Good, M. *et al.* Prevalence and Distribution of Paratuberculosis (Johne's Disease) in Cattle Herds in Ireland. *Irish Veterinary Journal* **62**, 597. ISSN: 2046-0481 (Sept. 1, 2009).
- 81. Grassberger, P. On the Critical Behavior of the General Epidemic Process and Dynamical Percolation. *Mathematical Biosciences* **63**, 157–172. ISSN: 0025-5564 (Apr. 1, 1983).
- 82. Grauwin, S. *et al.* Identifying and Modeling the Structural Discontinuities of Human Interactions. *Sci. Rep.* **7**, 46677 (2017).

- 83. Griffin, J. M. & O'Reilly, P. J. Epidemiology and Control of an Outbreak of Foot-and-Mouth Disease in the Republic of Ireland in 2001. *Veterinary Record* **152**, 705–712. ISSN: 00424900 (June 2003).
- 84. Griffith, D. A. Constrained Variants of the Gravity Model and Spatial Dependence: Model Specification and Estimation Issues, 33.
- 85. Gross, T., D'Lima, C. J. D. & Blasius, B. Epidemic Dynamics on an Adaptive Network. *Physical Review Letters* **96**, 208701. ISSN: 0031-9007, 1079-7114 (May 2006).
- 86. Hanski, I. A Practical Model of Metapopulation Dynamics. *Journal of Animal Ecology* **63**, 151–162. ISSN: 0021-8790 (1994).
- 87. Hanski, I. Metapopulation Dynamics. *Nature* **396**, 41–49. ISSN: 1476-4687 (6706 Nov. 1998).
- 88. Haydon, D. T., Kao, R. R. & Kitching, R. P. The UK Foot-and-Mouth Disease Outbreak — the Aftermath. *Nature Reviews Microbiology* **2**, 675–681. ISSN: 1740-1534 (8 Aug. 2004).
- 89. Haynes, K. E. & Fotheringham, A. S. *Gravity and Spatial Interaction Models* (Regional Research Institute, West Virginia University, 2020).
- 90. He, S., Peng, Y. & Sun, K. SEIR Modeling of the COVID-19 and Its Dynamics. *Nonlinear Dynamics* **101**, 1667–1680. ISSN: 0924-090X, 1573-269X (Aug. 2020).
- 91. Henderson, D. A. The Eradication of Smallpox – An Overview of the Past, Present, and Future. *Vaccine. Smallpox Eradication after 30 Years: Lessons, Legacies and Innovations* **29**, D7–D9. ISSN: 0264-410X (Dec. 30, 2011).
- 92. Hines, P. & Blumsack, S. A Centrality Measure for Electrical Networks in *Proceedings of the 41st Annual Hawaii International Conference on System Sciences (HICSS 2008)* 2008 41st Annual Hawaii International Conference on System Sciences (IEEE, Waikoloa, HI, Jan. 2008), 185–185.
- 93. Holme, P. & Saramäki, J. Temporal Networks. *Physics Reports. Temporal Networks* **519**, 97–125. ISSN: 0370-1573 (Oct. 1, 2012).

BIBLIOGRAPHY

94. Hong, I., Jung, W.-S. & Jo, H.-H. Gravity Model Explained by the Radiation Model on a Population Landscape. *PLOS ONE* **14** (ed Gallotti, R.) e0218028. ISSN: 1932-6203 (June 6, 2019).
95. House, T. & Keeling, M. J. Deterministic Epidemic Models with Explicit Household Structure. *Mathematical biosciences* **213**, 29–39. ISSN: 0025-5564 (2008).
96. Hövel, P., Viol, A., Loske, P., Merfort, L. & Vuksanović, V. Synchronization in Functional Networks of the Human Brain. *Journal of Nonlinear Science* **30**, 2259–2282. ISSN: 0938-8974, 1432-1467 (Oct. 2020).
97. Humphries, R. *EpiGraph* GitHub, 2020. <https://github.com/rory-humphries/EpiGraph-cpp>.
98. Humphries, R., Mulchrone, K., Tratalos, J., More, S. J. & Hövel, P. A Systematic Framework of Modelling Epidemics on Temporal Networks. *Applied Network Science* **6**, 23. ISSN: 2364-8228 (Dec. 2021).
99. Humphries, R. *et al.* A Metapopulation Network Model for the Spreading of SARS-CoV-2: Case Study for Ireland. *Infectious Disease Modelling* **6**, 420–437. ISSN: 2468-0427 (Jan. 1, 2021).
100. Iannelli, F., Koher, A., Brockmann, D., Hövel, P. & Sokolov, I. M. Effective Distances for Epidemics Spreading on Complex Networks. *Phys. Rev. E* **95**, 012313 (Jan. 2017).
101. *Information Note on the Implications of COVID-19 on the Processing of Death Certificates - CSO - Central Statistics Office* <https://www.cso.ie/en/releasesandpublications/in/vs/informationnoteontheimplicationsofcovid-19ontheprocessingofdeathcertificates/> (2022).
102. Ings, T. C. *et al.* Review: Ecological Networks - beyond Food Webs. *Journal of Animal Ecology* **78**, 253–269. ISSN: 00218790, 13652656 (Jan. 2009).
103. *Ireland's COVID-19 Data Hub* <https://covid19ireland-geohive.hub.arcgis.com/> (2022).

104. *Irish Horticulture Industry - Bord Bia - Irish Food Board* <https://www.bordbia.ie/industry/irish-sector-profiles/irish-agriculture-food-drink-sector/> (2022).
105. Kang, C., Liu, Y., Guo, D. & Qin, K. A Generalized Radiation Model for Human Mobility: Spatial Scale, Searching Direction and Trip Constraint. *PLOS ONE* **10**, e0143500. ISSN: 1932-6203 (Nov. 24, 2015).
106. Karrer, B. & Newman, M. E. J. Message Passing Approach for General Epidemic Models. *Phys. Rev. E* **82**, 016101. ISSN: 1539-3755, 1550-2376 (July 2010).
107. Katz, L. A New Status Index Derived from Sociometric Analysis. *Psychometrika* **18**, 39–43. ISSN: 0033-3123, 1860-0980 (Mar. 1953).
108. Kearney, P. M. *et al.* Compliance with Local Travel Restrictions and Face Masks during First Phase of COVID-19 Pandemic in Ireland: A National Survey. *Journal of Public Health*, fdac017. ISSN: 1741-3842, 1741-3850 (Mar. 14, 2022).
109. Keeling, M. J., Danon, L., Vernon, M. C. & House, T. A. Individual Identity and Movement Networks for Disease Metapopulations. *Proceedings of the National Academy of Sciences* **107**, 8866–8870 (May 11, 2010).
110. Keeling, M. J. & Eames, K. T. D. Networks and Epidemic Models. *Journal of The Royal Society Interface* **2**, 295–307 (June 2005).
111. Kermack, W. O. & McKendrick, A. G. A Contribution to the Mathematical Theory of Epidemics. **115**, 700–721 (1927).
112. Al-Khani, A. M., Khalifa, M. A., AlMazrou, A. & Saquib, N. The SARS-CoV-2 Pandemic Course in Saudi Arabia: A Dynamic Epidemiological Model. *Infectious Disease Modelling* **5**, 766–771 (2020).
113. Killeen, G. F. & Kiware, S. S. Why Lockdown? Why National Unity? Why Global Solidarity? Simplified Arithmetic Tools for Decision-Makers, Health Professionals, Journalists and the General Public to Explore Containment Options for the 2019 Novel Coronavirus. *Infectious Disease Modelling* **5**, 442–458. ISSN: 2468-0427 (Jan. 1, 2020).

BIBLIOGRAPHY

- 114. Kirkwood, J. G. Statistical Mechanics of Fluid Mixtures. *J. Chem. Phys.* **3**, 300–313. ISSN: 0021-9606, 1089-7690 (May 1935).
- 115. Kissler, S. M., Tedijanto, C., Goldstein, E., Grad, Y. H. & Lipsitch, M. Projecting the Transmission Dynamics of ARS-CoV-2 through the Post-pandemic Period. *Science* **368**, 860–868 (2020).
- 116. Koher, A., Lentz, H. H. K., Hövel, P. & Sokolov, I. M. Infections on Temporal Networks - A Matrix-Based Approach. *PLOS ONE* **11**, e0151209 (Apr. 2016).
- 117. Koher, A., Lentz, H. H., Gleeson, J. P. & Hövel, P. Contact-Based Model for Epidemic Spreading on Temporal Networks. *Phys. Rev. X* **9**, 031017. ISSN: 2160-3308 (Aug. 2019).
- 118. Kotsubo, M. & Nakaya, T. Kernel-Based Formulation of Intervening Opportunities for Spatial Interaction Modelling. *Scientific Reports* **11**, 950. ISSN: 2045-2322 (Dec. 2021).
- 119. Kyrychko, Y. N., Blyuss, K. B. & Brovchenko, I. Mathematical Modelling of the Dynamics and Containment of COVID-19 in Ukraine. *Sci. Rep.* **10**, 19662 (2020).
- 120. Lax, P. D. *Functional Analysis* 580 pp. ISBN: 978-0-471-55604-6 (Wiley, New York, 2002).
- 121. Lee, J., Choi, B. Y. & Jung, E. Metapopulation Model Using Commuting Flow for National Spread of the 2009 H1N1 Influenza Virus in the Republic of Korea. *Journal of Theoretical Biology* **454**, 320–329. ISSN: 0022-5193 (Oct. 7, 2018).
- 122. Lentz, H. H. K., Selhorst, T. & Sokolov, I. M. Unfolding Accessibility Provides a Macroscopic Approach to Temporal Networks. *Physical Review Letters* **110**, 118701. ISSN: 0031-9007, 1079-7114 (Mar. 2013).
- 123. Lentz, H. H. K. *et al.* Disease Spread through Animal Movements: A Static and Temporal Network Analysis of Pig Trade in Germany. *PLOS ONE* **11**, e0155196. ISSN: 1932-6203 (May 6, 2016).

- 124. Li, M. Y. & Muldowney, J. S. Global Stability for the SEIR Model in Epidemiology. *Mathematical Biosciences* **125**, 155–164. ISSN: 00255564 (Feb. 1995).
- 125. Li, S. *et al.* A Map of the Interactome Network of the Metazoan *C. Elegans*. *Science* **303**, 540–543. ISSN: 0036-8075, 1095-9203 (Jan. 23, 2004).
- 126. Little, R., Wheeler, K. & Edge, S. Developing a Risk-Based Trading Scheme for Cattle in England: Farmer Perspectives on Managing Trading Risk for Bovine Tuberculosis. *Veterinary Record* **180**, 148–148. ISSN: 00424900 (Feb. 2017).
- 127. Liu, E. & Yan, X. New Parameter-Free Mobility Model: Opportunity Priority Selection Model. *Physica A: Statistical Mechanics and its Applications* **526**, 121023. ISSN: 0378-4371 (July 15, 2019).
- 128. Liu, H., Chen, Y.-H. & Lih, J.-S. Crossover from Exponential to Power-Law Scaling for Human Mobility Pattern in Urban, Suburban and Rural Areas. *The European Physical Journal B* **88**, 117. ISSN: 1434-6028, 1434-6036 (May 2015).
- 129. Liu, E.-J. & Yan, X.-Y. A Universal Opportunity Model for Human Mobility. *Scientific Reports* **10**, 4657. ISSN: 2045-2322 (1 Mar. 13, 2020).
- 130. Liu, Z., Magal, P., Seydi, O. & Webb, G. A COVID-19 Epidemic Model with Latency Period. *Infectious Disease Modelling* **5**, 323–337 (2020).
- 131. Luce, R. D. A Note on Boolean Matrix Theory. *Proceedings of the American Mathematical Society* **3**, 382–388. ISSN: 0002-9939 (1952).
- 132. Maier, B. F. & Brockmann, D. Effective Containment Explains Subexponential Growth in Recent Confirmed COVID-19 Cases in China. *Science* **368**, 742–746 (2020).
- 133. Marschner, I. C. Estimating Age-Specific COVID-19 Fatality Risk and Time to Death by Comparing Population Diagnosis and Death Patterns: Australian Data. *BMC Medical Research Methodology* **21**, 126. ISSN: 1471-2288 (Dec. 2021).

BIBLIOGRAPHY

- 134. Masucci, A. P., Serras, J., Johansson, A. & Batty, M. Gravity versus Radiation Models: On the Importance of Scale and Heterogeneity in Commuting Flows. *Physical Review E* **88**, 022812. ISSN: 1539-3755, 1550-2376 (Aug. 22, 2013).
- 135. Masuda, N. & Holme, P. *Temporal Network Epidemiology* (Springer, 2017).
- 136. Matyas, L. Proper Econometric Specification of the Gravity Model. *The World Economy* **20**, 363–368. ISSN: 0378-5920, 1467-9701 (May 1997).
- 137. McAloon, C. G. *et al.* Individual and Herd-Level Milk ELISA Test Status for Johne’s Disease in Ireland after Correcting for Non-Disease-Associated Variables. *Journal of Dairy Science* **103**, 9345–9354. ISSN: 0022-0302 (Oct. 1, 2020).
- 138. McGrath, G., Tratalos, J. A. & More, S. J. A Visual Representation of Cattle Movement in Ireland during 2016. *Irish Veterinary Journal* **71**, 18. ISSN: 2046-0481 (Dec. 2018).
- 139. Mollison, D. Spatial Contact Models for Ecological and Epidemic Spread. *Journal of the Royal Statistical Society: Series B (Methodological)* **39**, 283–313. ISSN: 2517-6161 (1977).
- 140. Moore, C. & Newman, M. E. J. Epidemics and Percolation in Small-World Networks. *Physical Review E* **61**, 5678–5682 (May 1, 2000).
- 141. More, S. J., Radunz, B. & Glanville, R. J. Lessons Learned during the Successful Eradication of Bovine Tuberculosis from Australia. *Veterinary Record* **177**, 224–232. ISSN: 2042-7670 (2015).
- 142. More, S. J. Can Bovine TB Be Eradicated from the Republic of Ireland? Could This Be Achieved by 2030? *Irish Veterinary Journal* **72**, 3. ISSN: 2046-0481 (Dec. 2019).
- 143. Motta, P. *et al.* Implications of the Cattle Trade Network in Cameroon for Regional Disease Prevention and Control. *Scientific Reports* **7**, 43932. ISSN: 2045-2322 (1 Mar. 7, 2017).
- 144. Newman, M. E. J. Spread of Epidemic Disease on Networks. *Physical Review E* **66**, 016128. ISSN: 1063-651X, 1095-3787 (July 26, 2002).

- 145. Newman, M. E. J. *Networks* Second edition. 780 pp. ISBN: 978-0-19-880509-0 (Oxford University Press, Oxford, United Kingdom ; New York, NY, United States of America, 2018).
- 146. Nguyen, G. H. *et al.* *Continuous-Time Dynamic Network Embeddings in Companion of the The Web Conference 2018 on The Web Conference 2018 - WWW '18* Companion of the The Web Conference 2018 (ACM Press, Lyon, France, 2018), 969–976. ISBN: 978-1-4503-5640-4.
- 147. *Northern Ireland Local Government Districts* Northern Ireland Statistics and Research Agency. <https://www.nisra.gov.uk/statistics/regional-analysis-and-trends/local-government-district> (2022).
- 148. *Novel Coronavirus(2019-nCoV) Situation Report - 10* 10 (World Health Organisation, Jan. 30, 2020). <https://www.who.int/docs/default-source/coronaviruse/situation-reports/20200130-sitrep-10-ncov.pdf>.
- 149. NPHET Policy Unit. *Timeline and Detail of Public Health Restrictive Measures Advised by NPHET in Response to the COVID-19 Pandemic* (Department of Health, Government of Ireland, Jan. 13, 21). <https://assets.gov.ie/126580/471f8ed0-1ef3-4e0a-a498-5d0dc027fc2d.pdf> (2022).
- 150. Ortiz-Pelaez, A., Pfeiffer, D. U., Soares-Magalhães, R. J. & Guitian, F. J. Use of Social Network Analysis to Characterize the Pattern of Animal Movements in the Initial Phases of the 2001 Foot and Mouth Disease (FMD) Epidemic in the UK. *Preventive Veterinary Medicine* **76**, 40–55. ISSN: 0167-5877 (Sept. 15, 2006).
- 151. Page, L., Brin, S., Motwani, R. & Winograd, T. The PageRank Citation Ranking: Bringing Order to the Web (1999).
- 152. Pappalardo, L., Rinzivillo, S. & Simini, F. Human Mobility Modelling: Exploration and Preferential Return Meet the Gravity Model. *Procedia Computer Science. The 7th International Conference on Ambient Systems, Networks and Technologies (ANT 2016) / The 6th International Conference on Sustainable Energy Information Technology (SEIT-2016) / Affiliated Workshops* **83**, 934–939. ISSN: 1877-0509 (Jan. 1, 2016).

- 153. Paranjape, A., Benson, A. R. & Leskovec, J. *Motifs in Temporal Networks* in *Proceedings of the Tenth ACM International Conference on Web Search and Data Mining* (Association for Computing Machinery, New York, NY, USA, Feb. 2, 2017), 601–610. ISBN: 978-1-4503-4675-7.
- 154. Pinotti, F. *et al.* Tracing and Analysis of 288 Early SARS-CoV-2 Infections Outside China: A Modeling Study. *PLOS Med.* **17**, e1003193 (2020).
- 155. Porojan, A. Trade Flows and Spatial Effects: The Gravity Model Revisited, 16 (2001).
- 156. Porter, M. A., Onnela, J.-P. & Mucha, P. J. Communities in Networks. *Notices of the AMS* **56**, 1082–1097 (2009).
- 157. Prem, K. *et al.* The Effect of Control Strategies to Reduce Social Mixing on Outcomes of the COVID-19 Epidemic in Wuhan, China: A Modelling Study. *The Lancet Public Health* **5**, e261–e270 (2020).
- 158. Pullano, G., Valdano, E., Scarpa, N., Rubrichi, S. & Colizza, V. Evaluating the Effect of Demographic Factors, Socioeconomic Factors, and Risk Aversion on Mobility during the COVID-19 Epidemic in France under Lock-down: A Population-Based Study. *The Lancet Digital Health* **2**, e638–e649 (2020).
- 159. Rautureau, S., Dufour, B. & Durand, B. Vulnerability of Animal Trade Networks to The Spread of Infectious Diseases: A Methodological Approach Applied to Evaluation and Emergency Control Strategies in Cattle, France, 2005: Vulnerability of Animal Trade Networks to The Spread of Infectious Diseases. *Transboundary and Emerging Diseases* **58**, 110–120. ISSN: 18651674 (Apr. 2011).
- 160. Ren, Y., Ercsey-Ravasz, M., Wang, P., González, M. C. & Toroczkai, Z. Predicting Commuter Flows in Spatial Networks Using a Radiation Model Based on Temporal Ranges. *Nature Communications* **5**, 5347. ISSN: 2041-1723 (1 Nov. 6, 2014).

- 161. Riccardo, F. *et al.* Epidemiological Characteristics of COVID-19 Cases and Estimates of the Reproductive Numbers 1 Month into the Epidemic, Italy, 28 January to 31 March 2020. *Eurosurveillance* **25**, 2000790. ISSN: 1560-7917 (Dec. 10, 2020).
- 162. *Roadmap for Reopening Society and Business* <https://www.gov.ie/en/news/58bc8b-taoiseach-announces-roadmap-for-reopening-society-and-business-and-u/> (2022).
- 163. Roser, M. & Ritchie, H. Burden of Disease. *Our World in Data*. <https://ourworldindata.org/burden-of-disease> (2022) (Sept. 25, 2021).
- 164. Rybski, D., Buldyrev, S. V., Havlin, S., Liljeros, F. & Makse, H. A. Communication Activity in a Social Network: Relation between Long-Term Correlations and Inter-Event Clustering. *Scientific Reports* **2**, 560. ISSN: 2045-2322 (1 Aug. 6, 2012).
- 165. Sabbatani, S. & Fiorino, S. The Antonine Plague and the decline of the Roman Empire. *Le Infezioni in Medicina* **17**, 261–275. ISSN: 1124-9390. pmid: 20046111 (Dec. 2009).
- 166. Schaller, R. Moore’s Law: Past, Present and Future. *IEEE Spectrum* **34**, 52–59. ISSN: 1939-9340 (June 1997).
- 167. Schlickeiser, R. & Kröger, M. Analytical Modeling of the Temporal Evolution of Epidemics Outbreaks Accounting for Vaccinations. *Physics* **3**, 386–426. ISSN: 2624-8174 (2 June 2021).
- 168. Schlosser, F. *et al.* COVID-19 Lockdown Induces Disease-Mitigating Structural Changes in Mobility Networks. *Proc. Natl. Acad. Sci. U.S.A.* **117**, 32883–32890. ISSN: 0027-8424 (2020).
- 169. Sharkey, K. J., Kiss, I. Z., Wilkinson, R. R. & Simon, P. L. Exact Equations for SIR Epidemics on Tree Graphs. *Bulletin of Mathematical Biology* **77**, 614–645. ISSN: 0092-8240, 1522-9602 (Apr. 2015).
- 170. Sharkey, K. J. Deterministic Epidemiological Models at the Individual Level. *Journal of Mathematical Biology* **57**, 311–331. ISSN: 0303-6812, 1432-1416 (Sept. 2008).

BIBLIOGRAPHY

- 171. Sharkey, K. J. Deterministic Epidemic Models on Contact Networks: Correlations and Unbiological Terms. *Theoretical Population Biology* **79**, 115–129. ISSN: 00405809 (June 2011).
- 172. Sharkey, K. J. & Wilkinson, R. R. Complete Hierarchies of SIR Models on Arbitrary Networks with Exact and Approximate Moment Closure. *Math. Biosci.* **264**, 74–85. ISSN: 00255564 (June 2015).
- 173. Shrestha, M., Scarpino, S. V. & Moore, C. Message-Passing Approach for Recurrent-State Epidemic Models on Networks. *Phys. Rev. E* **92**, 022821. ISSN: 1539-3755, 1550-2376 (Aug. 2015).
- 174. Simini, F., González, M. C., Maritan, A. & Barabási, A. -. A Universal Model for Mobility and Migration Patterns. *Nature* **484**, 96–100 (2012).
- 175. Simini, F., Barlacchi, G., Luca, M. & Pappalardo, L. A Deep Gravity Model for Mobility Flows Generation. *Nature Communications* **12**, 6576. ISSN: 2041-1723 (Dec. 2021).
- 176. Song, C., Koren, T., Wang, P. & Barabási, A. -. Modelling the Scaling Properties of Human Mobility. *Nat. Phys.* **6**, 818–823 (2010).
- 177. Song, C., Qu, Z., Blumm, N. & Barabási, A. -. Limits of Predictability in Human Mobility. *Science* **327**, 1018–1021 (2010).
- 178. *Statement from the National Public Health Emergency Team - Tuesday 29 December* <https://www.gov.uk/en/press-release/86f64-statement-from-the-national-public-health-emergency-team-tuesday-29-december/> (2022).
- 179. Tang, Y., Huang, D., Ruan, S. & Zhang, W. Coexistence of Limit Cycles and Homoclinic Loops in a SIRS Model with a Nonlinear Incidence Rate. *SIAM Journal on Applied Mathematics* **69**, 621–639. ISSN: 0036-1399, 1095-712X (Jan. 2008).
- 180. *Temporal Network Theory* <https://link.springer.com/book/10.1007/978-3-030-23495-9> (2022) ().

181. Tenenbaum, M. & Pollard, H. *Ordinary Differential Equations: An Elementary Textbook for Students of Mathematics, Engineering, and the Sciences* 808 pp. ISBN: 978-0-486-64940-5 (Dover Publications, New York, 1985).
182. Thanh Le, T. *et al.* The COVID-19 Vaccine Development Landscape. *Nature Reviews Drug Discovery* **19**, 305–306. ISSN: 1474-1776, 1474-1784 (May 2020).
183. *The 2001 Outbreak of Foot and Mouth Disease - National Audit Office (NAO) Press Release* National Audit Office. <https://www.nao.org.uk/press-release/the-2001-outbreak-of-foot-and-mouth-disease-2/> (2022).
184. *The Fundamental Advantages of Temporal Networks* https://www.science.org/doi/full/10.1126/science.aai7488?casa_token=J3k9dRRlvJ4AAAAA:vACKiRmrsWMD9GOD1ZZLbq4pZGbQ03JMp9EoHg-NFYIgXvvemZbaxl8MznltLgb9bY00NrU7i (2022).
185. Thulke, H. -. *et al.* Eradicating BVD, Reviewing Irish Programme Data and Model Predictions to Support Prospective Decision Making. *Preventive Veterinary Medicine* **150**, 151–161. ISSN: 0167-5877 (Feb. 1, 2018).
186. Tratalos, J. A., Graham, D. A. & More, S. J. Patterns of Calving and Young Stock Movement in Ireland and Their Implications for BVD Sero-surveillance. *Preventive Veterinary Medicine* **142**, 30–38. ISSN: 01675877 (July 2017).
187. Tratalos, J. A. *et al.* Spatial and Network Characteristics of Irish Cattle Movements. *Preventive Veterinary Medicine* **183**, 105095. ISSN: 01675877 (Oct. 2020).
188. Truscott, J. & Ferguson, N. M. Evaluating the Adequacy of Gravity Models as a Description of Human Mobility for Epidemic Modelling. *PLOS Computational Biology* **8**, e1002699. ISSN: 1553-7358 (Oct. 18, 2012).
189. Valdano, E., Ferreri, L., Poletto, C. & Colizza, V. Analytical Computation of the Epidemic Threshold on Temporal Networks. *Physical Review X* **5**, 021005. ISSN: 2160-3308 (Apr. 2015).

BIBLIOGRAPHY

- 190. Van den Driessche, P. & Watmough, J. Reproduction Numbers and Sub-Threshold Endemic Equilibria for Compartmental Models of Disease Transmission. *Mathematical Biosciences* **180**, 29–48. ISSN: 0025-5564 (2002).
- 191. Van Bergeijk, P. A. G. & Brakman, S. *The Gravity Model in International Trade: Advances and Applications* 373 pp. ISBN: 978-1-139-48828-0. Google Books: vQSWRPuMoZMC (Cambridge University Press, June 10, 2010).
- 192. Wang, D., Pedreschi, D., Song, C., Giannotti, F. & Barabasi, A.-L. *Human Mobility, Social Ties, and Link Prediction in Proceedings of the 17th ACM SIGKDD International Conference on Knowledge Discovery and Data Mining - KDD '11* The 17th ACM SIGKDD International Conference (ACM Press, San Diego, California, USA, 2011), 1100. ISBN: 978-1-4503-0813-7.
- 193. Wang, J., Wang, X. & Wu, J. *Inferring Metapopulation Propagation Network for Intra-city Epidemic Control and Prevention in Proceedings of the 24th ACM SIGKDD International Conference on Knowledge Discovery & Data Mining KDD '18*: The 24th ACM SIGKDD International Conference on Knowledge Discovery and Data Mining (ACM, London United Kingdom, July 19, 2018), 830–838. ISBN: 978-1-4503-5552-0.
- 194. Wang, Y., Chakrabarti, D., Wang, C. & Faloutsos, C. *Epidemic Spreading in Real Networks: An Eigenvalue Viewpoint in 22nd International Symposium on Reliable Distributed Systems, 2003. Proceedings*. 22nd International Symposium on Reliable Distributed Systems, 2003. Proceedings. (Oct. 2003), 25–34.
- 195. Wasserman, S. & Faust, K. *Social Network Analysis: Methods and Applications* 1st ed. ISBN: 978-0-521-38707-1 978-0-521-38269-4 978-0-511-81547-8 (Cambridge University Press, Nov. 25, 1994).
- 196. Watts, D. J. & Strogatz, S. H. Collective Dynamics of ‘Small-World’ Networks. **393**, 3 (1998).
- 197. White, D. R. & Borgatti, S. P. Betweenness Centrality Measures for Directed Graphs. *Social Networks* **16**, 335–346. ISSN: 03788733 (Oct. 1994).

- 198. WHO Recommends Groundbreaking Malaria Vaccine for Children at Risk
<https://www.who.int/news/item/06-10-2021-who-recommends-groundbreaking-malaria-vaccine-for-children-at-risk> (2022).
- 199. Widgren, S. *et al.* Data-Driven Network Modelling of Disease Transmission Using Complete Population Movement Data: Spread of VTEC O157 in Swedish Cattle. *Veterinary Research* **47**, 81. ISSN: 1297-9716 (Aug. 11, 2016).
- 200. Wilson, A. G. The Use of Entropy Maximising Models, in the Theory of Trip Distribution, Mode Split and Route Split. *Journal of Transport Economics and Policy* **3**, 108–126. ISSN: 00225258. <http://www.jstor.org/stable/20052128> (2022) (1969).
- 201. World Health Organization. Global Measles and Rubella Strategic Plan: 2012, 42. ISSN: 9789241503396. <https://apps.who.int/iris/handle/10665/44855> (2022) (2012).
- 202. Yang, L. *et al.* COVID-19: Immunopathogenesis and Immunotherapeutics. *Signal Transduction and Targeted Therapy* **5**, 1–8. ISSN: 2059-3635 (1 July 25, 2020).
- 203. Zhan, X.-X., Li, Z., Masuda, N., Holme, P. & Wang, H. Susceptible-Infected-Spreading-Based Network Embedding in Static and Temporal Networks. *EPJ Data Science* **9**, 30 (2020).